





Università degli Studi di Napoli Federico II
Dottorato di Ricerca in
Ingegneria Strutturale, Geotecnica e Rischio Sismico

**Thesis for the Degree of Doctor of Philosophy**

# Design, development and implementation of methodologies for real-time analysis and modeling of seismic data for Earthquake Early Warning Systems

by
**Valeria Longobardi**

Advisor: Prof. Aldo Zollo
Co-advisor: Dr. Simona Colombelli

Scuola Politecnica e delle Scienze di Base
Dipartimento di Strutture per l'Ingegneria e l'Architettura


La borsa di dottorato è stata cofinanziata con risorse del
Programma Operativo Nazionale Ricerca e Innovazione 2014-2020, risorse FSE REACT-EU
Azione IV.4 “Dottorati e contratti di ricerca su tematiche dell’innovazione”
e Azione IV.5 “Dottorati su tematiche Green”

*"I boschi su le cime*
*de le montagne crollansi, e le mura*
*de le cittadi popolose, e i templi*
*ondeggiano perfino, allor che scuoti*
*tu col tridente flebile la terra,*
*e gran fracasso s'ode e molto pianto*
*per ogni strada."*

*Inno a Nettuno (vv. 142-148)*

# Design, development and implementation of methodologies for real-time analysis and modeling of seismic data for Earthquake Early Warning Systems

Ph.D. Thesis presented
for the fulfillment of the Degree of Doctor of Philosophy
in Ingegneria Strutturale, Geotecnica e Rischio Sismico
by

Valeria Longobardi

February 2025

Approved as to style and content by

Prof. Aldo Zollo, Advisor

Dr. Simona Colombelli, Co-advisor

Università degli Studi di Napoli Federico II
Ph.D. Program in Ingegneria Strutturale, Geotecnica e Rischio Sismico
XXXVII cycle - Coordinator: Prof. Iunio Iervolino

www.dist.unina.it/dottorati-di-ricerca/dottorati

# Abstract

This PhD thesis is developed within the framework of *Earthquake Early Warning* (EEW), a research topic that investigates the feasibility of issuing rapid alerts to mitigate the impact of earthquake striking target sites. The work addresses various aspects of EEW, focusing on the analysis of early P-wave signals and the development of *on-site* algorithms for earthquake intensity estimation. The main motivation is to improve the timeliness and accuracy of alerts using data from individual stations and short time windows.

The original contribution of this research is the development of an *on-site* EEW software package, tested on datasets from various tectonic environments, including the Campi Flegrei area.

Moreover, the analysis of early P-wave displacement growth led to the discovery of a global scaling relationship between the P-wave growth rate and the final earthquake magnitude, offering new opportunities for rapid magnitude estimation. These findings also have implications for earthquake nucleation studies, suggesting that the early portion of the P-wave signals could provide crucial information on the nucleation stage and non-radiative processes preceding dynamic rupture propagation.

**Keywords:** Earthquake Early Warning, earthquake source observations, magnitude estimation, earthquake rupture physics.

# Sintesi in lingua italiana

Questa tesi di dottorato si inserisce nel campo del *Earthquake Early Warning* (EEW), una disciplina scientifica che studia la fattibilità di emettere avvisi rapidi per mitigare l'impatto dei terremoti a siti di interesse. Il lavoro affronta vari aspetti dell'EEW, con particolare attenzione all'analisi dei primi secondi di segnale delle onde P e allo sviluppo di algoritmi *on-site* per la stima dei parametri di sorgente e dell'intensità del terremoto. La motivazione principale è quella di migliorare la tempestività e l'accuratezza degli allarmi, utilizzando dati provenienti da stazioni individuali e finestre temporali brevi.

Il contributo originale di questa ricerca consiste nello sviluppo di un pacchetto software per l'EEW *on-site*, testato su dataset provenienti da vari ambienti tettonici, tra cui i Campi Flegrei.

Inoltre, l'analisi della crescita iniziale dell'ampiezza delle onde P ha portato alla scoperta di una relazione di scaling globale tra la velocità di crescita dell'ampiezza delle onde P e la magnitudo finale del terremoto, aprendo nuove prospettive per la stima rapida della magnitudo. Questi risultati hanno anche implicazioni per lo studio della nucleazione del terremoto, suggerendo che la fase iniziale delle onde P potrebbe fornire informazioni cruciali sullo stadio di nucleazione e sui processi non-radiativi che precedono la propagazione dinamica della rottura.

**Parole chiave:** Earthquake Early Warning, osservazioni sulla sorgente sismica, stima della magnitudo, fisica della rottura del terremoto.

# CONTENTS

# List of figures

# List of tables

# Introduction

This thesis work developed in the framework of Earthquake Early Warning (EEW), e.g. the field of Earthquake Science that explore the scientific and technological feasibility of issuing a rapid alert from the analysis of early earthquake signals to mitigate the impact of late arriving, strong shaking waves. EEW systems are designed to this scope.

This study addresses various aspects of earthquake early warning (EEW), with a particular focus on methods for analyzing seismic waveforms—especially early P-wave signals. The main applications center on on-site EEW algorithms, which use data from individual stations and brief time windows to predict expected shaking intensity and source parameters. The work also explores the physics of earthquake rupture, examining its connection to the eventual earthquake size and the potential use of rapid magnitude-estimation modules in EEW systems.

The main outcome of this research is an on-site EEW software package for both real-time and retrospective analysis, developed in collaboration with TME Srl, an industrial partner in the frame of an industrial doctorate (Dottorato Industriale). The industrial doctorate is a specialized doctoral program designed to bridge the gap between academia and industry, and it is conducted collaboratively by the university and an external company, in our case the company TME srl. Under this scheme the doctoral research project directly aligned with the company's R&D goals, while also fulfilling the academic requirements set by the university.

Given the wide array of topics encompassed by Earthquake Early Warning (EEW), this thesis is organized into three main parts, each addressing a distinct aspect of the field.

---

**Part 1** describes the fundamental principles of EEW and its practical implementations.

- **Chapter 1** offers a detailed explanation of the parameters used in contemporary EEW methodologies, with special attention to early seismic signal observations and their relation to earthquake nucleation.

- **Chapter 2** provides a comprehensive overview of the current global status of EEW systems, followed by a discussion of the two system approaches: source-based and impact-based. These configurations are examined in terms of their design features, operational goals, and the contexts in which they are typically employed.

---

**Part 2** focuses on the application of on-site EEW algorithms to real-world earthquake scenarios.

- **Chapter 3** describes the implementation of the on-site Alert Level system (SAVE) across several seismically active regions worldwide. This chapter presents test results from notable events such as the 2023 Turkey-Syria earthquake doublet, the Md 4.2 Campi Flegrei earthquake, and a large earthquake dataset in California.
- **Chapter 4** highlights the next generation of P-wave-based on-site warning systems, with particular emphasis on the P-Alert system. The chapter examines the system's performance through analyses of a Californian earthquake database, shedding light on its robustness, accuracy, and potential for wider deployment.

---

**Part 3** explores emerging perspectives for EEW by investigating the first few seconds of P-wave arrivals.

- **Chapter 5** showcases insights derived from an innovative global seismic catalog, focusing on early P-wave displacement growth rates—those observed in less than one second. The discussion addresses the significance of these short-timescale

observations for both earthquake rupture physics and rapid magnitude estimation. It also evaluates how these findings can advance future EEW applications by improving alert accuracy and lead time.

By progressing from foundational EEW concepts to innovative research on early P-wave processing and modelling, this thesis aims to bridge theoretical groundwork with practical applications, ultimately contributing to more effective and timely earthquake early warning systems.

# PART 1 – PRINCIPLES OF EARTHQUAKE EARLY WARNING

# CHAPTER

# 1 Physical grounds of Earthquake Early Warning

Earthquake Early Warning (EEW) is about the fast delivery of alerts announcing the impending ground shaking due to an earthquake which has already nucleated. Since an EEW is issued only when the earthquake rupture has already started, the warning time is defined as the difference between the first earthquake detection/characterization and the occurrence of strong ground shaking at the user's site. Therefore, the time scale of EEW spans from few seconds to several tens of seconds after the earthquake beginning. The concept of EEW dates back to 1868 following an earthquake on the Hayward Fault in California, when J.D Cooper (Cooper, 1868) proposed a system that could transmit a warning to the city of San Francisco through telegraph cables which were far away from the city: anytime an earthquake would have struck, the warnings sent via cables could have been used to ring an alarm bell in the city.

Although the concept is quite immediate, the implementation is more difficult. Given the limited amount of time for an EEW system to be effective, the earthquake has to be characterized in terms of location and magnitude in a rapid and reliable way using few seconds of the available early seismic signal. This also poses challenging questions on earthquake physics, concerning the possibility of estimating the final earthquake magnitude from the first few seconds of recorded signals. The worldwide development of different types of instruments (including near fault accelerometers, borehole and strain rate sensors, fiber optic cables) recording high resolution signals have paved the way to refined analysis issuing questions about the physics of the earthquake rupture. Providing answers to the complex debate about the earthquake determinism will provide new perspective not only for future EEW applications but also for understanding the physical nature of the earthquake nucleation.

## 1.1 A basic grasp of seismology: the Representation Theorem

In order to discuss the basic concepts of EEW it is useful to start from the seismic signal and the physics behind its representation. Let us recall that the equations governing the propagation of seismic waves within the Earth, far from the source zone, are linear differential equations with constant coefficients. This is a consequence of the reasonable assumption of elastic behavior in these regions. However, it should be noted that the energy accumulated near the source, because of tectonic processes, is only partially used for seismic radiation. A significant portion of this energy is spent in fracturing processes at the source, which cannot be considered elastic. Nevertheless, when considering everything that occurs outside the source zone, it is reasonable to treat the Earth as a linear and stationary filter, with stationarity clearly limited to the duration of seismic wave propagation.

In other words, considering also the effect of the measuring apparatus, the seismogram recorded at the Earth's surface can be viewed as the output of a chain of filters (assumed to be linear and time-invariant) that modify the shape and amplitude of the signal (input) emitted by the seismic source. The relationship between the input and output of a chain of filters, if all the filters are linear and time-invariant, is expressed through the operation of convolution. Describing the chain of filters—comprising the Earth and the measuring instrument—by two functions of time, P(t) and I(t), and denoting the source function by S(t), the seismogram u(t) is given by:

$$u(t) = S(t) * P(t) * I(t) \qquad (1)$$

in the time domain $t$, or, by using the convolution theorem as:

$$u(\omega) = S(\omega)P(\omega)I(\omega) \qquad (2)$$

In the frequency domain $\omega$. Equations (1) and (2) generally represent the relationship between the seismogram and the various effects that contribute to its composition. In principle, if the function $P$ is known in the time or the frequency domain, and if the instrumental response $I$ is known, it is possible to use equations XX and XX to directly determine the function $S$ from the seismograms, which represents the time variation of the seismic source. Seismic sources are spatially extended, and seismograms are recorded at various points on the Earth's surface. Consequently, formula (1) needs to be modified to include spatial coordinates, as it follows:

$$u(\boldsymbol{x}, t) = \mathrm{S}(\boldsymbol{\xi}, \mathrm{t}) * \mathrm{G}(\mathbf{x}, \boldsymbol{\xi}, \mathrm{t}) * \mathrm{I}(\mathbf{x}, \mathrm{t}) \quad (3)$$

Where the vector $\boldsymbol{x}$ represents the coordinate position of the receiver and the vector $\boldsymbol{\xi}$ represents the coordinate position of the portion of the source being considered. In equation (3), the term $G(\boldsymbol{x},\boldsymbol{\xi},t)$ , the elastodynamic Green function, generally accounts for wave propagation effects, including, for example, anelastic attenuation and site effects. The elastodynamic Green's function can be calculated by solving the wave equation once the distribution of elastic/anelastic properties of the propagation medium is known.

For earthquake early warning purposes, the portion of the signal related to the P-wave, $u_P(\boldsymbol{x_R},t)$, at a given site $\mathbf{x_R}$ is used to give an estimate of the impact of the more damaging (and slower propagating) S-waves since the two phases are related to the same seismic source (as it is shown in equation (3)). In the next paragraph, we described the parameters and the methods that links the early P-wave content to the late S-wave content expected at a certain location.

## 1.2 The scaling between the early P-wave and the S-wave

An earthquake excites both *P* and *S* waves. The *S* wave carries the major destructive energy, and the smaller- amplitude *P* wave precedes the *S* wave by the time typically equal to the 60% of the *S*-wave travel time to the station. The initial portion of the *P* wave, despite its small and nondestructive amplitude, carries the information of the earthquake size, and a good determination of the earthquake size from the *P* wave provides information about the strength of shaking being brought by the following *S* wave. Indeed, in the early development of EEW methods, many authors (e.g (Kanamori, 2005) (Wu and Kanamori, 2005c), (Olson and Allen, 2005), (Zollo et al., 2006)) put their efforts into exploring the feasibility of the fast characterization of the earthquake source from the analysis of the parameters associated to few seconds of the P-wave signals. These parameters depend either on the P-wave amplitude or on the P-wave frequency content. Their combination is nowadays largely used in EEW systems (see chapter 2).

### 1.2.1 The early P-wave amplitude: Pa, Pv, Pd

Empirically derived relations and theoretical arguments show that the peak ground-motion amplitudes (Peak Ground Acceleration *PGA*, Peak Ground Velocity *PGV* and Peak Ground Displacement *PGD*) correlate with the amplitude of the initial motions such

as P-peak acceleration *Pa*, P-peak velocity *Pv*, and P-peak of displacement *Pd* ((Kanamori, 2005), (Wu and Kanamori, 2008)). To get the aforementioned parameters, the acceleration signals are integrated to velocity and displacement. Eventually, a high-pass filter with cut-off frequency of 0.075 Hz is applied on the displacement to remove the low-frequency drift (baseline) that might affect the signal after the last integration. Generally, for a nearby small event, Pa can be large but the *PGA* and *PGV* are small. Pa is usually determined by a very-high-frequency wave with short duration which does not have a high-damage potential. In contrast, Pv and Pd contain more long-period energy than Pa and correlate well with *PGA* and *PGV*. Pd correlates well with the Peak Ground Motion parameters (Wu and Kanamori, 2005c). As an amplitude parameter, the peak amplitude of the initial P-wave displacement, Pd, reflects the attenuation relationship of the ground motion with distance. This hypothesis paved the way to the calibration of empirical scaling laws that linked the early P-wave amplitude to a rapid magnitude characterization. As example, Wu and Zao (2006) investigated the attenuation of Pd with hypocentral distance R in Southern California, resulting in the following type of scaling law:

$$\log(\mathrm{Pd}) = \mathrm{A} + \mathrm{B} \cdot \mathrm{M} + \mathrm{C} \cdot \log\mathrm{R} \qquad (4)$$

Where M is the event magnitude. Similar results were also found for other regions of the world, such as Italy and Taiwan ((Zollo et al., 2006), (Wu, 2003)). The equation (4) was used to define a measure of magnitude, called "Pd magnitude". In many studies ((Kanamori, 2005), (Wu and Kanamori, 2008), (Allen and Kanamori, 2003)), the maximum time window explored to evaluate the earthquake magnitude, and the expected Peak Ground Motion was set to three seconds since the detection of the P-wave on the seismogram, to keep short the warning time.

An obvious trade-off exists between the duration of the initial motion and the reliability of magnitude/ground-shaking prediction. Below Mw 5.5-6.0, a couple of seconds of P-wave data would contain nearly the entire history of fault rupture and a scaling relation. Above Mw 5.5-6.0 a saturation effect was observed when equation (4) was used to evaluate the "Pd magnitude" (Wu and Zhao, 2006). Zollo et al (2006) proposed a combination of both the early P- and S-wave to get a more robust magnitude estimation. Particularly, they retrieved the magnitude dependence of early P-

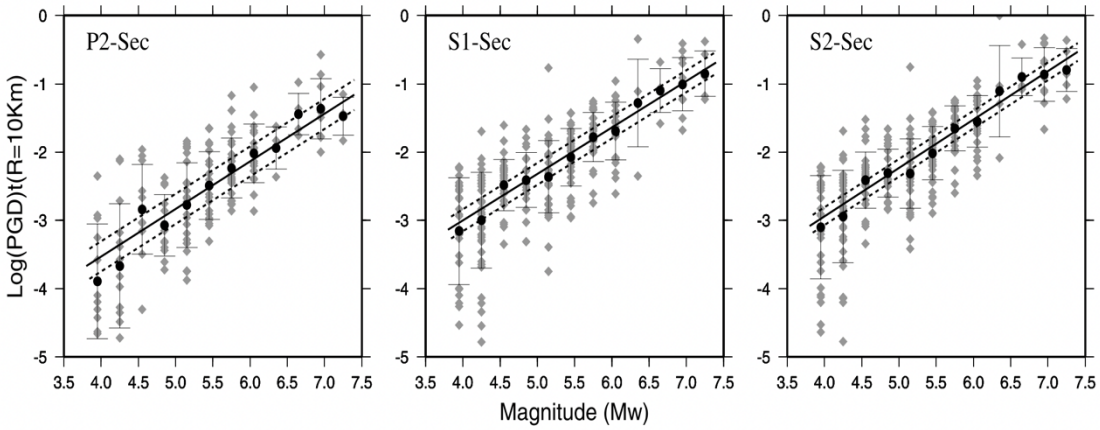


*Figure 1.2.1: Correlation between low-pass filtered peak ground motion value and moment-magnitude. The panels show the logarithm of peak ground displacement normalized at a reference distance of 10 km as a function of Mw in time windows of (left) 2 sec length from the first P-arrival and (middle) 1- and (right) 2- sec from the first S-arrivals (from (Zollo et al., 2006)).*

and S- peak amplitudes by correcting the equation (4) for the distance effect, normalizing to a reference distance of R=10 km. Due to the uncertainty in the identification of the first P arrival time, only the 2-sec window were considered while both 1-sec and 2-sec windows were used for S-waves (see Figure 1.2.1). Lancieri and Zollo (Lancieri and Zollo, 2008) further developed and refined these concepts.

Considering the discussions of Zollo et al. (2006), one of the hypotheses that causatively links the early peak amplitude parameters to the final earthquake size might be explained as it follows. The peak ground displacement depends on the relatively high frequency content of the signal. Since the receivers are usually not in the immediate proximity of the rupturing fault and that the rupture directivity is averaged by the azimuthal locations of the recording stations, the seismic radiation can be assimilated to the far-field content of a point source. In this first approximation, the radiated P-wave predicts a ground motion u(t) at a distance r can be written as (Aki and Richards, 2009):

$$u(t) = \frac{A^{FP}}{4\pi\rho r\alpha^3}\dot{M}_0(t - \frac{r}{\alpha}) \qquad (5)$$

Where $\alpha$ is the P-wave velocity, $\rho$ is the medium density, $A^{FP}$ describes radiation angular dependence. $\dot{M}_0$ is the moment rate that scales with the average slip-rate. The slip-rate is controlled by the stress drop $\Delta\sigma$ and the length of the slipping fault area (Kostrov, 1964). As a consequence, in a probabilistic sense, earthquake that fractures with higher dynamic stress drop and/or active surface at their initiation, have an increased probability of propagating to larger distances and radiate larger wave amplitudes, as seen from the peak

ground motion in the early portion of near-source P and S-signals in various studies ((Wu and Zhao, 2006), (Wu and Zhao, 2006), (Wu and Kanamori, 2005c))

### 1.2.2 The early P-wave characteristic period: $\tau_c$ and $\tau_p^{max}$

To determine the size of an earthquake, it is important to determine whether the event's slip motion has stopped or is still growing, which is generally reflected in the period of the initial motion. Small and large events yield short- and long-period initial motions, respectively. However, the slip motion is in general complex, and even a large event often begins with a small, short-period motion, followed by a long-period motion. Consequently, it is important to define the average period during the first motion. Kanamori (2005) modified the method that was first proposed by Nakamura (1988) to measure the parameter $\tau_c$, representing the average period of the initial portion of the P-wave ((Kanamori, 2005)(Nakamura, 1988)). The mathematical details of the $\tau_c$ evaluation are presented in Box 1.2.1. The difference in the method proposed by Kanamori (2005) with respect to the method of Nakamura (1988) relies on the fact that for the $\tau_c$ evaluation a short window of P-wave signal is being used (usually up to 3 seconds after the first P-wave detection).

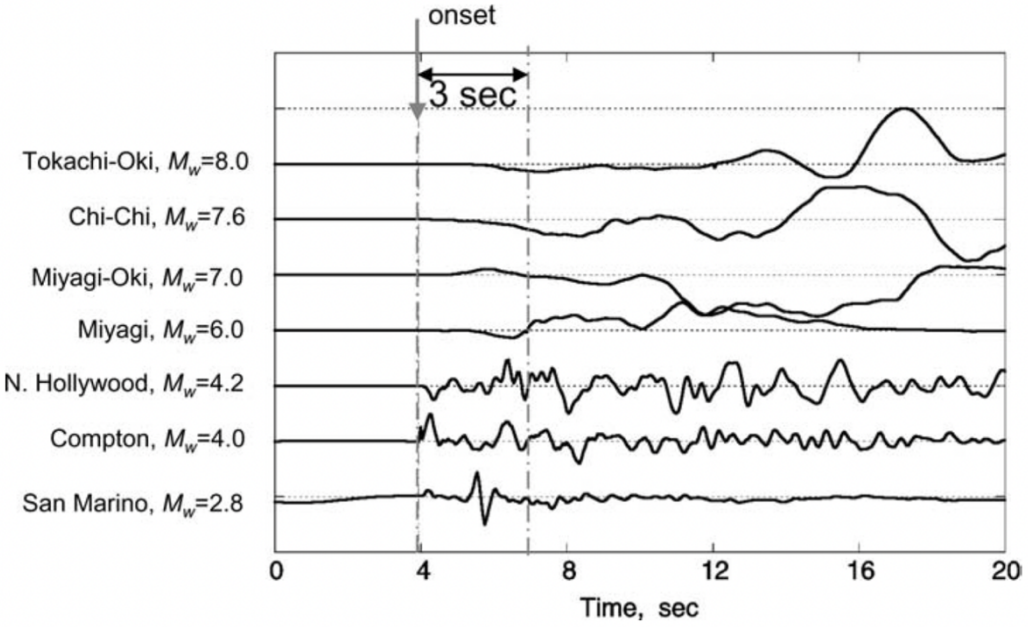


*Figure 1.2.2: The waveforms of the beginning of close-in displacement records of earthquakes with magnitudes from 2.8 to 8. The amplitudes are in arbitrary scale. The first 3 s is indicated by two dash-dot lines (from (Kanamori, 2005)).*

The method was successfully applied to real earthquakes data (some waveforms examples from Kanamori (2005) are presented in Figure 1.2.2), proving that the $\tau_c$ parameter scales

***Box 1.2.1: $\tau_c$ and $\tau_{max}^P$ measurement***

***Average P-wave period $\tau_c$***

We consider the ground-motion displacement *u(t)* and velocity $\dot{u}(t)$ from the vertical component record and evaluate the ratio *r*:

$$r = \frac{\int_0^{\tau_0} \dot{u}^2(t)dt}{\int_0^{\tau_0} u^2(t)dt} \qquad \text{(I)}$$

Usually, $\tau_0$ is set at 3 seconds after the onset of P-wave. Using Parseval's theorem,

$$r = \frac{4\pi^2 \int_0^{\infty} f^2 |\hat{u}(f)|^2 df}{\int_0^{\infty} |\hat{u}(f)|^2 df} = 4\pi^2 \langle f^2 \rangle \qquad \text{(II)}$$

Where $\hat{u}(f)$ is the frequency spectrum of *u(t)* and $\langle f^2 \rangle$ is the weighted average of $f^2$. Hence,

$$\tau_c = \frac{1}{\sqrt{\langle f^2 \rangle}} = \frac{1}{\sqrt{r}} \qquad \text{(III)}$$

***Predominant P-wave period $\tau_{max}^P$***

Let us consider $X_i$ the smoothed ground velocity squared at time *i* obtained as:

$$X_i = \alpha X_{i-1} + x_i^2 \qquad \text{(IV)}$$

where $x_i$ is the recorded ground velocity at time *i* and alpha is a smoothing constant, and $D_i$ the smoothed velocity derivative squared obtained as:

$$D_i = \alpha D_{i-1} + \left(dx/dt\right)_i^2 \qquad \text{(V)}$$

Thus, the predominant period is determined in real-time as:

$$\tau_i^P = 2\pi\sqrt{X_i/D_i} \qquad \text{(VI)}$$

with the event magnitude and keeps increasing even for earthquakes with magnitude M>7 having no saturation effects (Wu and Kanamori, 2005a).

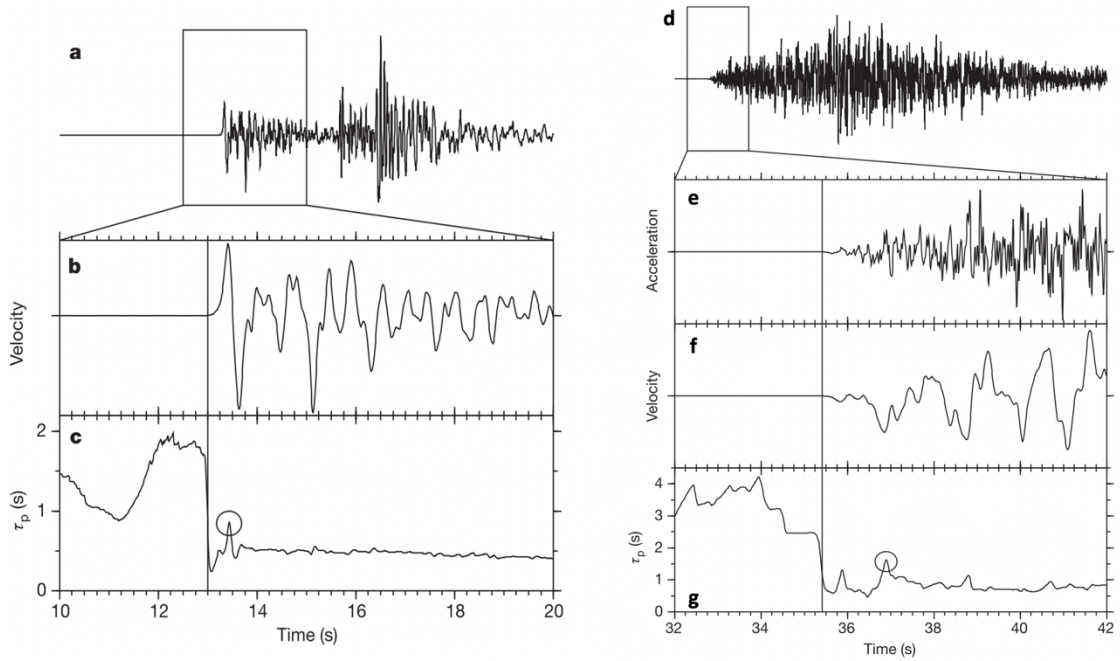


*Figure 1.2.3: Example of waveforms and $\tau_p^{max}$ evaluations. **Left side**: waveform of a M 4.6 earthquake in southern California recorded at station GSC, 74 km from the epicentre. Panel **(a)** shows the raw vertical component waveform recorded by a broadband velocity sensor. Panel **(b)** shows ten seconds of the velocity waveform after low-pass filtering at 3 Hz. The P-wave trigger time is shown by the vertical line. Panel **(c)** shows $\tau_p(t)$ trace calculated in a recursive fashion from the waveform in panel b. **Right side**: waveform of the M w 8.3 Tokachi-oki earthquake, recorded at station HKD112, 71 km from the epicentre. Panel **(d)** shows the raw vertical component waveform recorded on an accelerometer. Panel **(e)** shows ten seconds of the raw acceleration waveform. The P-wave trigger is shown by the vertical line. Panel **(f)** shows ten seconds of the velocity waveform determined from the acceleration recording using recursive relations only. It has also been low-pass filtered at 3 Hz. Panel **(g)** $\tau_p(t)$ trace calculated in a recursive fashion from the waveform in panel f (from (Olson and Allen, 2005)).*

For the EEWS application, if $\tau_c$ < 1 sec, the event has already ended or is not likely to grow beyond M > 6. If $\tau_c$ > 1 sec, it is likely to grow, but how large it will eventually become cannot be determined by the $\tau_c$ paramter. In this sense, this method provides a threshold warning.

The average or characteristic period $\tau_c$ as described above is evaluated in a fixed P-wave time window. Allen and Kanamori (2003) suggested a method which measures the predominant period $\tau_p$ (Allen and Kanamori, 2003). The predominant period is determined continually in real time from the vertical component of the recording sensor and is defined through a recursive relation. The mathematical detail of $\tau_p$ evaluation is provided in Box 1.2.1.

Allen and Kanamori (2003) and Olson and Allen (2005) retrieved log-scaling relationships of the predominant period with the earthquake magnitude for different world data such as Japan, Taiwan and Southern California. Particularly, Allen and Kanamori (2003) found two scaling relations of the logarithm of $\tau_p^{max}$ with respect to two different magnitude range (M<5 and M>5). In fact, the higher frequency content of smaller magnitude earthquakes is measurable within a shorter time period after the P- wave arrival (see left side of Figure 1.2.3) than the low-frequency energy of larger events (see right side of Figure 1.2.3). Correspondingly, the magnitude of smaller events can be determined more rapidly than that of larger events. This also means that the $\tau_p^{max}$ method is underlying a threshold method, because the minimum time window of available signal (as example 1 second) is to be considered as a minimum magnitude estimate.

The evidence for a scaling relation between the early P-wave amplitude and frequency with the final magnitude for EEW purposes has paved the way for the scientifical debate on whether the first few seconds of P-wave are informative on the physics of the rupture process. Much of the discussion has focused on the time-domain characteristics of the P-wave. ((Colombelli et al., 2014),(Meier et al., 2016),(Melgar and Hayes, 2019), (Trugman et al., 2019))

## 1.3 The short-term P-wave as an insight into the earthquake nucleation

### 1.3.1 Overview of different seismological observations

In the previous paragraph, a summary of the physics and the methods of the early P-wave parameters has been presented. These parameters are largely adopted for EEW systems to characterize the earthquake source as fast as possible. However, whichever parameter is adopted ($P_x$, $\tau_c$, $\tau_{max}^P$), the scaling with magnitude is generally evident and robust up to magnitude 6.0–6.5, while a poor correlation is observed for larger magnitudes. The saturation is a well-known problem and has been extensively discussed in the literature ((Kanamori, 2005), (Zollo et al., 2006), (Lancieri and Zollo (2008)), (Rydelek et al., 2007)). To avoid the arising of the saturation effect, different authors started to analyze the behavior of the P-wave amplitude at longer time windows. Colombelli et al. (2012) observed that when the Pd is measured at each time step on the available records starting from the P-wave arrival, the saturation effect disappears for higher magnitude. The

***Box 1.3.1: The Logarithm of P-peak displacement versus time (LPDT) curve***

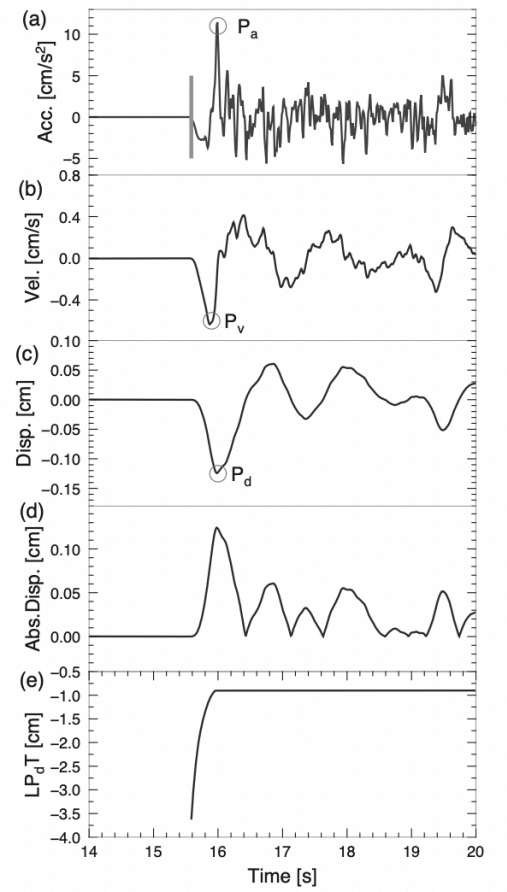


*Figure 1.3.1 The figure shows an example of waveform processing and LPDT curve computation for the 2011-07-25 M6.3 event recorded at the station MYG009 (distance 114 km). The figure shows: (a) acceleration [cm $s^{-2}$]; (b) velocity [cm $s^{-1}$]; (c) displacement [cm]; (d) absolute value of displacement [cm]; (e) LPDT curve [cm]. In all panels, time is referred to the time of the first sampling of records. Panels (a), (b) and (c) also show the peak amplitude values. The tick grey vertical line in panel a shows the manual P-wave arrival time identification. (from (Colombelli et al., 2020)).*

We here describe how to evaluate the Logarithm of P-peak displacement versus time (LPDT) curve upon the discussion provided by Colombelli et al. (2014). At each station, (1) the acceleration waveform is integrated twice to get the displacement (panel a, b, c of Figure 1.3.1); (2) the displacement is filtered with high-pass cutoff frequency of 0.075 Hz; (3) the absolute value of the displacement is evaluated (panel d of Figure 1.3.1).; (4) starting from the P-wave on set, the P-peak of displacement Pd is measured in an expanding time window with step equal to the signal time step; (5) finally, the logarithm of Pd is corrected by the distance through the approach described in paragraph 1.2.1 equation (4). The resulting LPD is plotted versus time vector (panel e of Figure 1.3.1)

approach follows the physics behind equation (4), where the logarithm of Pd is updated

at each time step on the seismograms (Colombelli et al., 2012). Colombelli et al. (2014) analyzed a set of Japanese earthquakes spanning a range of $M_{JMA}$ (magnitude

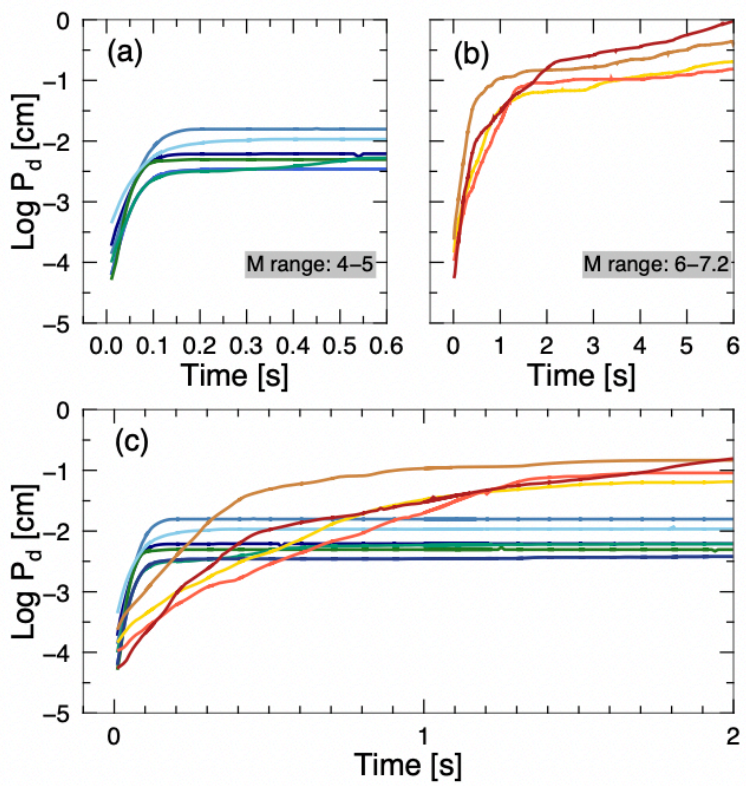


*Figure 1.3.2: Examples of LPdT curves for different magnitudes in a common distance range. The figure shows examples of average LPdT curves, for two different classes of magnitude, obtained using all the available data within a common distance range, between 20 and 50 km. Events in the magnitude range between 4 and 5 are shown with blue-shade colours, while larger events (in the magnitude range between 6 and 7.2) are shown with yellow- red shade colours. Panels (a) and (b) show the curves with their proper time scale, while in panel (c) the curves are plotted on the same time scale, to better illustrate the differences, in both shape and time scale, among the magnitude classes. In all panels, the amplitudes of LPdT curves are plotted as they are, without corrections for the distance effect. The effect of the initial slope decreasing with magnitude is rather evident, even in a common distance range.*

measurement by the Japanese Meteorological Agency) going from 4 to 9. For each event, the logarithm of Pd versus the P-wave Time Window is measured to obtain the Logarithm of the P-peak of displacement versus Time (LPDT) curve (see box 1.3.1). It is observed that each curve progressively increases with time until a final, stable value is reached. This stable value is called Plateau Level (PL hereinafter). PL shows a scaling with the magnitude (Colombelli and Zollo, 2015) and the time at which it is reached corresponds to the half duration of the apparent source time function by approximating it as an isosceles-triangular function (Zollo et al., 2022). Alongside this result, it is also observed that the initial slope of the LPDT curves shows a magnitude-dependency (Colombelli et al., 2014). Particularly, as it is shown in Figure 1.3.2, the steepest values of slope are typical of the smallest events (small magnitude values), while the gentlest values of the initial slope are typical of the biggest event (big magnitude values). This peculiar behavior

is already evident at very short time scales, in the order of few seconds of the P-wave signal (as it is shown in panel a and b of Figure 1.3.2). It is observed that at least one order of magnitude separates the class of class of small magnitudes (M~4) from the class of big magnitudes (M~7) (Colombelli et al., 2020).

For this reason, it was proposed that the initial slope of the LPDT curves could be a parameter for a fast magnitude characterization. We give a physical interpretation of the slope parameter and from where its behavior might arise in the next paragraph. In a more qualitative way, Colombelli et al. (2020) argued that the parameters controlling the shape of the LPDT curve (that are PL and the initial slope) could be related to the earthquake source model of Sato & Hirasawa (SATO and HIRASAWA, 1973) in the sense that they might be informative of the initial bending (the slope) of the modelled near-triangular source time functions towards the final peak (PL). This is a first step of interpretation that underlies a differentiation in the earthquake rupture beginning. Indeed, according to model c-d) and e-f of Figure 1.3.3, the LPDT curves, and their initial slope in particular, might indicate that it is possible to predict the final earthquake size from the first stage of the rupture initiation, suggesting a deterministic behavior of the earthquake beginning.

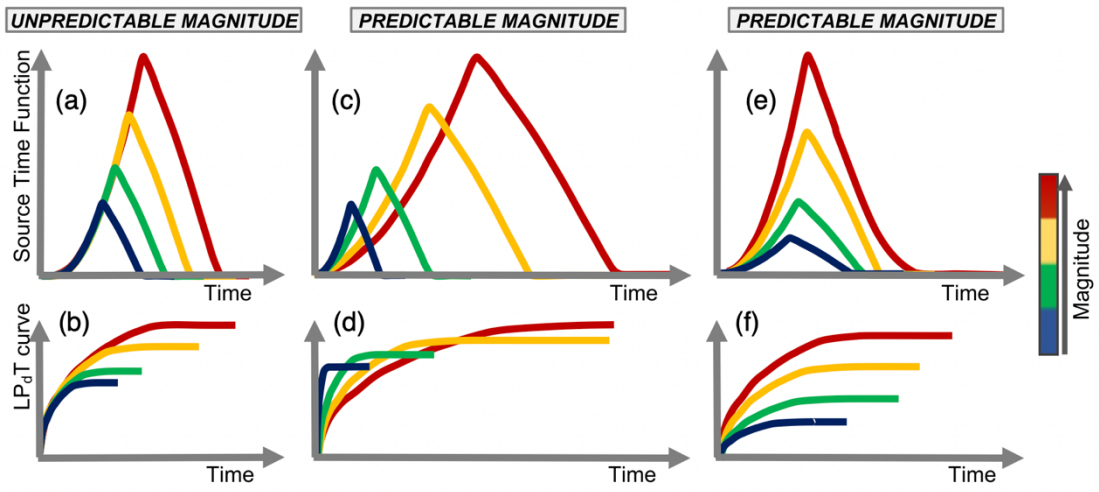


*Figure 1.3.3: Sketch of the relationship between STF and LPdT curves. The figure shows a conceptual scheme of the relationship between the STFs (as obtained from the Sato & Hirasawa 1973 model) and the corresponding LPdT curves, for two different models. Panels (a, b) show the case of ruptures with the same nucleation, for which the initial slope is the same for all magnitudes and the events become distinguishable at the peak of the STFs, which corresponds to the plateau level of LPdT curves. Panels (c, d) show the case of a completely predictable magnitude model, for which the STFs have a different beginning and the corresponding LPdT curves show a distinguishable slope, even at the initial part. In this case, the initial slope of STFs decreases with magnitude. Panels (e, f) show the third case of a predictable magnitude model, for which the initial slope of the STFs increases with magnitude (from (Colombelli et al., 2020))*

Other studies ((Melgar and Hayes, 2019), (Meier et al., 2016), (Meier et al., 2017), (Trugman et al., 2019)) performed similar analysis but obtained rather different results.

Melgar & Hayes (2019) considered the Source Time Functions (STFs) of moderate-to-large earthquake (Vallée and Douet, 2016) and HR-GNSS data in order to argue the deterministic behavior in the rupture process. They measured the "moment acceleration" that is the growth rate of the STFs over the first 20 seconds starting at the earthquake's origin time. In their study, in the very early stage of rupture (between origin time and the first 2 seconds of STFs), only a weak determinism between moment acceleration and final magnitude is observed. Interestingly, in the intermediate stage (2-20 seconds of STFs) a proportional scaling of moment acceleration with magnitude was found: the bigger the magnitude the bigger the value of PGD grows with time. This result could underly a model like the one represented in panel e of Figure 1.3.3, where the magnitude characterization is still possible before the STF has reaches its peak. Indeed, they suggested an interpretation where the initial phase of rupture is rather chaotic followed by a transition to a self-similar pulse.

Meier et al. (2016) examined the near-source peak displacement measurements, including the Japanese records and Southern Californian records with magnitude higher than 4. The pgd(t) static was obtained by separating the whole dataset into magnitude bins. The results showed that on average small and large earthquakes would follow the same amplitude growth and that the large events would start neither more nor less impulsively at their beginning (e.g the model of panel a of Figure 1.3.3). Meier et al. (2017) focused on the STFs of large earthquakes. The STFs were grouped by magnitude with a nearest-neighbor approach. For each point in time, the median was evaluated among the STFs falling within the same group. It is shown that the STFs grow linearly until the peak moment rate is reached and then start decaying with a similar rate. Moreover, the average growth rate does not vary significantly with magnitude. Trugman et al. (2019) also showed that the time evolution of Pd on a Japanese dataset of earthquakes with M4.5-9 suggests a universal pattern growth. To overcome the non-deterministic nature of rupture that these studies support for EEW purposes, it was suggested that the saturation affecting the $\log_{10}$Pd-M might provide the basis for a Bayesian approach. The earthquake magnitude can be estimate from a posterior probability obtained by the set of Pd measurements in the form of (Trugman et al., 2019):

$$P(M|log_{10}P_d, TW) \propto \mathrm{P}(log_{10}P_d, TW|M)\mathrm{P}(\mathrm{M}) \qquad (6)$$

Where $P(log_{10}P_d, TW|M)$ is the likelihood function of $log_{10}P_d$ in the considered Time Window TW for a given magnitude M; P(M) is the prior magnitude distribution and $P(M|log_{10}P_d, TW)$ is the posterior magnitude distribution.

### 1.3.2 The measure of the P-wave growth rate and its physical interpretations

The scaling of P-wave onset with the final earthquake size is so far contradictory. However, the differences that have arisen (we discussed them in paragraph 1.3.1) could be explained in terms of: (1) different type of data analyzed (strong motion, broadband, HR-GNSS); (2) different time scale of observation (from the first few seconds of P-wave onset to the tens of seconds of STFs). The question about whether the earthquake final size predictability could imply that the earthquake rupture has a deterministic behavior is still complicated to answer. The main reason for that comes from the fact that it is very challenging to map a process (the earthquake nucleation) that is linked to the aseismic, not-radiative phase of the physical phenomenon. A great opportunity to connect the observations from the early P-wave amplitude and its growth with the nucleation phase in which rupture loads comes from the laboratory experiments and the numerical modelling.

Many theoretical works have improved the understanding of rupture nucleation ((Dieterich, 1979), (Uenishi and Rice, 2003), (Rubin and Ampuero, 2005)). Indeed, it is known that the seismic rupture begins with a process of quasi-static slip accumulation over a limited region of the seismic fault. On this region, where the rupture starts loading, the slip slowly accumulates until reaching a critical threshold, beyond which the rupture becomes unstable and starts to propagate. Numerical modelling of the quasi-static phase is focused on developing constitutive laws for fault slip. A standard form of the constitutive law is (Rubin and Ampuero, 2005):

$$\frac{\tau}{\sigma} = f^* + \mathrm{a} \cdot \ln\frac{V}{V^*} + \mathrm{b} \cdot \ln\frac{V^*\theta}{D_c} \qquad (7)$$

where $\tau$ is the frictional strength, $\sigma$ is the normal stress, V is the sliding velocity, $\theta$ is the state variable (with units of time), $D_c$ is a characteristic sliding distance for the evolution of $\theta$, f* and V* are reference values of the friction and velocity, $a$ is a parameter that characterizes the increase in strength depending on the increase of velocity, $b$ is a parameter is a parameter that reflects the increase in strength depending on an increase of

the total area. Equation (7) makes clear that this process is governed by slip velocity as well as stress drop and characteristic lengths (such as $D_c$).

Through laboratory experiments researchers have been able to characterize the nucleation phase dynamics. Latour (2013) showed that the evolution of the rupture propagation is divided into three stages, each of them characterized by a different slope in the curve representing the logarithm of the rupture velocity versus the logarithm of the rupture length (Figure 1.3.4). These stages are named *quasi-static* stage, *acceleration* stage and *dynamic propagation* stage. In the first quasi-static stage the log-log scale between the rupture velocity and the rupture length has slope equal to 1, which indicates a linear dependence of the two parameters (Latour et al., 2013). During the quasi-static stage, the rupture grows exponentially as:

$$L = L_0 e^{\frac{t-t_0}{t_c}} \qquad t < t_0 \tag{8}$$

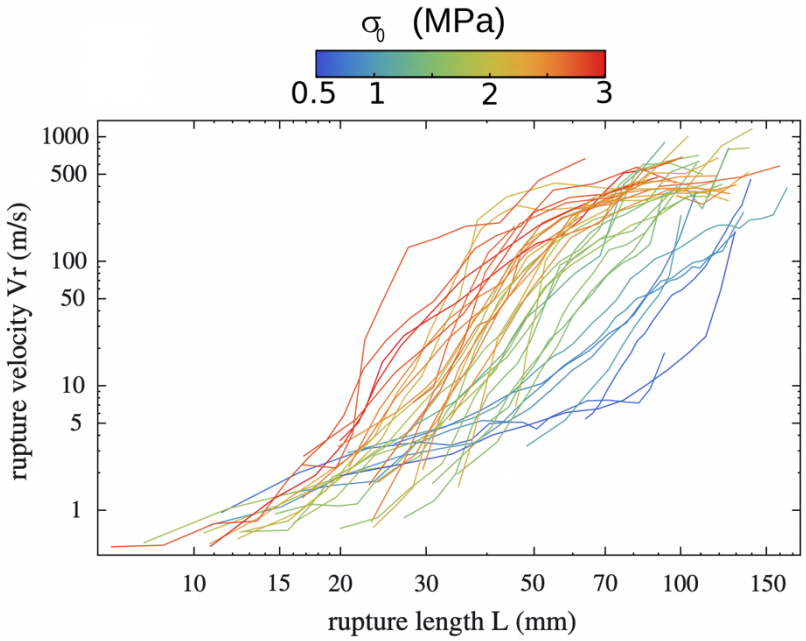


*Figure 1.3.4: Rupture velocity as a function of rupture length obtained from high-speed videos for 45 slip events (each curve represents a single rupture event). Changes in slope allow to distinguish different stages of dynamic rupture. The organization of the curves indicates a dependence with the initial normal stress (represented by color code) (from (Latour et al., 2013))*

where $L_0$ is the length of the rupture at the end of the quasi-static phase and $t_0$ is defined as the instant of the transition between the quasi-static and the acceleration phase; $t_c$ is a characteristic time defined by $t_c = L_0/Vr_0$ where $Vr_0$ is the velocity at time $t=t_0$. Time $t_0=0$ is arbitrarily defined as the last instant of exponential growth (quasi-static phase) and the beginning of the second phase (acceleration phase). The acceleration phase is characterized by slopes between rupture velocity and rupture length higher than 1. This

means in the acceleration stage the rupture velocity grows like a power of the rupture length. The solution to this kind of differential equation is:

$$L = \frac{L_0}{(1 - \frac{(n-1)(t-t_0)}{t_c})^{\frac{1}{n-1}}} \qquad t > 0 \tag{9}$$

In the equation (9), the rupture length L diverges at $t_0$+$t_f$ where $t_f = t_c/(n-1)$. Equations (8) and (9) indicate that the rupture is defined by the nucleation length $L_0$. In laboratory it is supported that $L_0$ is equal to the critical length Lc which is related to the frictional parameters (Campillo and Ionescu, 1997):

$$L_c = \beta \frac{\mu D_c}{\sigma_0 (f_s - f_d)} \tag{10}$$

where $f_s$ and $f_d$ are the static and dynamic friction coefficients, $D_c$ is the critical weakening distance, $\mu$ is the shear modulus, and β is a nondimensional coefficient. The characteristic time $t_c$ of the nucleation phase defines both the quasi-static phase (as shown in equation (8)) and the acceleration stage (as shown in equation (9)). The results obtained in laboratory experiments particularly show that the acceleration stage of the rupture is very well defined and relatively short, controlled by the critical length that ends the quasi-static phase when particular conditions are reached. Latour (2013) proposed that $t_c$ is represented as a ratio depending mostly on Dc and the difference between $f_s$, the static friction coefficient, and $f_d$, the dynamic friction coefficient as it follows:

$$t_c = \frac{k\mu}{p_0} \frac{D_c}{f_s - f_d} \tag{11}$$

To extrapolate Dc from equation (11) and to discussion its implications to the natural conditions, Colombelli et al. (2020) have given a first qualitative analysis that links the observed scaling of the initial growth rate of displacement with the earthquake final size with the laboratory observations. The growth rate is measured as the slope on the LPDT curve (see paragraph 1.3.1). So, it can be written as:

$$\partial LPDT/\partial t \propto \delta \dot{v}/\delta v \tag{12}$$

Equation (12) expresses the ratio between the slip acceleration and the slip velocity. Therefore, the initial growth rate of displacement measured as the slope of the LPDT has the physical dimension of the inverse of time. Having in mind the theoretical and

modelled concepts of the earthquake nucleation, the initial growth rate of the displacement expressed as the slope of the LPDT curves could relate to a characteristic time during the initial stage of the earthquake rupture. Indeed, using equation (11), with $t_c = 1/SLP_d$, Colombelli et al. (2020) found reasonable values $D_c$ varying from 0.1m to 1 m for events spanning a magnitude range from 4 to 9. In this interpretation, the initial growth rate of the early P-wave displacement might reflect the footprint of the acceleration stage of the earthquake nucleation preceding the full dynamic propagation, as observed for laboratory experiments.

New interpretations suggest that variations in the physical fracture parameters (such as stress drop/slip velocity and/or rupture velocity) during the initial phase of the radiative process may be the mechanisms that distinguish small earthquakes from large ones. This topic will be addressed in greater detail later in the thesis (Chapter 5)

The observed slope decrease with magnitude can be related to the effect of variable dynamic stress drop and/or rupture velocity in the initial stage of the rupture of small and large earthquakes, possibly triggered by the acceleration phase during the quasi-static rupture nucleation. Indeed, based on the dynamic-consistent model for an expanding shear circular crack of Sato & Hirasawa (1973), the relation between the early P radiated displacement pulse $\Omega_P(t)$ , the dynamic stress drop ($\tau_e$) and the rupture velocity ($v_R$) during the rupture growth phase can be written as: (Boatwright, 1980):

$$\Omega_P(t) = \frac{2\pi \Delta v_o v_R^2}{(1-\zeta^2)^2} t^2 \approx \frac{2\pi v_R^3 \tau_e}{\mu\,(1-\zeta^2)^2} t^2 \qquad (13)$$

where $\Delta v_o$ is peak slip velocity, $\mu$ the rigidity at the source region and $\zeta = \frac{v_R}{v_P}\sin\theta$ is the P-wave *apparent* Mach number (Boatwright, 1980), with $\theta$ being the angle between the ray take-off direction and the normal to the circular fault. The term including the apparent Mach number accounts for rupture directivity, depending on the receiver view angle and the rupture to wave velocity ratio. In (13) the relation between the peak slip velocity and dynamic stress drop is inferred from the dynamic models of a propagating shear crack by Kostrov (Kostrov, 1964) and Dahlen (Dahlen, 1974).

Averaging over $\theta$, eq (13) changes to:

$$\Omega_c(t) \approx \frac{2\pi\, C(v_R)\tau_e}{\mu} t^2 \qquad (14)$$

where the rupture velocity factor

$$C(v_R) = \frac{\pi}{2} \frac{v_R^3 \left(2 - \left(\frac{v_R}{v_P}\right)^2\right)}{\left(1 - \left(\frac{v_R}{v_P}\right)^2\right)^{\frac{3}{2}}} \quad (15)$$

shows an exponential increase with $v_R$. According to eq (14), both the rupture velocity and/or dynamic stress drop control the rise of the radiated P pulse displacement and therefore its initial slope.

An example of the effect of a varying rupture velocity with magnitude on LPDT curves and slope by assuming a Sato and Hirasawa (1973) kinematic source model of a circular shear crack is presented in Chapter 5. Synthetic tests support the idea that a decreasing value of rupture velocity with magnitude could be responsible for the observed decrease of the initial slope of P-wave displacement. Additional constraints provided by more complex and realistic numerical simulations are necessary to understand in which physical conditions and how these two parameters may play a role during the initial stage of the rupture propagation.

## 1.4 The open debate of the earthquake rupture behavior: the earthquake nucleation models

The different observations coming either from laboratory experiments or from the analysis on the early signals of real earthquakes data are rooted in the models describing the earthquake nucleation phase. These models were proposed and discussed by Ellsworth and Beroza (1995) and Beroza and Ellsworth (1996). In their studies ((Ellsworth and Beroza, 1995), (Beroza and Ellsworth, 1996)), they denoted the nucleation phase as the difference between the first arriving P-wave and the observed sudden increase in growth of the velocity seismograms. They also defined the beginning of the linear increase in ground velocity as the *breakaway phase*. They evaluated the size and the duration of the defined seismic nucleation phase for 48 earthquakes with magnitudes ranging from 1.1 to 8.1. They found the size and the duration of the nucleation phase showed a scaling with the total seismic moment of the events. The characteristics of seismic nucleation allowed two possible interpretations that were summarized into two physical models, the *cascade model* and the *preslip model*. Both two models are still widely discussed for the relevant implications that would carry on the earthquake determinism debate.

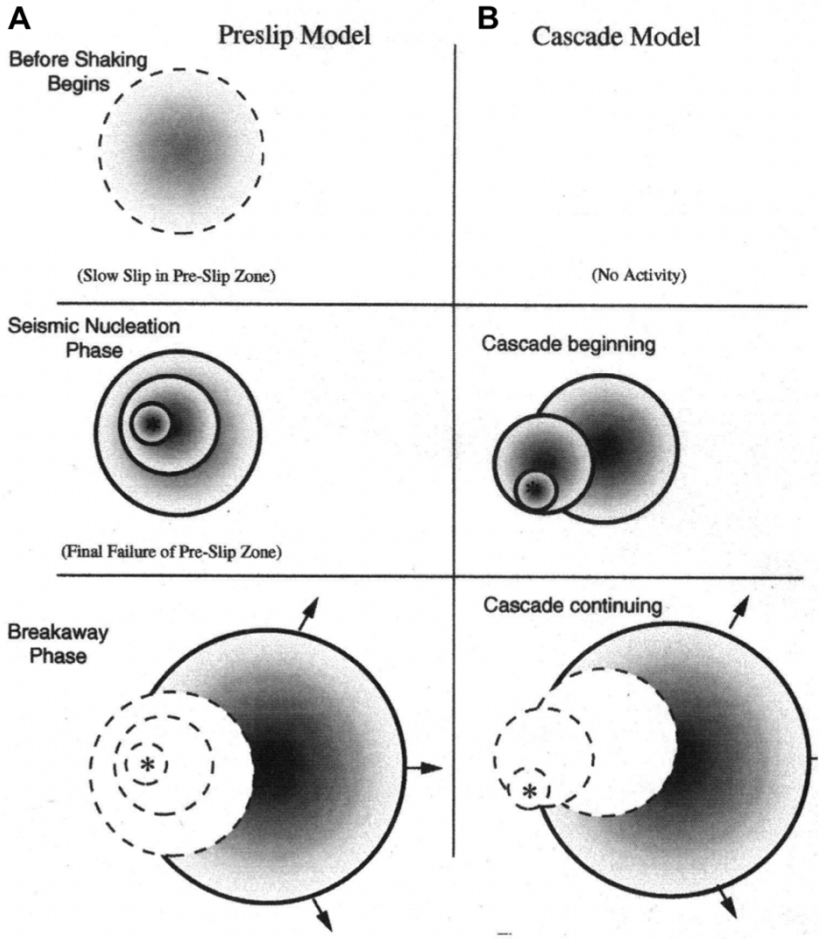


*Figure 1.4.1: Preslip and cascade model sketch. In the pre-slip model an episode of slow, aseismic slip precedes dynamic rupture and establishes the dimensions of the nucleation zone. In the cascade model there is no activity before the mainshock begins. The seismic nucleation phase is generated either when slip in the aseismic nucleation zone accelerates to dynamic rupture velocity (preslip model panel A) or when spontaneous failure triggers a series of triggered subevents (cascade model panel B) ((Ellsworth and Beroza, 1995)).*

According to the *cascade model* (Panel B of Figure 1.4.1), earthquakes begin abruptly and there is no difference between the beginnings of large and small events. A large earthquake happens when a smaller earthquake can trigger a cascade of events of increasingly larger slip. In this model view, seismic nucleation is an accumulation of smaller events that leads to the largest subevent of the earthquake. The breakaway phase is represented by the first large slip event of the cascade. In the cascade model, any observable scaling between source parameters during the seismic nucleation and the source parameters for the entire earthquake might arise only if the last jump in subevent size also characterizes the final size of the earthquake.

According to the *preslip model* (Panel A of Figure 1.4.1), the beginnings of large and small earthquakes are different. In this model view, failure starts aseismically in a region which represents the pre-slip zone. This pre-slip zone gradually becomes larger and larger

and the slip within this region increases until it reaches a critical size. Following the preslip model, the nucleation phase represents the last stage of the failure process within the preslip zone, whereas the breakaway phase is generated as soon as the rupture breaches the preslip zone and begins to propagate along the seismic fault.

In the pre-slip model, any observable scaling of the source parameters related to the nucleation are controlled with the final earthquake size is controlled by the critical length of the preslip zone. Indeed, any existing scaling between the nucleation phase and the final stage of the earthquake is explainable if it is considered that the final size of the earthquake is determined by the slip amplitude when the breakaway stage begins. In simple words, according to the preslip model, an earthquake becomes large because the "push" at its beginning is large.

If the cascade model is correct like some observations seem to point out (see paragraph 1.3.1), the outlook for the short-term earthquake prediction is unpromising. To predict large earthquakes that are the most interesting target of the Earthquake Early Warning, one would have to predict the small event that initiates the cascade together with the conditions that leads to the cascade triggering on the fault. On the other hand, if the pre-slip model is correct as other observations seem to show (in paragraph 1.3.1), the short-term earthquake prediction is more feasible, because earthquakes would be preceded by precursory slip episode having different initial size which would lead to different final size.

Until now, there is still no definitive evidence on which model is the right one to describe the earthquake nucleation and to state whether the earthquake rupture has a deterministic behavior or not. We presented a summary of contradictory results from a wide range of data showing that the answer remains unclear. Putting a closure to the long debate on earthquake nucleation and its implication relative to the final earthquake size would not only mean a great success in understanding the earthquake physics but would also represent a milestone for the Earthquake Early Warning future developments.

# CHAPTER

# 2 Implementation of Earthquake Early Warning

## 2.1 Earthquake Early Warning Systems around the world

In this paragraph, we present a brief description of the status of EEW systems around the world following the overviews by Allen and Melgar (2019) who reviewed the worldwide status of EEW and Clinton et al. (2016) who reviewed EEW state of art in Europe. Following their scheme presented in Figure 2.1.1 we can divide the characteristics of EEW systems into three categories: systems deploying public alerts; systems deploying limited alerts to selected users and systems under construction and real-time testing.

Mexico's system SASMEX (Aranda et al., 1995) issues alert through radio receivers mostly located in schools and offices in multiple cities. Particularly, in Mexico City the alert makes 12.000 sirens sound so that most residents can hear and act. The alert is triggered when two stations detect an earthquake and estimate the likely magnitude to be significant. The threshold for alert issuing is set at M>5 for two stations as far as 300 km from Southern Mexican coast. The national EEW system in Japan is managed by the

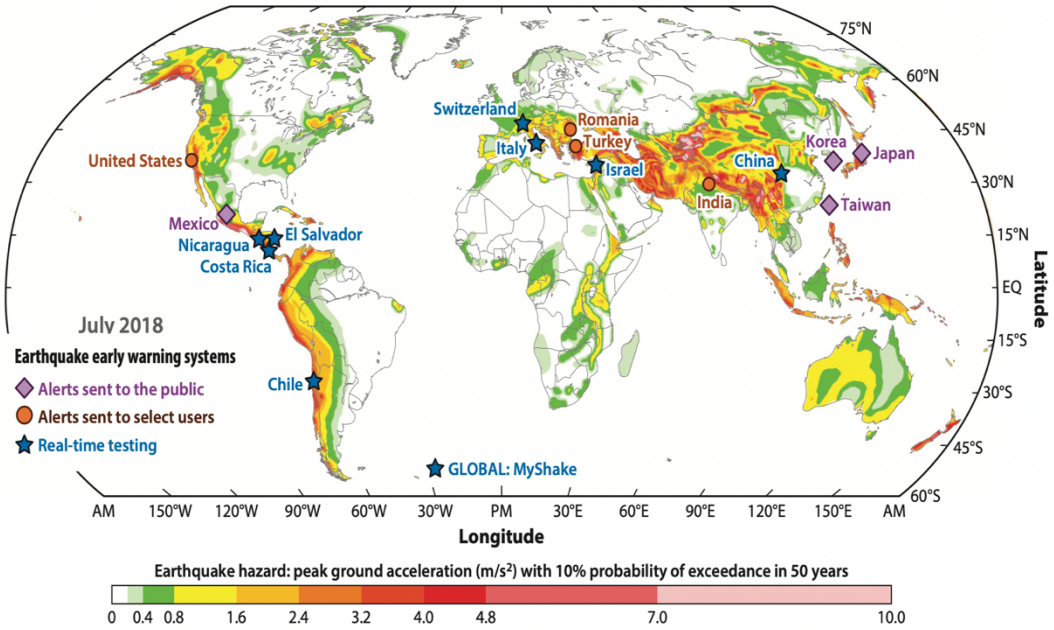


*Figure 2.1.1: Status of EEW systems around the globe. Purple diamonds represent systems that deliver public alerts; red circles represent systems that deliver alerts to a limited number of users; blue stars represent systems under real-time testing. The map shows the earthquake hazard in peak ground acceleration with 10% probability of exceedance in 50 years. (from Allen & Melgar (2019))*

Japan Meteorological Agency (JMA). Alerts are issued through different channels: from cell phones to radio and TV. The JMA intensity level set as threshold is 5-lower. Before

the 2011 M9.1 Tohoku-Oki earthquake, the JMA system used a source point algorithm to locate and estimate magnitude, based on the first few seconds of P-waves. This massive earthquake caused significant shaking over a much larger area than predicted by EEW algorithms, as the expected magnitude saturated around M~8. The great Tohoku-Oki earthquake effectively re-opened the discussion among the scientific community about EEW effectiveness in case of large events. Since then, great efforts were applied to improve the system reliability which is now moving towards impact-based algorithm (Kodera et al., 2018a). We will discuss both approaches later in this chapter.

China's Earthquake Early Warning (EEW) efforts are primarily driven by the China Earthquake Administration (CEA) and various research institutions. Over the past decade, they have deployed increasingly dense seismic networks in quake-prone areas such as Sichuan and Yunnan, working to reduce detection times and improve alert accuracy (Peng et al., 2022). Several pilot EEW systems are now in place, utilizing real-time data and advanced algorithms to estimate magnitude and epicenter location (Peng et al., 2021). Ongoing research focuses on refining detection strategies, enhancing sensor coverage, and ensuring system redundancy to better protect urban centers and critical infrastructure across the country (Liu and Liu, 2024) .

In South Korea, public alerts are issued by the Korean Meteorological Administration in the form of text messages sent to cell phones for earthquakes with magnitude M>4. Earthquakes characterization is assessed through ElarmS point source algorithm (Sheen et al., 2017).

Taiwan uses three EEW systems. All of them are P-wave-based system to predict the coming peak shaking (Hsu et al., 2018; Wu et al., 2019).

On the West Coast of United States, the EEW system *ShakeAlert* is fully operational (Kohler et al., 2020). The system combines EPIC point source algorithm (Chung et al., 2019) and finite fault detector FINDER algorithm (Böse et al., 2018) to estimate magnitude, location and expected shaking intensity. Additionally, the MyShake app (Kong et al., 2016) has been sending alerts to users since its first public lunch in 2019. Started as a project at University of California, Berkeley, MyShake is also collecting

waveforms recorded by smartphone that could be used to predict peak ground shaking using accelerometers built in cell phones (Patel and Allen, 2022).

In Europe, different countries have now systems that issue alerts to a limited number of users or facilities (Clinton et al., 2016).

In Italy, PRESTo, a source-based algorithm is running for the Irpinia Region with the goal of issuing alerts in Naples and surrounding areas (Satriano, Elia, et al., 2011). Recently, the regional approach to early warning has been extended to include real-time estimation of the Potential Damage Zone (PDZ) i.e the area where the expected shaking intensity is higher than a threshold. The PDZ is obtained by the real-time mapping of observed and predicted P-peak displacement amplitudes (Zollo et. al, 2023). Together with the network system PRESTo, an on-site algorithm (SAVE) is also running on the stations of the Irpinia Seismic Network (ISNet) (Caruso et al., 2017). SAVE provides real-time information about the expected shaking at the sites where the stations are located. We discuss SAVE algorithm, presenting several applications in Chapter 3. Furthermore, ISNet is associated with the European platform CREW, the Testing Centre for Early Warning and Rapid Source Characterization, where the performance of Early Warning software is evaluated and compared.

In Switzerland, the Virtual Seismologist (VS) algorithm (Cua and Heaton, 2007) has been operating as a test system since 2008. VS is a network-based Bayesian approach to EEW. The VS magnitude relationships are derived using a Southern Californian dataset augmented with strong motion from Next Generation Attenuation Relationships (NGA). A key advantage of this method is that the station magnitude estimates are evolutionary (using the entire waveform available at a given time and not just the first few seconds). This means that source parameter estimates are updated with new data every second even if no new P-wave detections have been recorded.

Romania is also using PRESTo together with its own event validation approach to send alerts to a nuclear research facility (Clinton et al., 2016).

In Turkey, Istanbul has a warning system that issue alerts when acceleration exceeds a threshold at three stations of the network across the city, called Istanbul earthquake Early Warning (IEEW). After triggered by an earthquake, each station will process the streaming strong motion to yield the spectral accelerations at specific periods and will

send these parameters in the form of SMS messages to the main data center through available network service (Erdik et al., 2003).

## 2.2 Earthquake Early Warning Configurations

Depending on the deployment of the seismic networks, it is possible to distinguish two configurations for EEW systems: the network-based systems and the stand-alone, on-site systems. A variant of the on-site configuration is the barrier system, in which a barrier-shaped seismic network is deployed between the source region and the target site to be protected. The main difference between the network and the on-site (with barrier variant) EEWS is to be found in the time interval available to issue an alert soon after the rapid detection and characterization of the on-going earthquake due to the fact that the monitoring network is located the source region of earthquakes, while the onsite system is located at the target site to protect.

### 2.2.1 Network systems

In a network system, seismic stations are deployed near active faults (Figure 2.2.1). In this configuration, the information carried within the first P-wave arrival is used to rapidly estimate earthquake magnitude and location. The fast characterization of earthquake source is then used to make predictions of the expected damage in areas far from event epicenter using regional empirical attenuation relations or ground motion prediction equations (GMPE). The available time to issue an alert in this configuration goes from few seconds for those areas close to event epicenter to several tens of seconds for farther areas.

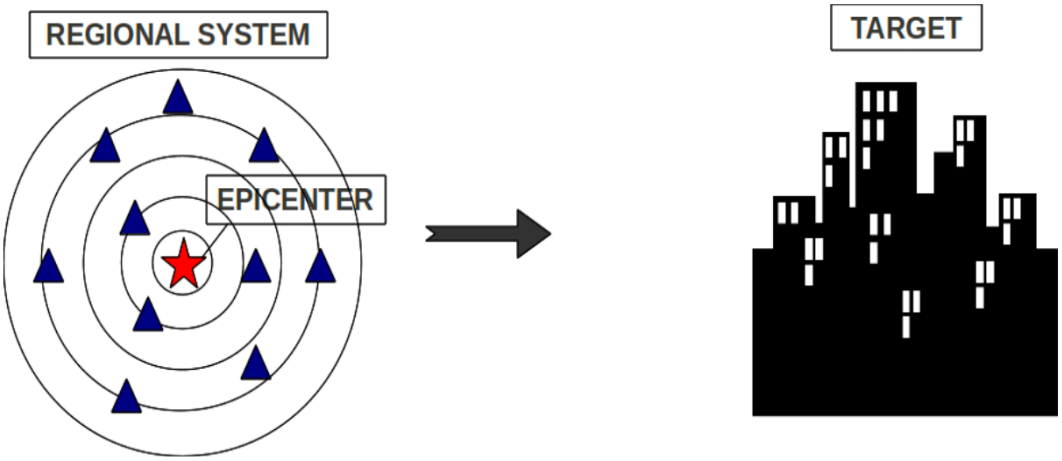


*Figure 2.2.1: Regional EEWS scheme*

The *lead-time*, that is the time between the arrival of damaging seismic waves at the target and the time of first issued alert, is here defined as:

$$\Delta t_R = t_{S,target} - (t_{FA} + \mathrm{t}_{elab}) \quad (16)$$

where $\Delta t_R$ is the theoretical lead-time, $t_{S,target} = t_o + T_s$ ($t_o$ origin time, $T_s$ wave propagation time) is the S-wave arrival time to the target and $t_{FA} = t_o + T_P^{last}$($T_P^{last}$ P-wave propagation time at the last station considered for the analysis) is the time of first alert, which can be issued taking into account the analysis of one or more P-wave signals recorded at seismic stations of the network. In the definition of the theoretical lead-time, it is also added the time for data acquisition and elaboration ($\mathrm{t}_{elab}$), which is usually of few seconds, depending on the communication speed, latency of the data transmission and computing time efficiency of the real time algorithms. In a network-based EEW configuration, the S- waves generally arrive at the area located really close to event epicenter before the alert is issued. This area is called *blind zone* and its radius is evaluated as it follows:

$$R_{BZ} = V_s(t_{FA} + \mathrm{t}_{elab} - t_o) \quad (17)$$

where $V_S$ is the average S-wave velocity in the medium. The extension of the blind zone depends on the seismic network density, on the number of seismic stations used to issue the first alert, on the time required for signals acquisition and elaboration and on the earthquake depth.

#### *2.2.1.1 Source-based approach*

The implementation of EEW has known a great acceleration thanks to the digitalization of seismic instruments and communications to issue alerts. The algorithms which have been developed in EEW systems worldwide can be summarized into two big categories: source-based algorithms and wavefield-based algorithms. The former uses the information coming from the propagation of P- and S- waves (typically the first few seconds) to estimate source parameters (origin time, location and magnitude). The source characterization is required to obtain the expected ground shaking at the site of interest. The expected ground shaking is evaluated through an appropriate Ground Motion Prediction Equation (GMPE) that link source parameters to the peak ground motion and

***Box 2.2.1: RTLoc***

It is assumed that a seismic network has known sets of operational and nonoperational stations. When an earthquake strikes, P-wave arrivals will become available from some operational stations. We consider N operational stations ($S_0 \dots S_N$), a gridded search volume V containing the network and the earthquake source regions, and the travel times from each station to each grid point $(i, j, k)$ in V computed for a given velocity model. According to the Equal Differential Time (EDT) approach, if the hypocenter $(i, j, k)$ is exactly determined, the difference between calculated travel times $tt_n$ and $tt_m$ from the hypocenter to two stations $S_n$ and $S_m$ is equal to the difference between the observed travel times tn and tm at the same stations:

$$(tt_m - tt_n)_{i,j,k} = t_m - t_n; \quad m \neq n$$

For a constant velocity model, the above equation defines a 3D hyperbolic surface whose symmetry axis cross stations $S_n$ and $S_m$. Giving N triggering, $N(N-1)/2$ surfaces can be drawn and the hypocenter will be located in the small region having the maximum number of EDT surfaces crossings. If we take into account the not-yet-triggered stations and we consider $t_n = t_{now}$ the time at which the n-th station is triggered, the EDT surface is bounded by the inequality:

$$(tt_l - tt_n)_{i,j,k} \geq 0; \qquad l \neq n$$

where $S_l$ is the not-yet-triggered station and $tt_l$ is its calculated travel time. As the current time tnow progresses, the hypocentral volume is more and more constrained around the actual earthquake location, bounded by the information that not-yet-triggered station can only have observed $t_l > t_{now}$. This leads to the following inequality satisfied by EDT surface:

$$(tt_l - tt_n)_{i,j,k} \geq t_{now} - t_n$$

that includes ground motion propagation models. The wavefield-based algorithms are completely different from source-based approaches because they do not ground on the earthquake source characterization. They make use of the observation of the impending strong shaking to predict shaking at other locations. In this sense, the wavefield-based

approach is not sensitive to earthquake detection or uncertainties coming from location and magnitude estimation since it is completely data driven.

The techniques for fast real-time earthquake location are mostly based on a probabilistic approach, where both the stations that already recorded the event and the stations that still have not received the signal are used to obtain the earthquake hypocenter. In the box 2.2.1 the concept of the real-time location (RTLoc) is briefly described (Satriano et al., 2008).

The magnitude characterization in real-time for EEW purposes is still a matter of great debate in the seismological community. In recent years, the fast magnitude estimation from early seismic signals has opened the way to the possibility of a deterministic behavior of the earthquake rupture ((Colombelli et al., 2014),(Colombelli et al., 2020)) that has been extensively discussed in Chapter 1. In operating EEW systems around the world, the magnitude estimation is performed through modules that link the early P-peak amplitude or frequency to the earthquake final size, such as PRESTo regional system (Satriano et al., 2011) and the EPIC algorithm in U.S ShakeAlert (Chung et al., 2019).

Nakamura, (1988) proposed the measure of a predominant frequency from the first P-wave train. Since then, the method has been extensively applied in EEW showing that the predominat period $\tau_{max}^{P}$ parameter scales with magnitude regardless of epicentral distances up to few hundred kilometers (Allen and Kanamori, 2003). Alternatively, to $\tau_{max}^{P}$, a similar characterist time parameter that scales with magnitude is the average period of the P-wave signal $\tau_c$ (Wu and Kanamori, 2005b). Although the measure of $\tau_c$ parameter is scattered around the magnitude, the scaling with the earthquake final size is preserved for different region of the world, making its use appealing in source-based approaches. We provided a mathematical description of $\tau_{max}^{P}$ and $\tau_c$ in the box 1.2.1. The $\tau_{\mathrm{max}}^{\mathrm{P}}$ and $\tau_{\mathrm{c}}$ approaches that we described for rapid magnitude estimation are largely implemented in EEW systems.

However, they underly the point-source approximation. The point-source approximation is valid until a certain range of magnitude (from small to moderate) (Aki and Richards, 2009) depending on the signal frequency content and distance of the observer. Above this physical threshold, the rupture complexity cannot be recovered completely because it affects signal amplitude, frequency and duration such that the point-source approximation cannot describe the radiated signal complexity. Moreover, the use of a signal time window too short as compared to the one related to the magnitude related rupture length could

lead to a saturation in magnitude estimation, which might result in a failure of the designed EEW system.

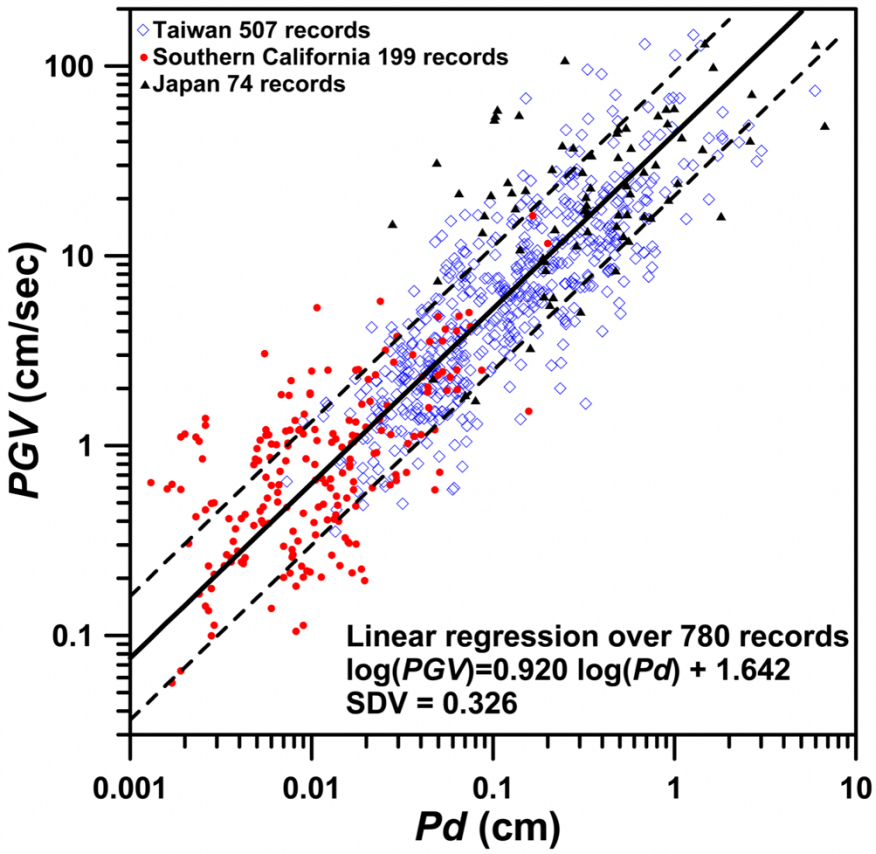


*Figure 2.2.2: Relationship between peak initial three-second displacement amplitude (Pd) and peak ground velocity (PGV) for 780 records with the epicentral distances less than 30 km for Japan (black triangles), southern California (red solid circles) and Taiwan (blue diamonds). Solid line indicates the least squares fit and the two dashed lines show the range of one standard deviation.*

Indeed, EEW algorithms that measure the rupture extent in real-time have recently been developed and their advantages become clear at the occurrence of great events. It is worthy to mention the Finite-Fault Rupture Detector (FinDer) (Böse et al., 2018), which is a module for line-source parameters estimation implemented the U.S. ShakeAlert. FinDer determines earthquake rupture extent from the observed distribution of near-source high-frequency motions. Based on template matching methodology, FinDer determines line-source models from the real-time recorded PGA at a dense network around the epicenter, very rapidly and continuously updates these parameters during the fault rupture development. The application of a finite-fault detector improves the accuracy of the magnitude estimation and consequently, the accuracy of ground motion parameters.

The prediction of the expected Peak Ground Motion (e.g PGA, PGV, PGD) is performed through the use of empirical attenuation relationships or Ground Motion Prediction Equations (GMPE). The simplest form of the GMPE is:

$$logPGX = A + BM + ClogR \quad (18)$$

where X=Acceleration, Velocity, Displacement; coefficient A, B, and C are locally calibrated; M and R are the magnitude and the hypocentral distance evaluated through EEW approaches described in previous paragraphs. More complex shaped GMPE are proposed in literature, including higher order terms in magnitude, depth dependency and site amplification terms (Douglas, 2018).

#### *2.2.1.2 Wavefield-based approach*

As an alternative to source-based methods, another approach has recently been developed, which does not require earthquake source parameters estimation to predict the impending ground motion. This approach is solely based on the propagation of wavefield and predicts the expected ground motion directly from the observed ground motion in real-time. For this reason, this kind of approach is referred to as "wavefield-based method" or "ground motion-based method". The wavefield-based method for EEW has been successfully tested in Japan and California ((Kodera et al., 2018b) (Cochran et al., 2019)). In Italy and in Turkey, the wavefield-based approach has been tested using P-wave information: M and R are determined in real-time to interpolate the GMPE at nodes where instruments are not deployed ((Zollo et al., 2023), (Rea et al., 2024)). Especially for large earthquakes, the wavefield-based approach has been proved to be particularly suitable, because it skips rupture duration and length estimation, which for high energetic events could lead to poor resolution using the standard empirical relationships of source-based methods. The propagation of *local undamped motion* (PLUM) method (Hoshiba, 2013) has been implemented in JMA's EEW system since 2018. As a wavefield-based approach, PLUM predicts seismic intensities directly from observed real-time seismic intensities near the target site. The basic principle of PLUM is that under the assumption of plane wave propagation, the maximum amplitude between the prediction and the observation point is preserved when the distance between the former and the latter is sufficiently short compared to the hypocentral distance. Following this approximation, seismic intensities are predicted by (Kodera et al., 2018b):

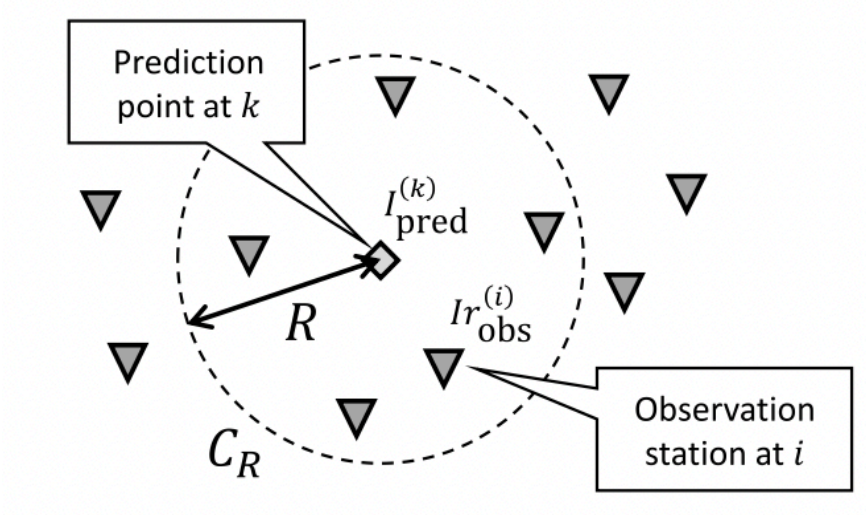


*Figure 2.2.3: Schematic diagram of the ground-motion prediction (GMP) process in the propagation of local undamped motion (PLUM) method. The diamond indicates a prediction point, and the inverted triangles represent observation stations (from (Kodera et al., 2018)).*

$$I_{pred}^{(k)} = \max_{i \in C_R} \left\{ Ir_{obs}^{(i)} - F_0^{(i)} \right\} + F_0^{(k)} \qquad (19)$$

where $I_{pred}^{(k)}$ is the predicted seismic intensity at the prediction point $k$, $I_{r\,obs}^{(i)}$ is the observed real-time intensity at point $i$, $F_0^{(i)}$ and $F_0^{(k)}$ are the site amplification factors converted into seismic intensity. $C_R$ denotes a circular area centered on the prediction point (as in Figure 2.2.3). The predicted intensity is obtained as the maximum of the observed seismic intensity in $C_R$. The radius R of the circular area can be evaluated either in an empirical way or by considering the spatial density of the seismic network. The prediction points of the PLUM method consist in about 4200 sites displaced all over Japan where seismic-intensity meters are located.

The warning times from the PLUM method are usually shorter than the warning times from source-based algorithms. The main reason is that the PLUM algorithm does not use the P-wave information available before S-waves.

On this matter, the evolutionary shaking-forecast-based EEW method (Quake-Up) proposed by Zollo et al. 2023 (Zollo et al 2023) has shown that a P-wave based early shake map is feasible and increases the available warning times with respect to other ground motion-based approaches. The core of Quake-Up is the mapping of the real-time evolutionary Potential Damage Zone (an area of expected strong ground shaking), using the information coming from the onset P-waves. The early shake map is updated while

the P-time window of the recorded signal is expanding. Moreover, the evaluation of the ground motion is performed considering both the recording sites, where the P-wave arrivals are available, and the "virtual nodes", points of the gridded 3D space around event location which are not instrumented. Particularly, the expected Peak Ground Velocity at the recording site at time *t* is obtained through:

$$logPGV_x^t = D_x \cdot logP_x^t + E_x \tag{20}$$

where $D_x$ and $E_x$ are empirically estimated coefficients, $P_x^t$ is the P-peak at time *t* of *x* which stands for acceleration, velocity and displacement. The predicted $PGV_{onsite}^t$ is obtained as a weighted mean of the three estimated $PGV_x^t$. The prediction of PGV at the non-instrumented nodes of the grid map is obtained through a combination of the available information from recording sites and the interpolation using regional scaling relationships as it follows:

$$PGV^t(x,y) = \frac{\sum_{i=1}^{N}\left[\frac{1}{\sigma_{onsite}^{i\,2}} \cdot PGV_{onsite}^{t\,i}(x,y)\right] + \frac{1}{\sigma_{GMPE}^2} \cdot PGV_{GMPE}(x,y)}{\sum_{i=1}^{N}\left[\frac{1}{\sigma_{onsite}^{i\,2}}\right] + \frac{1}{\sigma_{GMPE}^2}} \tag{21}$$

where $PGV_{onsite}^{t\,i}(x,y)$ is the PGV predicted at i-th network station from P-peak amplitudes, $PGV_{GMPE}(x,y)$ is the PGV predicted by a regional GMPE, $\sigma_{onsite}^i$ and $\sigma_{GMPE}^2$ are the standard error related to the P-wave predicted PGV and the standard error related to the GMPE predicted PGV, respectively. The standard error for PGV of recording site takes into account the standard deviation of the PGV versus $P_x$ relation and the distance between the network node and the virtual node. The final output is the predicted PGV versus time at any location (x,y) around the earthquake source, which can be converted in instrumental intensity according to regional scaling laws.

### 2.2.2 On-site systems

In an on-site EEW system, a single sensor (or a small array of sensors) is usually deployed near a target to be secured during the earthquake occurrence (Figure 2.2.4). The stand-alone design of on-site systems makes them suitable for sites located within several tens of km from active faults areas, at distances where typically extends the blind-zone of network-based EWS. In this configuration, the information carried by the early P-waves is used to predict the expected ground shaking at the target. Indeed, in an on-site configuration, the magnitude and the hypocentral measurements are usually not available.

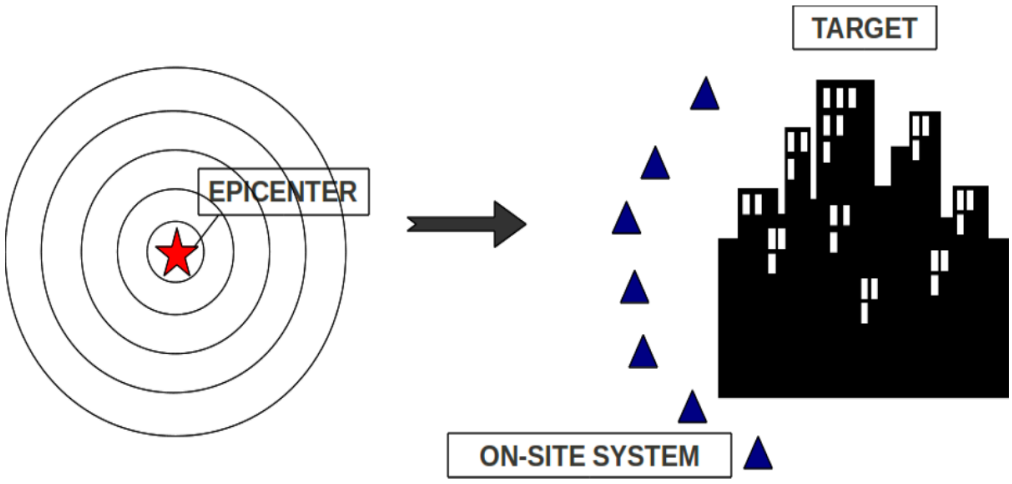


*Figure 2.2.4: On-site EEWS scheme*

The expected Peak Ground Motion is obtained through empirical scaling relations that link PGX to the peak amplitude of P-waves (Wu e Kanamori 2008, Zollo 2010). These empirical laws can be written as follows:

$$logPGX(PTW) = A(PTW) + B(PTW)logPx(PTW) \tag{22}$$

where $Px$ is P-peak of acceleration, velocity or displacement measured in the P-wave time window of length PTW; A and B are locally calibrated (e.g. taking into account regional variability as it is shown in Figure 2.2.2 from Wu e Kanamori (2008)).

Finally, the expected Peak Ground Motion is converted into expected shaking intensity through regional laws that link PGX to seismic intensity (e.g. Modified Mercalli Intensity MMI) ((Faenza and Michelini, 2010), (Worden et al., 2012), (Bilal and Askan, 2014)).

The lead-time for an on-site system design is evaluated as:

$$\Delta t_R = t_{S,target} - (t_{P,target} + t_{elab}) \tag{23}$$

where $t_{P,target} = t_o + T_P$ is the P-wave arrival time at the target; $t_{S,target}$ is the S-wave arrival time at the target and $t_{elab}$ is the latency/computational time that is generally assumed to be 3 sec, considering the minimum P-wave window length for the analysis. On one hand the on-site design decreases the radius of the blind zone because the alert is issued directly at the target; on the other hand, it increases the false alarm likelihood, because predictions are based on one (or very few) sensor.

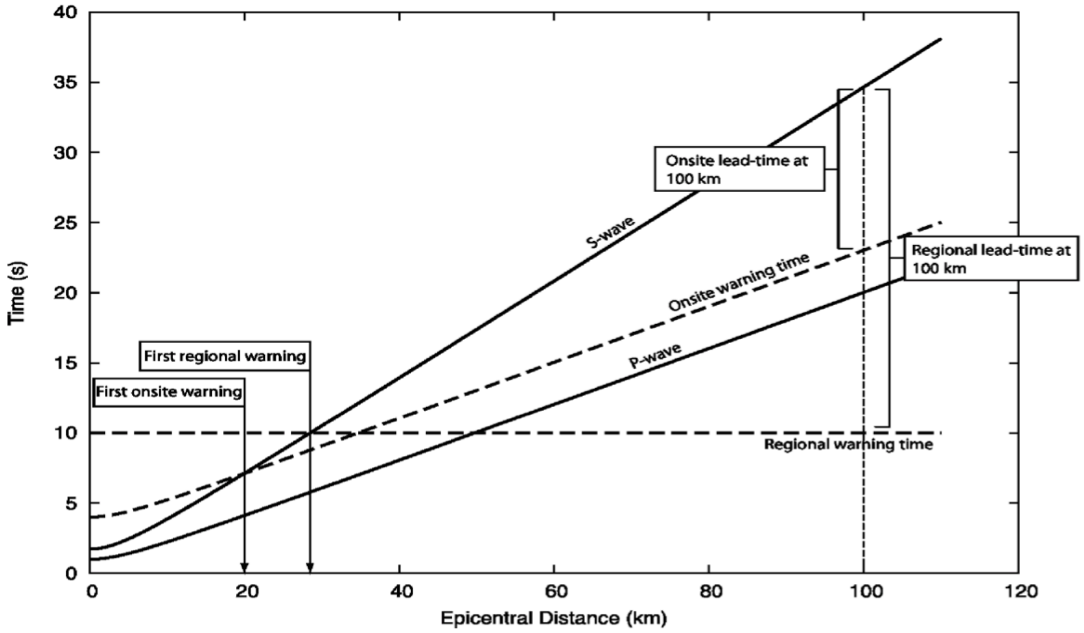


*Figure 2.2.5: Comparison of warning times and lead-times for onsite and regional EEW approaches. The onsite warning time depends on the P arrival time at the site and on a (generally) fixed analysis window (here set to 3 s). The regional warning time depends on the source-network geometry and on the algorithms employed and is generally of the order of a few seconds (e.g. 10 s). An onsite system can provide a warning to targets closer to the epicenter. (from (Satriano, Wu, et al., 2011))*

However, the main factor which makes the two designs complementary is the lead-time. This parameter increases with the epicentral distance both for the regional and the on-site system. Regional systems are characterized by greater lead-times with respect to on-site systems at the same distance (see Figure 2.2.5). There is a trade-off between the amount of time required for alert issuing and the precision of earthquake parameters on which the declaration of an alert is based. Generally, the bigger the time required for data acquisition and earthquake characterization, the more precise the estimation is (and consequently the alert). It is also true that increasing time to get precise source estimates corresponds to an increase of blind zone radius. For this reason, a hybrid design is usually the preferred strategy, where a network configuration is joined by an on-site configuration that validates/invalidates the information evaluated from the former when an earthquake strikes in the monitored fault area.

# PART 2 – ON-SITE EARTHQUAKE EARLY WARNING: METHODS AND APPLICATIONS

In the framework of fast characterization of the earthquake source, the on-site earthquake early warning systems represent the step that turns rapid algorithms for source parameters estimation into operational systems issuing alerts. As described in paragraph 2.2.2, an on-site system can work with a single sensor and evaluate the expected shaking intensity from few seconds of signal at the site where the system is deployed. The on-site EEW systems are usually preferred over the regional systems when the target to be secured is close to an active fault area or when the target site falls within the radius of the blind zone of a regional system. In the blind zone (mentioned in paragraph 2.2), the most damaging S- or surface waves reach the target before any alert could be issued. Indeed, most of the algorithms in the on-site systems are implemented as P-wave based algorithms, meaning that the earthquake is rapidly characterized by looking solely at the P-wave phase of the signal. Moreover, every operation performed on the seismogram, from the detection to the alert issuing, is done at the site where the system is. This reduces eventual delays for warning declarations that might come from latencies in electromagnetic signal transmissions. In this part we describe two on-site systems, SAVE and P-Alert, and their application to different real earthquakes scenarios.

# CHAPTER

# 3 On-Site Alert Level System: SAVE

## 3.1 SAVE theoretical concepts

In this paragraph we describe the on-Site Alert Level system (SAVE, hereinafter) implemented by (Caruso et al., 2017). SAVE is a P-wave based on-site early warning system. SAVE processes the vertical component of accelerometers and (broadband) velocimeters. Through the measurement of P-peak amplitude and early P-wave frequency content SAVE predicts the expected ground shaking at the recording site and issues a local alert level together with a qualitative assessment of earthquake magnitude and source-to-receiver distance. The block diagram of SAVE is shown in Figure 3.1.1. In the following sections we focus on each single step of SAVE operations from the automatic detection of P-wave on records until the final outputs of the system. Herein after we

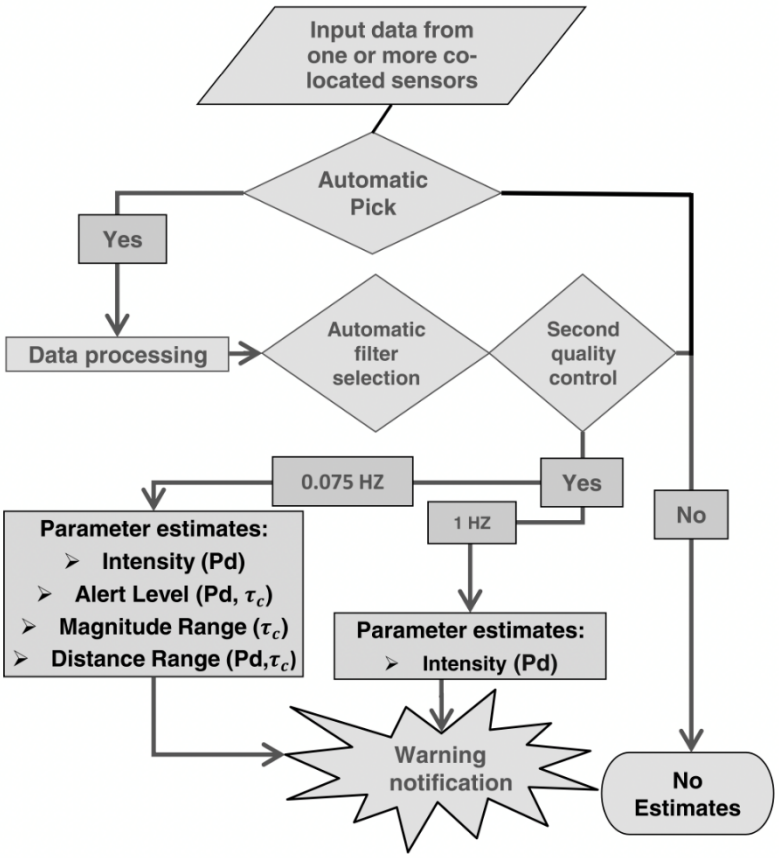


*Figure 3.1.1: block diagram of SAVE (from (Caruso et al., 2017))*

describe in detail the following modules of the onsite EW system: (1) the automatic P-wave picking, (2) the Data Quality Control, (3) the parameters estimates.

### 3.1.1 Automatic P-wave picking

The P-wave picking algorithm implemented in SAVE is FilterPicker (FP hereinafter) by Lomax (Lomax et al., 2012). FP is optimized for EEW as it operates on data packets of different lengths and can declare a P-wave pick within few samples from the trigger. A mathematical description of FP is provided in box 3.1.1.

***Box 3.1.1: The FilterPicker Algorithm***

The FilterPicker (FP hereinafter) operates on a discretized time- series signal $y(i)$ with sample interval $\Delta T$. The FP algorithm makes use of decay constants for accumulating time-averaged statistics on the signal independently of the elapsed time since the start of the signal. For a statistic $S = f(y)$, the time-averaged value $S_{long}$ is given by:

$$S_{long}(i) = C_{long} S_{long}(i-1) + (1 - C_{long}) S(i) \quad \text{(I)}$$

where $S(i)$ is an instantaneous value of $S$ and $C_{long}$ :$0 \leq C_{long} < 1$ is a decay constant defined by $C_{long} = 1 - \Delta T / T_{long}$ where $T_{long}$ is a time-averaging scale.

To perform the picking, the first step is to obtain a differential signal y'(i) as:

$$y'(i) = y(i) - y(i-1) \quad \text{(II)}$$

In the next step, a set of filtered signals $Y_n(i) = Y_n^{LP}(i)$ {n=0, $N_{band}$-1} are generated from y'(i) using two simple one-pole high-pass filters:

$$Y_n^{HP1}(i) = C_n^{HP}[Y_n^{HP1}(i-1) + y'(i) - y'(i-1)] \quad \text{(III)}$$

And

$$Y_n^{HP2}(i) = C_n^{HP}[Y_n^{HP2}(i-1) + Y^{HP1}(i) - Y^{HP1}(i-1)] \quad \text{(IV)}$$

Followed by one simple one-pole low pass filter,

$$Y_n^{LP}(i) = Y_n^{LP}(i-1) + C_n^{LP}[Y^{HP2}(i) - Y^{HP2}(i-1)] \quad \text{(V)}$$

With filter constants $C_n^{HP} = \omega_n/(\omega_n + \Delta T)$ and $C_n^{LP} = \Delta T/(\omega_n + \Delta T)$, time constant $\omega_n = T_n/2\pi$, corner period $T_n = 2^n \Delta T$, $y'(0)$, $Y_n^{HP1}(0)$ and $Y_n^{HP2}(0)$ initialized to 0.

***Continue Box 3.1.1***

$N_{band}$ is chosen so that $T_{N_{band}-1} = 2^{N_{band}-1}\Delta T$ is greater than the largest dominant period of the phase to be picked. In the following step, we construct an envelope $E_n$ function for each band n:

$$E_n(i) = Y_n^2(i) \qquad \text{(VI)}$$

and a characteristic function $F_n^C(i)$:

$$F_n^C(i) = \frac{E_n(i) - <E_n>(i-1)}{<\sigma(E_n)>(i-1)} \qquad \text{(VII)}$$

Where $< E_n > (i-1)$ and $< \sigma(E_n) > (i-1)$ the time-averages up to sample *i-1* of $E_n$ and the standard-deviation of $E_n$ respectively, are accumulated using the decay constant $C_{long}$ of equation (I). In the final step, a single summary CF, $F^C(i)$, is formed by setting $F^C(i) = max\{F_n^C(i); n = 0, N_{band} - 1\}$. A trigger is declared when $F^C(i) \geq S_1$, where $S_1$ is a predefined threshold and the corresponding trigger time $t_{trig}$ is stored. Given a predefined time width $T_{up}$, a pick is declared if and when the integral of $F^C(i)$, $\sum_{up} F^C(i)\Delta T$, exceed the value $S_2$*$T_{up}$ within a window up from $t_{trig}$ to $t_{trig}$+$T_{up}$.

The threshold $S_2$ is also predefined.

FP has few parameters, all of which are not difficult to set and can easily adapted to the type of signal and to the phase to be picked.

### 3.1.2 Data Quality Control

When a P-wave is detected, the waveform enters in a preprocessing module that removes the average and the linear trend and is integrated (once or twice depending on the type of waveform) to get displacement. After the preprocessing step, the signal goes through two quality controls. The first quality control is performed to assess whether to keep the signal or to discard it. The first quality control is based on the analysis of the Signal-to-Noise Ratio. Indeed, the waveform is automatically discarded if:

$$20 \cdot \log\left(\frac{P_d^{PTW}}{P_{d\ NOISE}}\right) < SNR_{threshold} \tag{24}$$

where $P_{d\ NOISE}$ is the average value of displacement in a fixed pre-event window; $P_d^{PTW}$ is the P-peak of displacement in the corresponding P-Time-Window, which for SAVE is 1, 2, 3 seconds from P-wave arrival; $SNR_{threshold}$ is the threshold which can be set according to users' needs.

When the signal is good enough to pass the quality control expressed in the inequality (24), a second quality control is performed to select the cut off frequency for the data filtering. Since acceleration waveforms are integrated once to get velocity and twice to get displacement, signals could be affected by low frequency drift. This drift is removed with a high-pass filter.

For each PTW, SAVE calculates the ratio $P_d^{PTW}/P_v^{PTW}$, where $P_v^{PTW}$ is the P-peak of velocity in the corresponding PTW. The waveform is declared as high quality when:

$$\log\left(\frac{P_d^{PTW}}{P_v^{PTW}}\right) \leq threshold_{HIGH} \tag{25}$$

where $threshold_{HIGH}$ is pre-determined. In fact, if velocity and displacement waveforms are correctly retrieved, they are expected to follow a similar decay law hence their ratio will vary in a pre-determined range. If inequality (25) is true, the signal is high-pass filtered at cut-off frequency of 0.075 Hz.

If inequality (25) is not respected, the signal is high-pass filtered at cut-off frequency of 1 Hz and a second inequality is checked. The signal is considered as low quality if:

$$treshold_{LOW}^1 \leq \log\left(\frac{P_d^{PTW}}{P_v^{PTW}}\right) \leq threshold_{LOW}^2 \tag{26}$$

Again, $treshold_{LOW}^{1}$ and $threshold_{LOW}^{2}$ are pre-determined. Should the waveform fail the second quality control, the signal is discarded.

### 3.1.3 Parameter estimates

The expected Peak Ground Velocity ($PGV_{SAVE}^{PTW}$) is estimated by SAVE in the corresponding P-wave time window (PTW) (1, 2, 3 seconds since P-arrival) and is obtained through a log-linear regression in the form of equation (22) in the paragraph 2.2.2 where the P-peak of displacement $P_d$ is updated at each P-time window. The coefficients in equation (22) are empirically calibrated for high- or low- quality data in each of the available PTW. The empirical regressions PGV vs Pd of Caruso et al. (2017) were calibrated on a dataset of Italian and Japanese earthquakes.

The main output of SAVE is the shaking intensity expected to the site that is evaluated through scaling laws that link the measured PGV to MMI such as:

$$\mathrm{MMI} = \mathrm{A} + \mathrm{B} \cdot \log\left(PGV_{SAVE}^{PTW}\right) \tag{27}$$

Where A and B are regional coefficients (for Italy A=5.11 and B=2.35 from Faenza and Michelini (2010))

Moreover, SAVE introduces a novelty in the final parameter estimates. Generally, for an on-site system, the expected shaking intensity is the only output which is required to eventually issue an alert (paragraph 2.2.2). Since SAVE has two quality controls, as described in the paragraph above, when the data is particularly good (that is high-quality waveform) SAVE can also provide a rough estimate of the event magnitude and the source-to-receiver distance. The magnitude estimate is obtained by measuring the characteristic period $\tau_c$ in each available PTW. The $\tau_c$ is converted to expected magnitude according to:

$$M = C^{PTW} + D^{PTW} \cdot \log\left(\tau_c^{PTW}\right) \tag{28}$$

Where $C^{PTW}$ and $D^{PTW}$ are empirically calibrated in each available PTW= 1, 2, 3 seconds. Caruso et al. (2017) showed that the magnitude estimated by equation (28) is affected by a great uncertainty. For this reason, it has been chosen to provide a magnitude classification, rather than the dot magnitude value. The event is classified as:

$$\begin{cases} SMALL & (M \leq 3) \\ MEDIUM & (3 < M \leq 5) \\ MODERATE & (5 < M \leq 7) \\ LARGE & (M > 7) \end{cases}$$

The source-to-receiver distance is obtained through an empirical law that combines the P-peak of displacement $P_d$ and the characteristic period $\tau_c$ which leads to:

$$\log(R) = E^{PTW} + F^{PTW} \cdot \log(P_d^{PTW}) + G^{PTW} \cdot M_{\tau_c}^{PTW} \qquad (29)$$

The coefficient $E^{PTW}$, $F^{PTW}$ and $G^{PTW}$ are calibrated in each PTW. The mathematical details of how the equation (29) is derived are presented in the box 3.1.2.

***Box 3.1.2: Source-to-receiver distance empirical law***

Let us recall the general formulation of the GMPE:

$$logPGV = A + BM + ClogR \qquad (I)$$

Then the logarithmic distance from the earthquake source is:

$$logR = \frac{log\,(PGV)}{C} - \frac{B}{C}M - \frac{A}{C} \qquad (II)$$

In SAVE, the magnitude estimate is available from $\tau_c$ measurement, while $logPGV$ is obtained from:

$$log(PGV^{SAVE}) = a + blog(P_d) \qquad (III)$$

Putting equation (III) into (II), the logarithmic distance in SAVE can be obtained as:

$$logR^{SAVE} = \frac{a}{C} + \frac{b}{C}logP_d - \frac{B}{C}M_{\tau_c} - \frac{A}{C} \qquad (IV)$$

By imposing $\left(\frac{a-A}{C}\right) = E, \frac{b}{C} = F, -\frac{B}{C} = G$, we obtain:

$$logR^{SAVE} = E + FlogP_d + GM_{\tau_c} \qquad (V)$$

Which corresponds to the equation (14) in the text.

The uncertainty of the distance estimate by the equation (29) derives both from the errors coming from the equation (27) and the errors from the equation (28). Hence, SAVE provides a classification of source-to-receiver distance in the form of distance intervals:

$$\begin{cases} NEAR & (R \leq 50\ km) \\ INTERMEDIATE & (50\ km < R < 150\ km) \\ FAR & (R \geq 150\ km) \end{cases}$$

## 3.2 SAVE at Turkey

### 3.2.1 Introduction of SAVE test to the 2023 Turkey doublet

A devastating earthquake doublet occurred at the Eastern Anatolian Fault Zone (EAFZ) in Turkey on February 6th 2023. The first event was the Mw 7.8 earthquake that nucleated on a smaller structure called the Nurdağı-Pazarcık Fault (NPF) and then the rupture propagated toward the EAFZ where it spread bilaterally with a total rupture length of ~350 km; about 9 hours later, a second event of Mw 7.6 struck in the same region with hypocenter on the Sürgü fault (SF) spreading bilaterally with a total rupture length ~160 km (see Figure 3.2.1) (Melgar et al., 2023). Due to the significant shaking and the superimposition of the two strong earthquakes, the casualties were reported to be near the apocalypse (more than 50.000 deaths). The earthquake intensity was registered up to 10 degrees. In many cities (such as Antakya in the southeast of Turkey) numerous buildings were destroyed to the ground with surrounding areas turning into ruins.

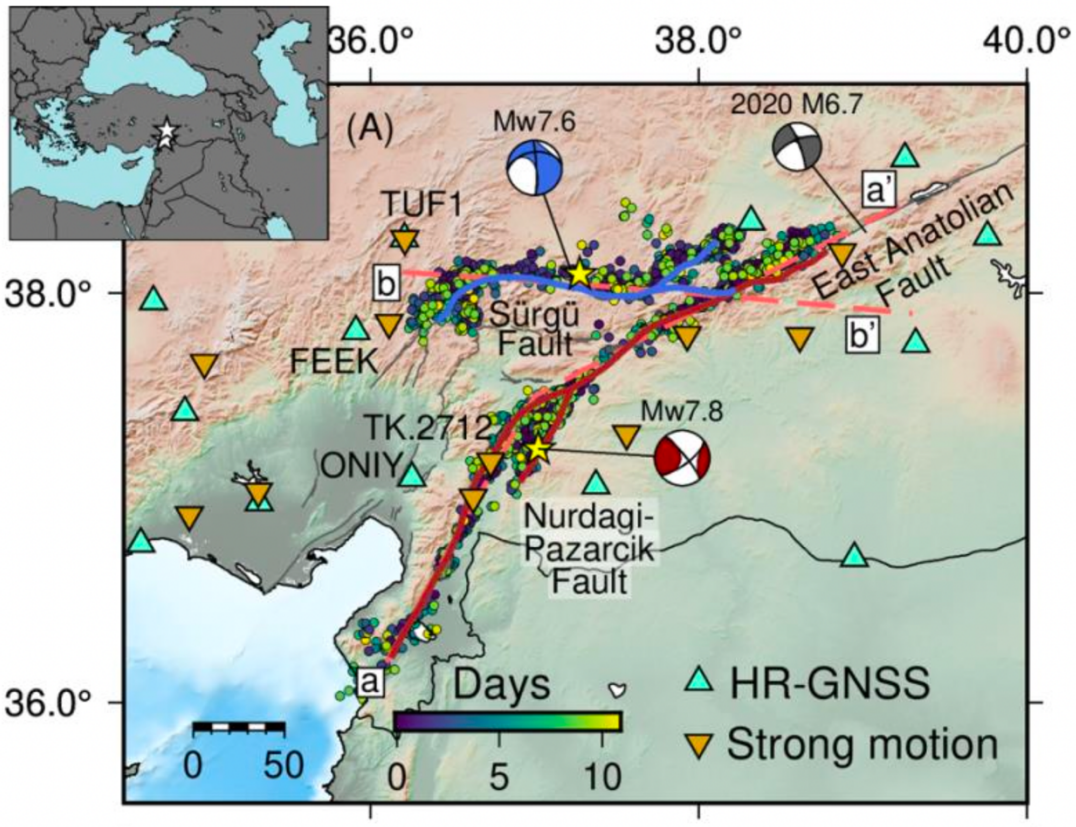


*Figure 3.2.1: Simplified map of the study region showing the focal mechanisms for both events in the earthquake doublet. Known and mapped fault surface traces are shown as dark grey lines. The East Anatolian (EAF) fault and Sürgü fault (SF) are labeled. The inferred Nurdağı-Pazarcık Fault (NPF) is labeled as well. The first 11 days of aftershocks are shown. The grey moment tensor is for the. M6.7 2020 Doğanyol-Sivrice earthquake. (from (Melgar et al., 2023))*

Turkey is one of the most seismically active regions of the world. The majority of the observed seismicity is located on the Anatolian Plate, with two main fault systems called the North Anatolian Fault Zone (NAFZ) and the East Anatolian Fault Zone (EAFZ). (Tan and Taymaz, 2006). The NAFZ was particularly active in the past three decades when a series of M+7 happened including the 1999 Kocaeli Earthquake (Mw 7.6), the 2011 Van Earthquake (Mw 7.2) and the 2020 Neon-Karlovasion Earthquake (Mw 7.0). In the same time period, the EAFZ was relatively quiescent. The strongest event registered on the EAFZ until February 2023 was the Mw 6.8 Doğanyol-Sivrice earthquake of January 2020 (Melgar et al., 2020). Many authors believed that the EAFZ would be active throughout the twenty-first century and one or more destructive earthquakes might occur ((Nalbant et al., 2002), (Taymaz et al., 2021)). Particularly, Nalbant (2002) calculated the stress evolution along the fault zone due to both seismic and tectonic loading since 1822, identifying two areas of relevant seismic risk where a large event (M~8) might have occurred. One of these two areas involved the location where the first M 7.8 earthquake of the doublet struck in February 2023.

Given the high seismic risk that characterizes Turkey, the country has invested research efforts in Earthquake Early Warning Systems. Although the city of Istanbul has an operative warning system which is based on a simple exceedance of acceleration threshold at three stations in the network, the alert distribution is still limited to just specific area and companies, such as the Istanbul Gas Distribution Company and the Marmaray Tube Tunnel (Clinton et al., 2016). In June 2021 Google's Android Earthquake Alert System was announced in Turkey. The system proposed by the Google company should provide warnings to the millions of Android's cellphone users at the occurrence of an earthquake higher than M 4.5 analyzing acceleration waveforms recorded by the built-in sensors in each cellphone. However, on February 6$^{th}$ 2023 hundreds of thousand people did not receive any warning (drop, cover and hold on) when the M 7.8 earthquake struck, raising questions about the reliability of such system (Clayton et al., 2023). In a retrospective analysis, Rea (2024) proved that an impact based EEWS would have issued an alert after 10-20 seconds from origin time with a threshold intensity MMI=IV, resulting in 95% of successful warnings with available lead-times up to 60 seconds (Rea et al., 2024). Within this framework, we tested SAVE on the earthquakes doublet in order to explore the feasibility of an on-site EEWS in the region.

***Box 3.3.1: The Source Time function of the Mw 7.8 earthquake and the Mw 7.6 earthquake (Melgar et al. 2023)***

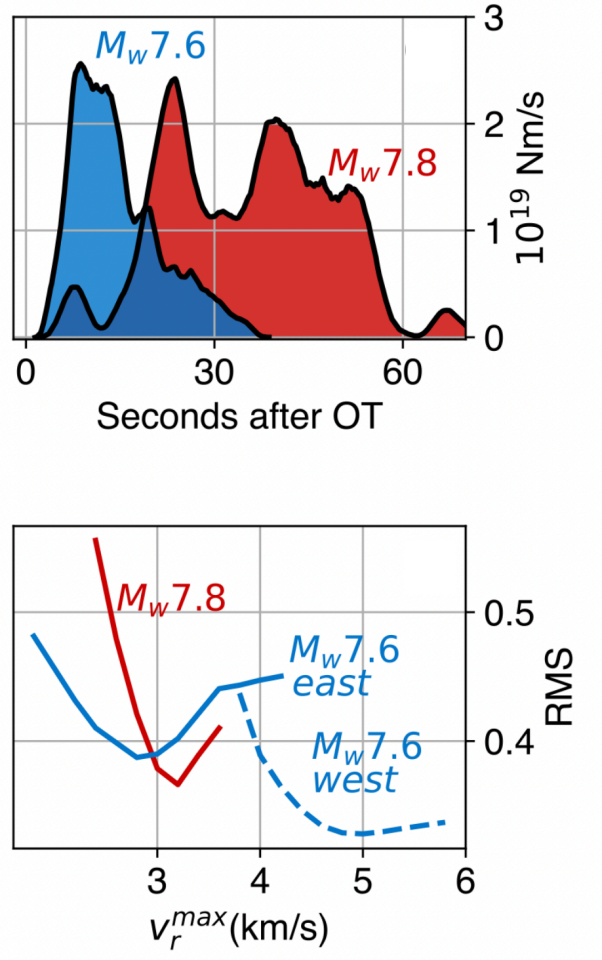


*Figure 3.2.2: Top Panel: Source time functions for both ruptures. Bottom panel: RMS misfit as a function of maximum rupture speed $v_r^{max}$ allowed in the inversion for both events. For the Mw 7.6 authors distinguished between misfit for stations east or west of the hypocenter. Best fitting values are 3.2 km/s for the Mw 7.8 and 2.8 and 5.0 km/s for the Mw 7.6. (from (Melgar et al., 2023))*

In Figure 3.2.2 top panel the source time function of the Mw 7.8 (in red) and the Mw 7.6 (in blue) are shown. The STFs were evaluated by Melgar et al. (2023) following a linearized multi time-window kinematic inversion. In bottom panel, results concerning the rupture velocity are shown for both events. The RMS misfit from source inversion showed that the Mw 7.8 earthquake (in red) was characterized by an overall average velocity of 3.2 km/s; the Mw 7.6 showed a super-shear velocity which involved the west of the bilateral rupture and a sub-shear velocity which involved the east (Melgar et al., 2023). It is worth to mention that when SAVE test was performed, the Moment Rates of Melgar et al. (2023) were the first proposed source time functions. However, later in literature other Moment Rate functions have been developed and published.

### 3.2.2 Off-line test on the Mw 7.8 earthquake of 6 February 2023

In order to perform the off-line test for the Mw 7.8 earthquake (first event of the doublet) we acquired data from the Disaster and Emergency Management Presidency of Türkiye (AFAD). The dataset consisted of three-component acceleration waveforms of the strong motion network, recorded at stations located few kilometers up to about 600 kilometers from the event epicenter.

Concerning the tuning phase of SAVE, we set the thresholds for data quality control used in Caruso et al (2017) and we also used the same logPGV vs logPd empirical scaling laws to evaluate the predicted PGV at the site. The expected shaking intensity is obtained through Bilal and Askan (2014) scaling law. The Bilal and Askan (2014) MMI versus logPGV relation was obtained from data of 14 moderate-to-large earthquakes that occurred in Turkey between 1976 and 2011, including the Mw 7.2 earthquake which was the biggest event available in the catalog at the time of the paper publication. The MMI versus PGV law was tailored on Turkey seismicity because it was observed that existing MMI vs PGV laws for other regions in the world (e.g. (Worden et al., 2012), (Faenza and Michelini, 2010)) did not fit Turkish data, resulting in either under- or overestimations (Bilal and Askan, 2014).

In panel A of Figure 3.2.3, we show the results of the predicted PGV (and MMI) versus the observed PGV (and MMI) after 3 seconds since the P-wave arrival was automatically picked on the trace. The observed PGV is obtained from the horizontal components of velocity waveforms. Stations within 100 km of epicentral distance present the highest value of PGV (MMI), while stations further than 500 km show very low PGV amplitudes (MMI). However, we notice there is an overall underestimation of the expected PGV (as shown in histogram of panel B of Figure 3.2.3). The underestimation we observe might be explained in terms of rupture complexity. In Figure 3.2.2 of box 3.3.1, we reported the source time functions of both Turkish events obtained by Melgar (2023) through kinematic inversion. The source time function of the Mw 7.8 is represented with red color. In principle, we should expect an almost triangular-scalene-shaped function, from which we could infer the total energy release (total seismic moment) from the area underneath (Aki and Richards, 2009). However, for the Mw 7.8 earthquake the source time function is too complex to be represented by such a model. Indeed, there is a first energy release (the small triangular-shaped impulse preceding the biggest one in Figure 3.2.2) that is due

to the fact that the rupture of the Mw 7.8 first nucleated on a small fault segment on the west of the EAFZ, the NFP (Melgar et al., 2023).

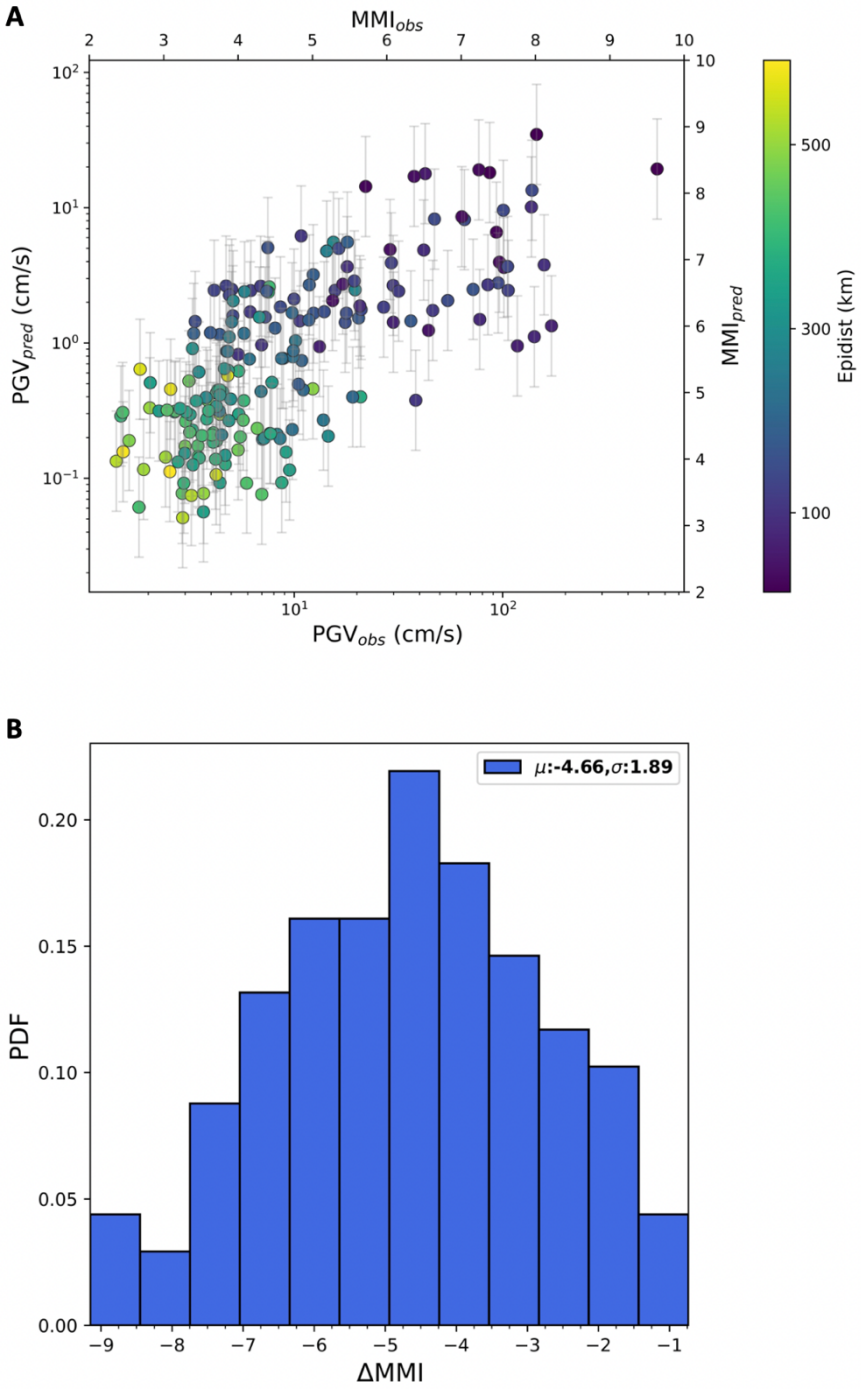


*Figure 3.2.3: Panel A shows $PGV_{pred}$ versus $PGV_{obs}$ at each station using 3 seconds PTW. Markercolor follows epicentral distance. Secondary axis indicates $MMI_{pred}$ and $MMI_{obs}$ obtained from Bilal 2014 scaling law. Panel B shows the prediction error ($MMI_{pred}$-$MMI_{obs}$) as probability density function. The mean value and the standard deviation of the distribution are represented in top right corner.*

Performing a raw evaluation of the seismic moment of the first impulse of the Mw 7.8, we obtained that the energy release in the first ten seconds since rupture beginning

corresponds to an event of M~6. To obtain this estimate we roughly evaluate the seismic moment from the area underneath the first ten seconds of the source time function of Melgar et al. (2023) and used Kanamori (1977) (Kanamori, 1977) law for moment magnitude evaluation.

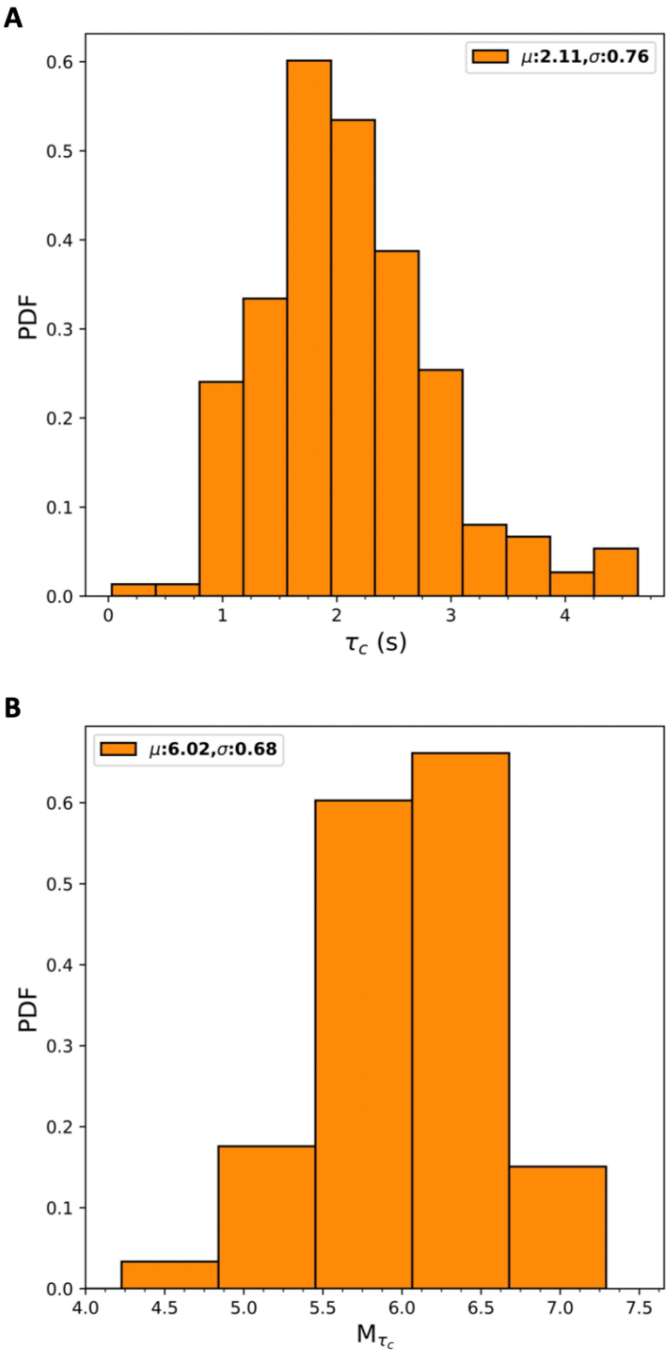


*Figure 3.2.4: Panel A shows the distribution of $\tau_c$values using 3 seconds PTW as probability density function. The mean and the standard deviation of the distribution are represented in top right corner. Panel B shows the distribution of the moment magnitude using 3 seconds PTW obtained using the Caruso et al 2017 Mw versus log($\tau_c$) empirical law. The mean and the standard deviation of the distribution is reported in top left corner.*

SAVE empirical relationships relate on the $P_d$ parameter to get PGV estimates. This means that in the first three seconds since the P-wave arrival on the records, $P_d$ could effectively be mapping the displacement associated with an event of Mw~6, resulting in the underestimation we see. This effect is even more evident when we look at the average $\tau_c$ and consequently, at the average point magnitude estimate provided by the system in 3 seconds (see Figure 3.2.4).

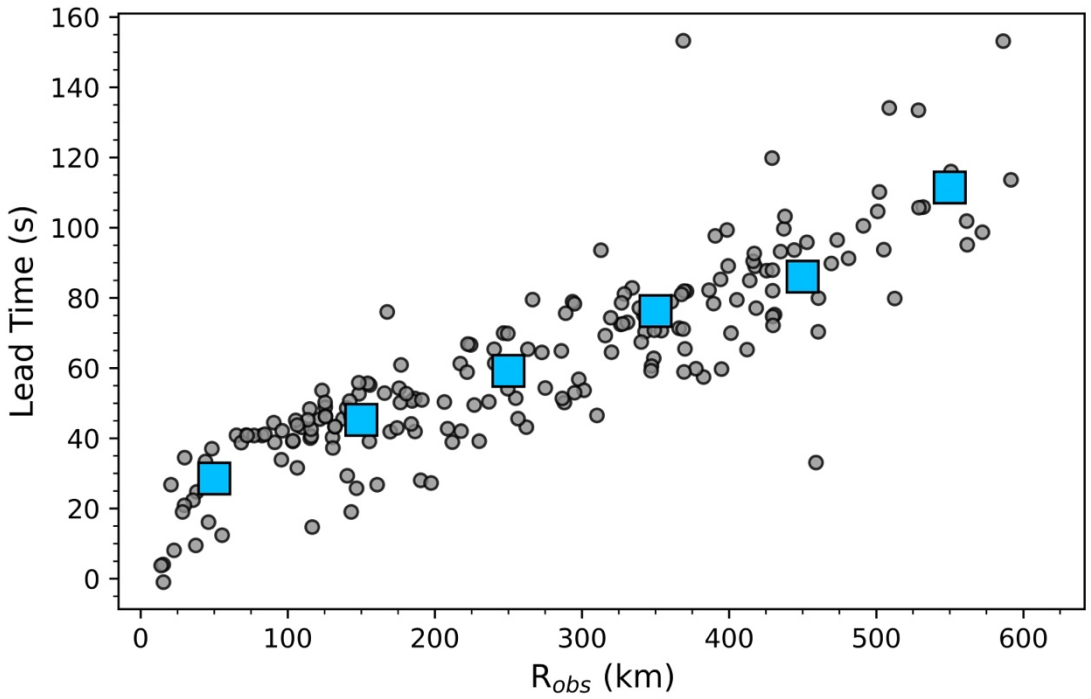


*Figure 3.2.5: Lead time plot of the off-line test on the Mw 7.8 Turkish earthquake. The Lead Time is obtained as the difference between the PGV arrival and the P-wave arrival at the station minus 1 second required by the system to give a first MMI estimate. Grey points are single station lead times. Blue squares are averaged lead times in an observed epicentral distance bin (bin width = 100 km).*

In Figure 3.2.5 we show the lead time at the available stations. The lead time in SAVE is evaluated as the difference between the PGV arrival at the site and the P-time window required to get the MMI estimation, as:

$$Lead\ Time_{SAVE} = \mathrm{T(PGV)} - (T_P + PTW) \qquad (30)$$

In case of a large event like the Mw 7.8 Turkish earthquake, the PGV might be related mostly to surface waves which reach the sites of interest very late with respect to body waves. This could explain the higher lead times values that we observe in Figure 3.2.5. Although with an underestimation of the impact, we notice that on average, SAVE would have provided about 30 seconds of available lead time for sites located within 100 km

from the event epicenter and more than 100 seconds for sites located within 500 km from the event epicenter (the cyan squares in Figure 3.2.5).

The off-line test we performed on the Mw 7.8 Turkish earthquake showed that SAVE could be integrated in an EEW system providing first simple alerts in very short time windows. However, in cases of events with M 6+ the P-wave window must be expanded. In a recent ongoing work (Ding et al., 2024) we evaluated that at last 10 seconds of the P-wave time window are needed to obtain reliable PGV predictions for the Turkey-Syria mainshock. In this case a proper strategy must be designed to automatically identify the optimal time window to be used for alert.

SAVE is not able to properly catch the rupture complexity, however, the test demonstrates that it would have sent valid information about the incoming earthquake to a wide area which was effectively affected by severe damages.

### 3.2.3 Off-line test on the Mw 7.6 earthquake of 6 February 2023

The Mw 7.6 earthquake (second event of the doublet) struck along the Sürgü fault about 9 hours later since the origin time of the first Mw 7.8 earthquake. We performed the off-line test of SAVE on the acceleration waveforms from AFAD database. As for the test in paragraph 3.2.2, for the tuning phase of the system we selected the same threshold values used in Caruso et al. (2017) for the data quality control and the Bilal 2014 MMI versus PGV scaling law to get the predicted MMI from the predicted PGV.

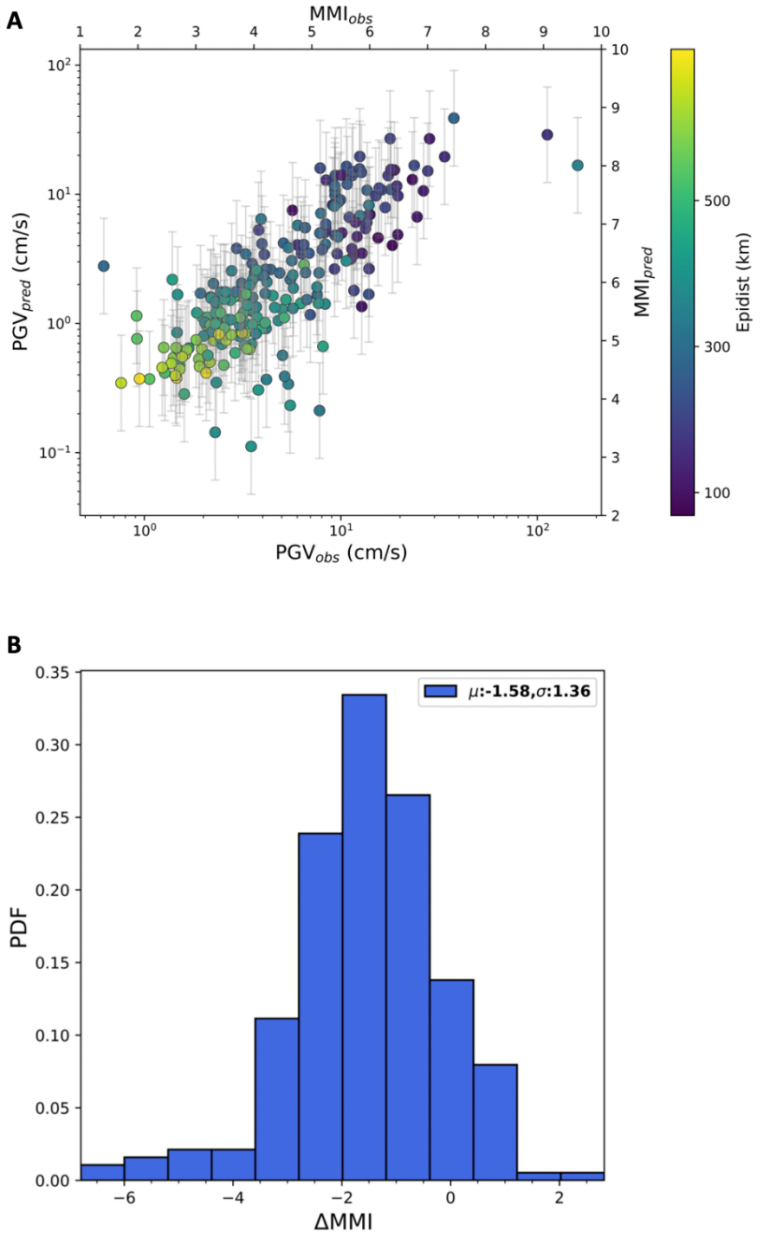


*Figure 3.2.6:Panel A shows PGV$_{pred}$ versus PGV$_{obs}$ at each station using 3 seconds PTW. Markercolor follows epicentral distance. Secondary axis indicates MMI$_{pred}$ and MMI$_{obs}$ obtained from Bilal and Askan (2014) scaling law. Panel B shows the prediction error (MMI$_{pred}$-MMI$_{obs}$) as probability density function. The mean value and the standard deviation of the distribution are represented in top right corner.*

In Figure 3.2.6 we represent the result of the predicted PGV (MMI) versus the observed PGV (MMI). The general trend shows an underestimation of expected shaking intensity at the site (see panel B of Figure 3.2.6) after 3 seconds since P-wave arrival. However, the underestimation we observe for the off-line test of the Mw 7.6 earthquake is less severe than the underestimation we observe for the Mw 7.8 earthquake.

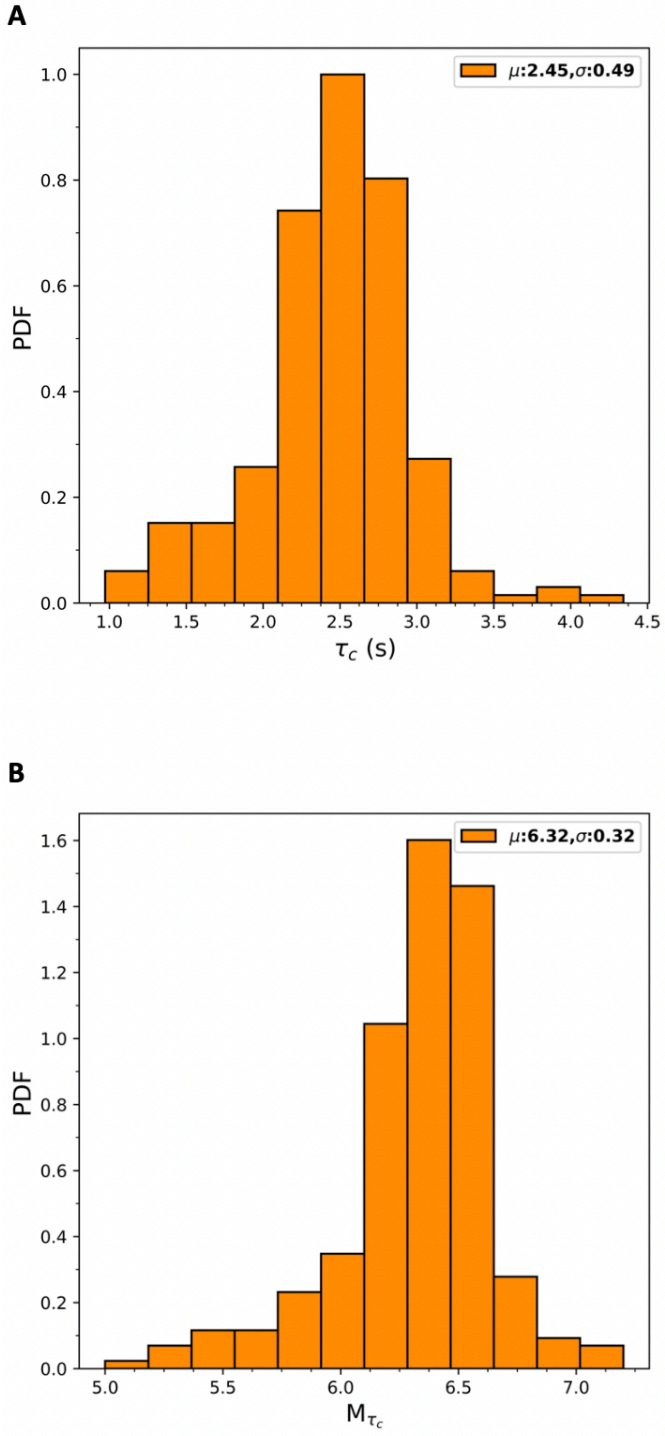


*Figure 3.2.7: Panel A shows the distribution of $\tau_c$ values using 3 seconds PTW as probability density function. The mean and the standard deviation of the distribution are represented in top right corner. Panel B shows the distribution of the moment magnitude using 3 seconds PTW obtained using the Caruso et al 2017 Mw versus log($\tau_c$) empirical law. The mean and the standard deviation of the distribution is reported in top left corner.*

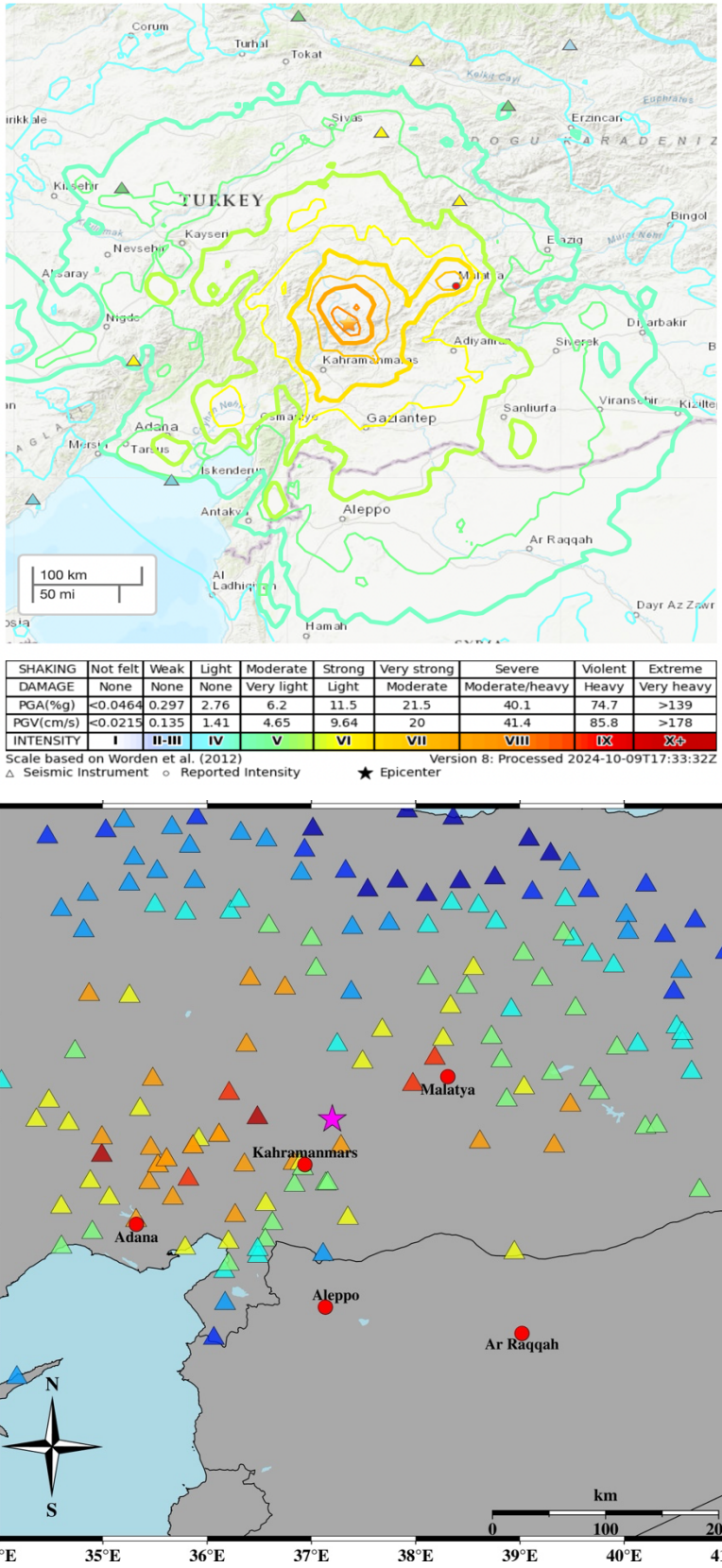


*Figure 3.2.8: top panel: Intensity map for Mw 7.6 earthquake provided by USGS. Bottom panel: predicted intensity map obtained through SAVE using 3 seconds of signal after P-wave onset at each station (colored triangles). Colorbar follows intensity scale.*

The fact that the underestimation effect is less heavy for the off-line test of the Mw 7.6 is even visible in Figure 3.2.7, showing the results of the point magnitude estimation in 3 seconds PTW from $\tau_c$ measurements. On average, the system classification of the event magnitude was about Mw 6.4, placing the earthquake in the class of moderate events. For the Mw 7.6 earthquake, the source time function retrieved by Melgar (2023) with kinematic inversions is triangular-shaped (see Figure 3.2.2). The complexity of the rupture depends mostly on the different values retrieved for the rupture velocity (super-shear towards the west and sub-shear towards the east in panel B of Figure 3.2.2). The underestimation in the prediction of both expected shaking intensity and the moment magnitude might be related to a saturation in the last available P-Time Window used for parameters estimation. In order to resolve the underestimation, we could extend the available time window to get more accurate parameter estimations, although other potential bias might enter in the final output evaluation such as the inclusion of S-waves in the time window for the sites very close to the event location. Indeed, the 3 seconds PTW corresponds to the source duration of an event of Mw~6, which is what the system is retrieving by using Pd and $\tau_c$ evaluated in the last PTW used by SAVE.

Interestingly, in bottom panel of Figure 3.2.8 we plot the expected shaking intensity at each station after 3 seconds since P-wave arrival and we notice that from the values obtained by SAVE there is an elongation of the highest MMI first towards the west (with respect to the event location) where the rupture propagated faster (Melgar et al., 2023). Moreover, other observations arise from the comparison of SAVE predicted MMI map with the MMI map provided by USGS shakemap service: (1) at the closest city to event epicenter, Kahramanmars, the system correctly predicts severe shaking; (2) the contour of severe shaking of USGS map (top panel of Figure 3.2.8) shows a lobe which includes the city of Malatya and SAVE also obtains the same result (bottom panel of Figure 3.2.8); (3) SAVE predicted intensity at the site of Adana is slightly overestimated with respect to USGS result. Some of the differences in MMI values between the two representations might derive from the fact that USGS shakemap tool uses Worden (2012) MMI vs PGV scaling law to provide intensity estimates, while for this test of SAVE we used Bilal and Askan (2014) MMI vs PGV scaling law which is tailored on Turkey region. It is worth to notice (from Figure 3.2.8) that in just three seconds from the first P-wave pick, the system would have issued alerts for an event of MMI > 4 at stations falling in a circular ring of 200 km from the event location. In the framework of EEW applications, this result is promising because SAVE could be coupled with existing regional systems in the region.

A fast alert providing expected shaking intensity could be sent at those areas where a strong shaking is expected. Until now, EEW systems in Turkey are issuing alerts just around Istanbul area (Clinton et al., 2016).

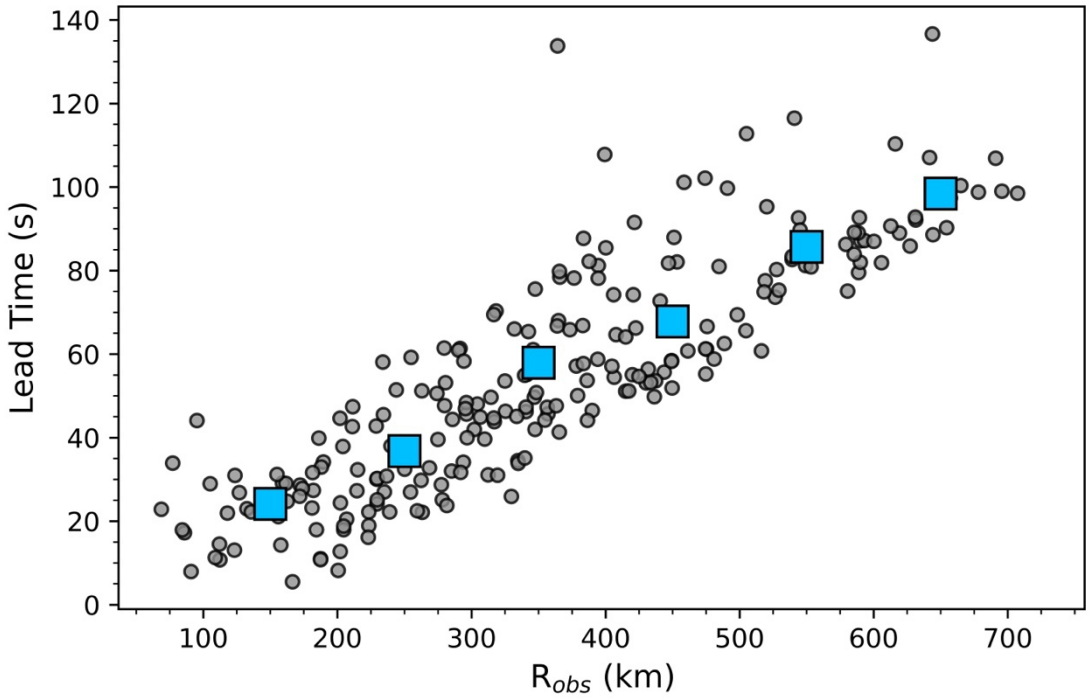


*Figure 3.2.9: Lead time plot of the off-line test on the Mw 7.6 Turkish earthquake. The Lead Time is obtained as the difference between the PGV arrival and the P-wave arrival at the station minus 1 second required by the system to give a first MMI estimate. Grey points are single station lead times. Blue squares are averaged lead times in an observed epicentral distance bin (bin width = 100 km).*

The lead times for the off-line test on the Mw 7.6 event are shown in Figure 3.2.9. The average values are compatible with the off-line test of paragraph 3.2.2 performed on the Mw 7.8 earthquake. Here SAVE would have provided about 30 seconds of available time before the PGV arrival at sites located within 150 km from the event epicenter and almost 100 seconds before the PGV arrival at station located at 500 km from the event epicenter.

## 3.3 SAVE at California

### 3.3.1 Introduction to SAVE test to California region

In the western United States (Washington, Oregon and California), the ShakeAlert system is fully operational (Kohler et al., 2020), providing warning to users about shaking ahead of time when an earthquake occurs. As a regional EEW system, ShakeAlert is designed to detect earthquake arrivals at seismic stations ((Meier et al., 2019), (Chung et al., 2019)) and to characterize earthquake source parameters and the expected impact through dedicated algorithms such as EPIC ((Chung et al., 2019), (Kohler et al., 2020)) and FinDer (Böse et al., 2018). Peak ground motions are estimated using ground-motion prediction equations (GMPEs) (e.g. (Boore and Atkinson, 2008)). Modified Mercalli Intensity (MMI) is finally computed through regional equations that convert Peak Ground Velocity and Peak Ground Acceleration into MMI (Worden et al., 2012). The free earthquake smartphone app MyShake has also been delivering ShakeAlert-powered alerts in western U.S. since its public launch in 2019. Started as a citizen science project by the University of California at Berkeley in 2016, MyShake uses a neural network machine learning algorithm which is trained to distinguish between human activity and earthquake signals analyzing the waveforms recorded by the accelerometer built into each smartphone (Kong et al., 2016). Recently, Patel and Allen (Patel and Allen, 2022) have shown that MyShake waveforms can enhance resolution and shaking variability during earthquakes. Indeed, when accounting for proper site effect corrections, it is possible to build GMPEs (Marcou et al., 2024).

The implementation of a system that can rely on single waveforms could help provide additional seconds of warning time in some circumstances. This is because network-based earthquake early warning systems such as the one in California require a few seconds to evaluate source characteristics. As a consequence, there are regions that might not receive an alert, especially at high intensity shaking locations close to the epicenter (Meier et al., 2020).

In this paragraph we show the results of the application of SAVE in California. California is characterized by onshore, shallow crustal earthquakes of small-to-moderate magnitude and has experienced big events not so far in the past (such as 1989 M 6.9 Loma Prieta earthquake). Moreover, a high level of off-shore seismicity occurs at the Mendocino triple junction, that includes thrust, normal, and strike-slip earthquakes.

In order to compare SAVE with existing regional system ShakeAlert, we assessed SAVE performance in terms of:

Successful Alert (SA): $MMI_{pred} > MMI_{threshold}$ & $MMI_{obs} > MMI_{threshold}$

Successful No Alert (SNA): $MMI_{pred} \leq MMI_{threshold}$ & $MMI_{obs} \leq MMI_{threshold}$

False Alert (FA): $MMI_{pred} \geq MMI_{threshold}$ & $MMI_{obs} < MMI_{threshold}$

Missed Alert (MA): $MMI_{pred} < MMI_{threshold}$ & $MMI_{obs} \geq MMI_{threshold}$

Where $MMI_{pred}$ is the predicted intensity by SAVE, $MMI_{obs}$ is the observed intensity at the site and $MMI_{threshold}$ is a user defined intensity threshold. The matrix scheme above is then used to quantify the system performance in terms of precision and recall.

The "Precision" is defined as (Meier et al., 2020):

$$Precision = \frac{SA}{SA + FA} \tag{31}$$

Whereas the "Recall" is defined as:

$$Recall = \frac{SA}{SA + MA} \tag{32}$$

The Precision obtained from equation (31) is informative about the number of correct alerts that the system sent. The Recall obtained from equation (32) is informative about the number of alerts that the system should have been sent. These two metrics are standard metrics used in Machine Learning algorithms to assess the goodness of fit. Since the output is a category classification, they can be easily adapted to evaluate the performance of a threshold base system.

### 3.3.2 Test on event data

We run SAVE retrospectively on 113 earthquakes in California (Figure 3.3.1), spanning a magnitude range between 4 and 7 and shallow depths down to 35 km. The stations we used are included in the Northern and Southern California networks with seismic records

having epicentral distances between a few kilometers to 1000 km from the event locations. From Figure 3.3.2 to Figure 3.3.4 we compare the predicted PGV with the observed PGV in the three second P-time window for records having observed PGV higher than 0.1 cm/s which corresponds to the intensity level of MMI=2 (weak shaking)(Worden et al., 2012). Predicted PGV values are obtained using empirical scaling laws by Caruso (Caruso et al., 2017).

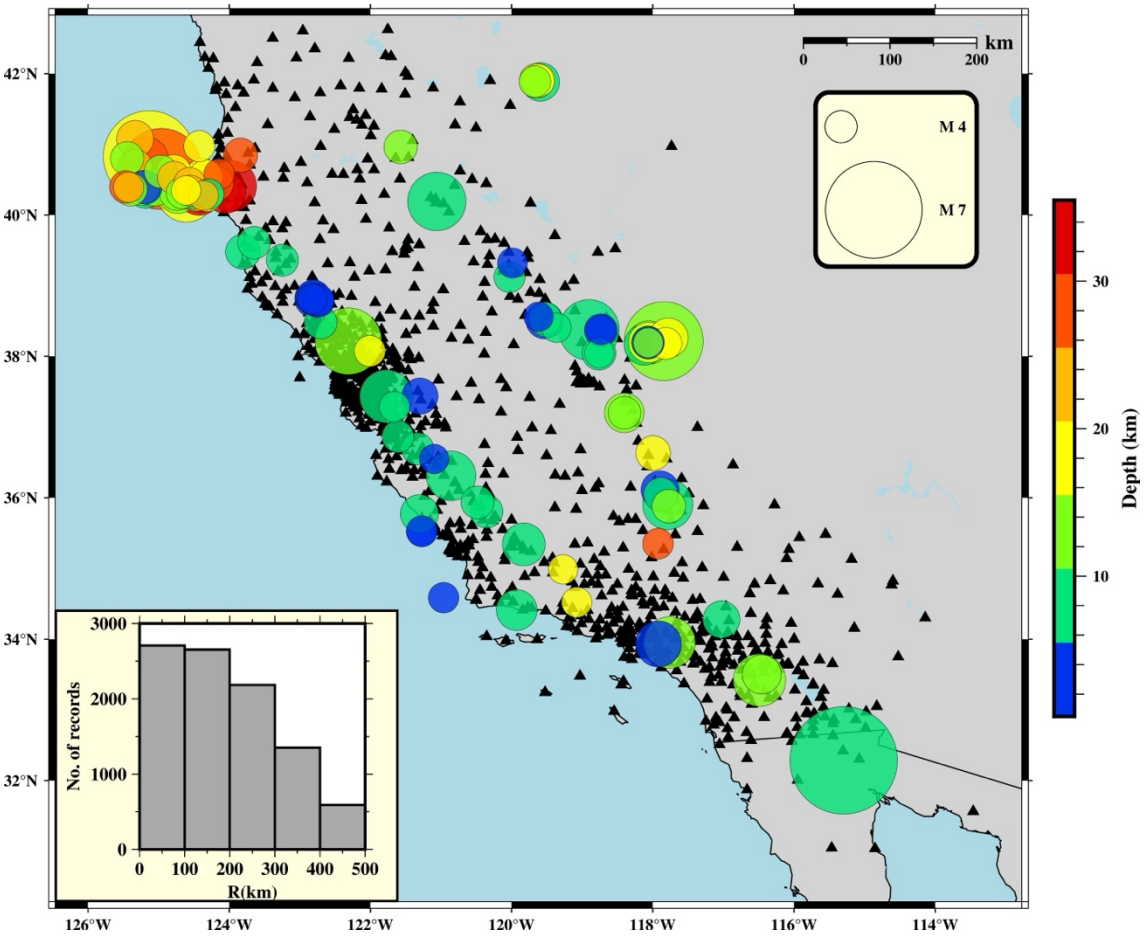


*Figure 3.3.1: Map of events. Circles represent event locations. Marker size indicates event magnitude; the color indicates event depth. Black triangles represent seismic stations used in this study. The histogram in bottom left corner shows the distribution of seismic records per distance from event epicenter.*

The underestimation of predicted PGV for events with magnitude between 5.5 and 6.5 is overcome when going from the 1 and 2 second window (as it is shown in red/magenta points of Figure 3.3.2 and Figure 3.3.3) to the 3 second window (red/magenta points of Figure 3.3.4). For events with magnitude higher than 6.5, PGV is still underestimated. This result is mostly due to the fact that the longest P-time window used in SAVE for PGV estimations (3 seconds) is still shorter than the average source duration for events with a magnitude greater than 6.5. The lead time is calculated as the difference between observed PGV time and one second PTW required to get first estimates. On average we

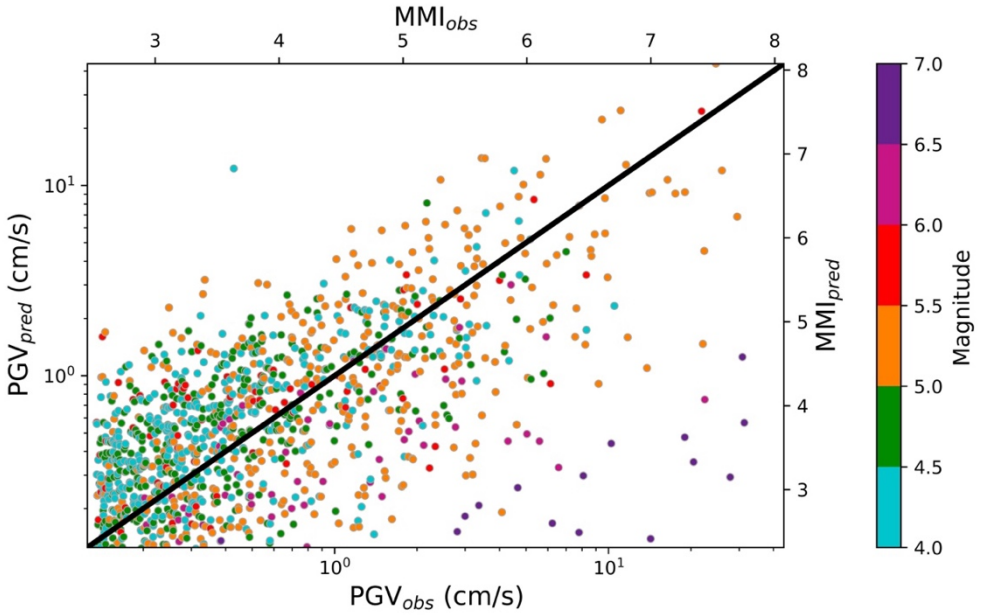


*Figure 3.3.2: Predicted PGV versus observed PGV in 1 second PTW. Each point represents a measure from a single seismic record. Markers are colored according to event magnitude. Secondary x and y axis show the observed and predicted shaking intensity respectively (MMI obtained from (Worden et al., 2012) scaling law). Black solid line is the one-to-one PGV relation.*

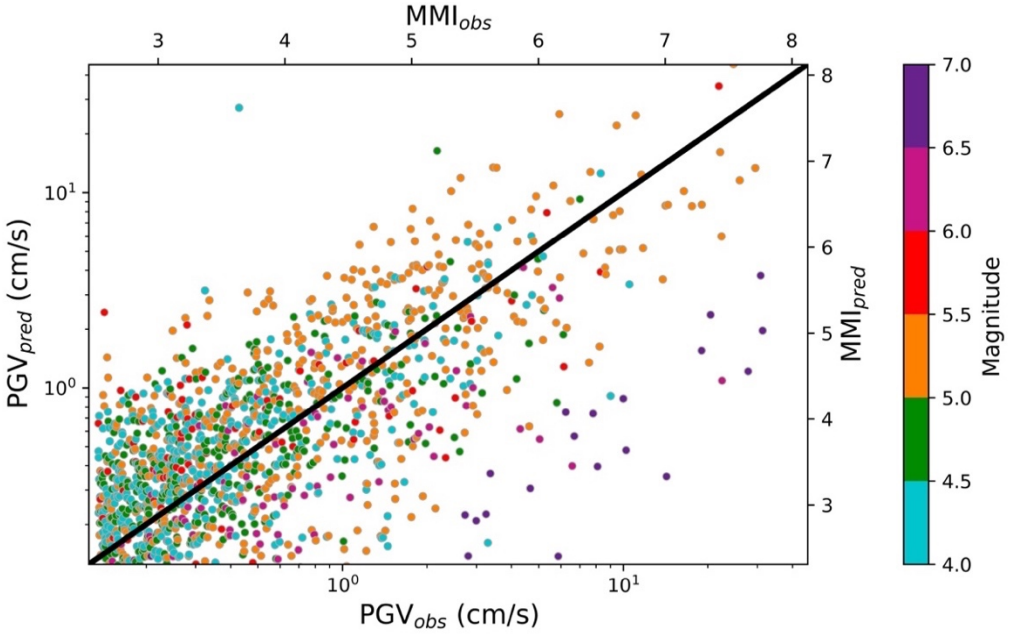


*Figure 3.3.3: Predicted PGV versus observed PGV in 2 seconds PTW. Each point represents a measure from a single seismic record. Markers are colored according to event magnitude. Secondary x and y axis show the observed and predicted shaking intensity respectively (MMI obtained from (Worden et al., 2012) scaling law). Black solid line is the one-to-one PGV relation.*

found values of 8-10 seconds at 50 km, 12-15 seconds at 100 km and 20-22 seconds at 150 km (Figure 3.3.5). The prediction error on MMI is well distributed around zero value at all observed distance ranges (Figure 3.3.6). System performance using 3 second PTW is shown in Figure 3.3.7. The system precision goes from about 75% at lower intensity

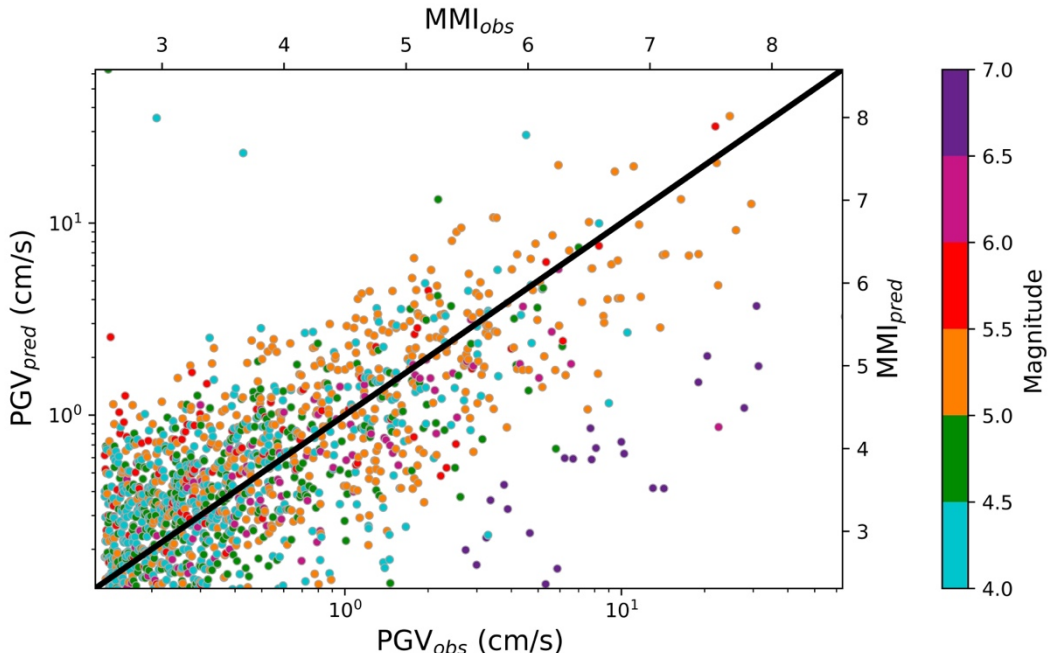


*Figure 3.3.4 Predicted PGV versus observed PGV in 3 seconds PTW. Each point represents a measure from a single seismic record. Markers are colored according to event magnitude. Secondary x and y axis show the observed and predicted shaking intensity respectively (MMI obtained from (Worden et al., 2012) scaling law). Black solid line is the one-to-one PGV relation.*

thresholds to about 50% at higher intensity thresholds, whereas the recall value decreases from 80% at lower intensity thresholds to about 25% at higher intensities.

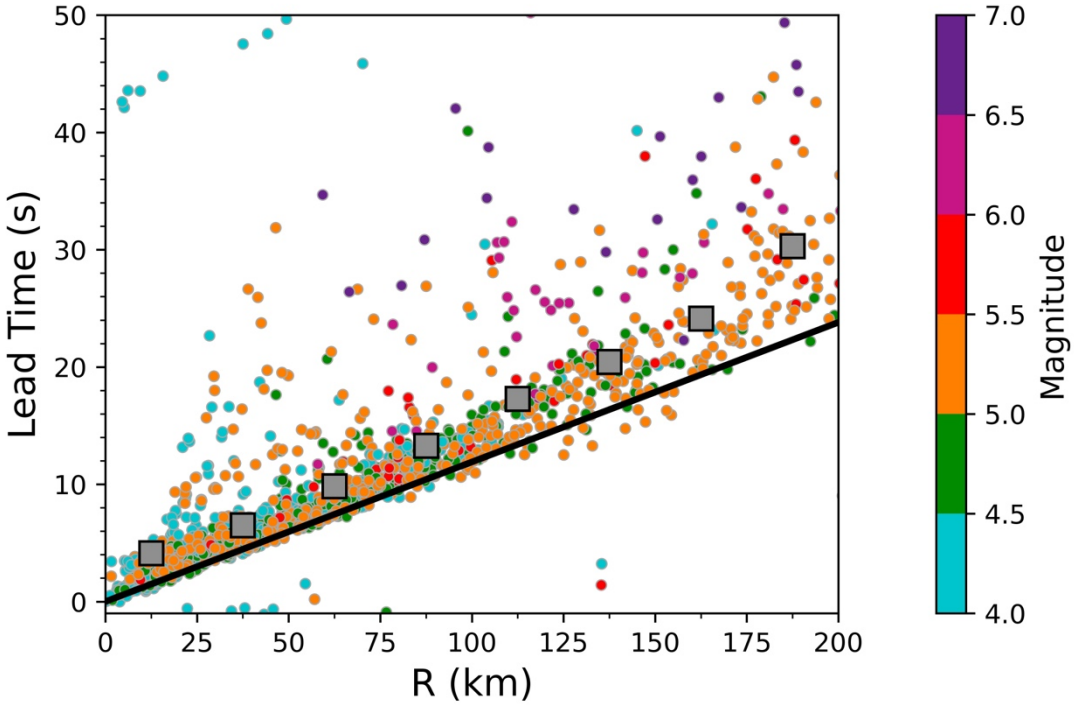


*Figure 3.3.5: Lead Time plot. The figure shows the lead time versus epicentral distance. Lead time is obtained as the difference between PGV time and the end of the 1 second PTW. Circles are single record lead times, colored by event magnitude. Darkgrey squares are averaged values of lead time in binned distance (bin width = 25 km). Black solid line is theoretical S-wave arrival. Theoretical S-wave arrival represents the minimum lead time since the PGV can be produced by later arrivals. S-wave speed is computed as 60% of P-wave speed which is fixed at 6 km/s.*

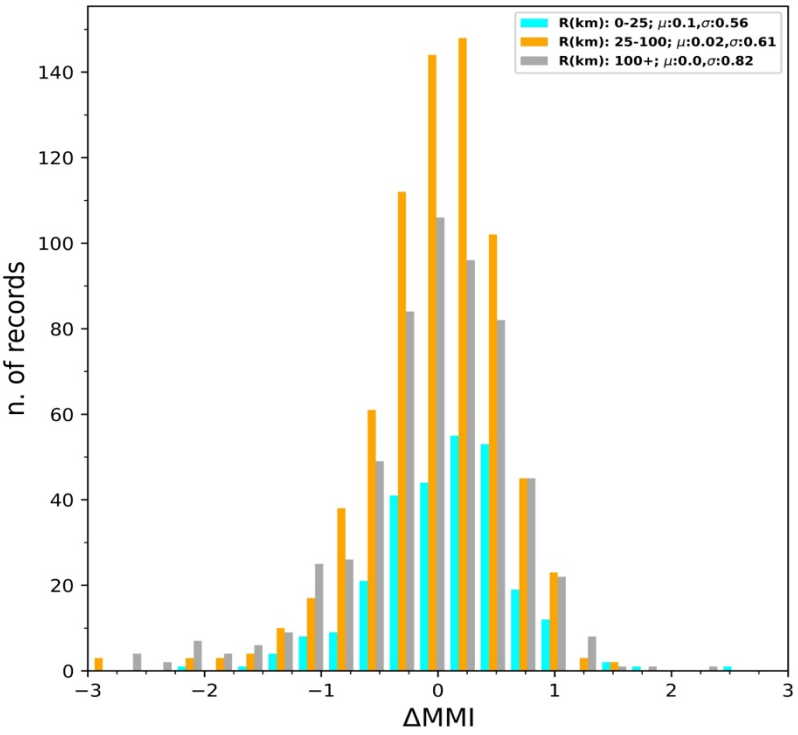


*Figure 3.3.6: Prediction error distribution using 3 second PTW. The figure shows the distribution of prediction error on shaking intensity for different ranges of distance to event epicenter: 0-25 km (cyan bars), 25-100 km (orange bars), 100 km and higher (grey bars). Mean and standard deviation of each distribution are shown in top right corner.*

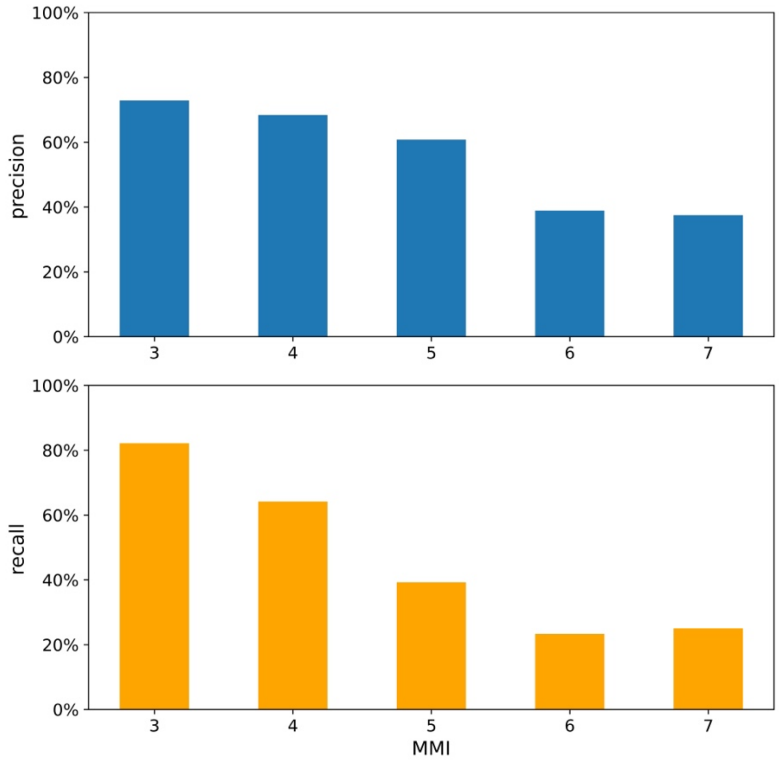


*Figure 3.3.7: Precision and recall bar plot for event dataset in 3 seconds PTW. Precision (top panel) and recall (bottom panel) variation relative to different MMI threshold values.*

The empirical scaling relationship between predicted PGV and Pd for the original SAVE algorithm (Caruso et al., 2017) requires no recalibration when tested with event data in California. That might be explained in terms of the magnitude range of the events. The Caruso (2017) empirical PGV vs Pd laws were calibrated on Italian and Japanese events spanning the same magnitude range as used for our test (M 4-7 in Figure 3.3.1). The histogram tails we observe in Figure 3.3.6 for the event data test are mostly due to (automatic) picking errors. In particular, many of the underestimation cases are due to (1) the presence of a smaller event that is picked head of the main event, or (2) an early P-pick declaration due to noise. The overestimation comes mostly from the inclusion of the S-waves in the PTW or is due to a bad phase identification (i.e picking glitches or S-waves). In future applications we can be more selective on SNR and time window thresholds which control FP used in SAVE. Moreover, automatic pickers based on Machine Learning algorithms have been recently developed and trained for Northern California (Zhu and Beroza, 2018) (Meier et al., 2019) and could replace current picker in SAVE. Usually, these techniques work well with short time window snippets of the waveform (1-3 sec), but that might also mean losing seconds of warning time as the algorithm waits for picking confirmation.

### 3.3.3 Test on continuous waveforms

We additionally tested SAVE on continuous waveforms, running the algorithm on three different networks in Northern California. We analyzed waveforms of the strong motion seismic stations of the Berkeley Digital Seismic Network (BK), the USGS Northern California Seismic Network (NC) and the USGS National Strong-Motion Project (NP). (Figure 3.3.8). We present the results of the analysis for the first two months of 2022, the last ten days of October 2022, during which the M 5.1 Alum Rock earthquake struck, and the last ten days of December 2022, during which the M 6.4 Ferndale earthquake struck. In Figure 3.3.9 we summarize the system performance. We notice there is a scatter in the estimation of MMI (Table 3-1). One reason of this result may lie in the fact that only few moderate earthquakes (M 5.1 Alum Rock and M 6.4 Ferndale) struck in the selected window for the analysis. The Caruso et al. (2017) empirical PGV vs Pd law was not calibrated to get estimates from waveforms related to smaller earthquakes (having smaller values of P-peak of displacement). This effect is quite evident in first column and first

row of Figure 3.3.9, where most of the scatter in MMI for BK network is coming from the points at lower values of PGV (MMI).

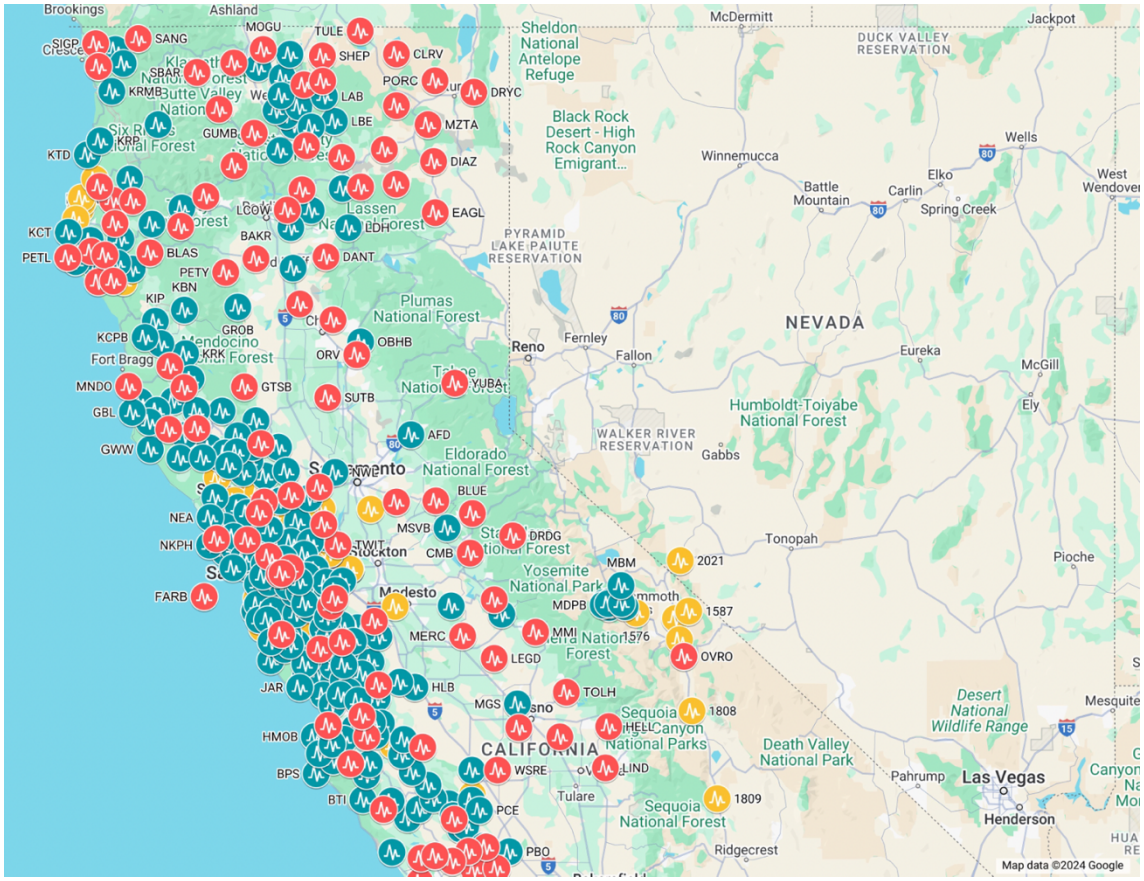


*Figure 3.3.8: Map of the stations used for the continuous waveforms test. Red points are BK stations; blue points are NC stations; yellow points are NP stations.*

The calibration of a regional PGV vs Pd empirical law partially resolves the MMI scatter, as it is shown in the histogram of the second row of Figure 3.3.9 and in Table 3-1. The Californian-tailored law of PGV vs Pd allows us to rule out any possible effect in MMI estimation that may arise from regional differences such as magnitude range, depth range and tectonic settings of the earthquakes. This means that the scatter we still observe in the prediction error of MMI may depend on the characteristic noise level for each network (the case of NP network is particularly evident in Figure 3.3.9). Hence, we calibrate a network based PGV vs Pd empirical law which completely overcomes the scatter, as it is shown in the histogram of last row of Figure 3.3.9 and more quantitatively in the reduction of the standard deviations $\sigma_{\Delta MMI}$ presented in Table 3-1 for each network with respect to the applied PGV vs Pd law.

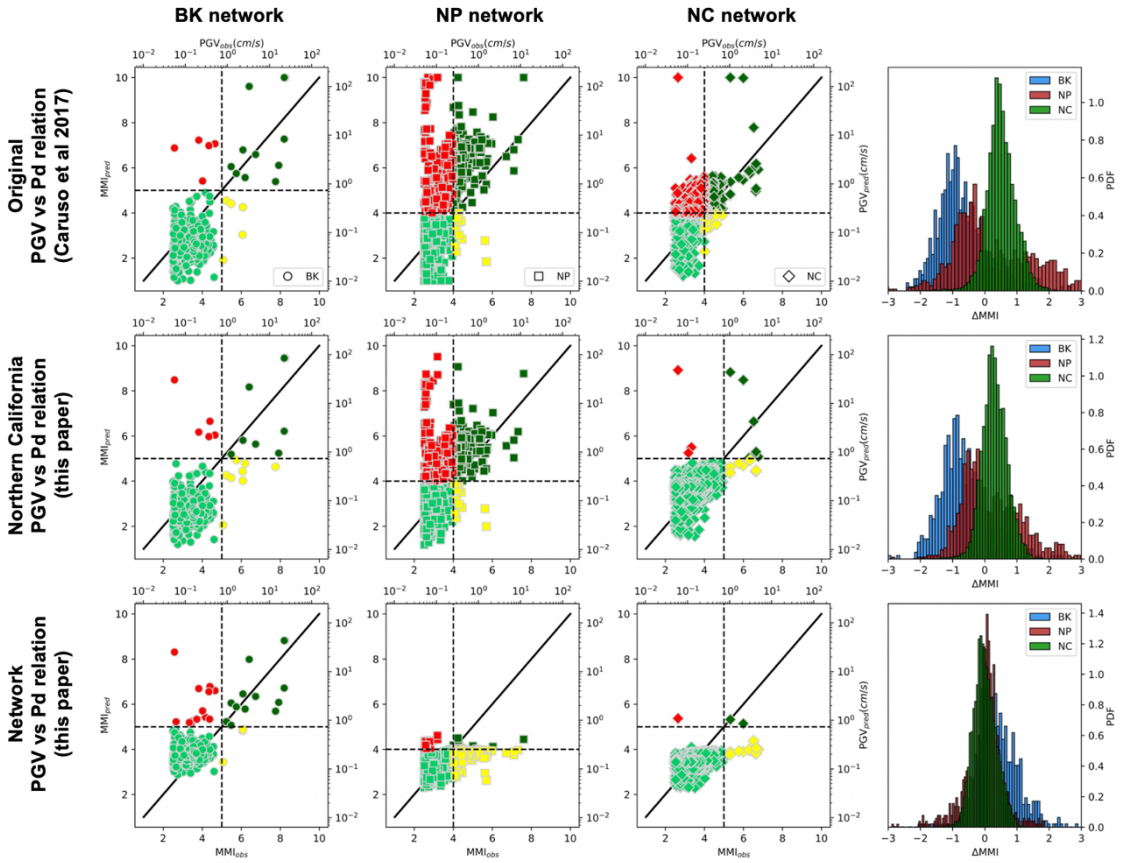


*Figure 3.3.9: Application to continuous waveforms in 3 second PTW. Lightgreen markers are Successful No-Alert; darkgreen markers are Successful Alert; yellow markers are Missed Alert; red markers are False Alert. The first three columns show the results of MMI prediction for each network. From first column to third: BK, NP and NC (plotted with circles, squares and diamonds respectively). Vertical and horizontal dashed line is the best MMI threshold for each network; black thick line is the one-to-one MMI line. Last column shows the distribution of prediction error on MMI for the three networks, represented in different colors. Rows show the results of different relation used to estimate MMI from predicted PGV. From first row to last: application of the Caruso 2017 PGV vs Pd empirical law, Northern California PGV vs Pd empirical law obtained in this paper, Network based PGV vs Pd empirical law obtained in this thesis.*

The off-line application of SAVE on California suggests that an operating on-site system could be coupled with the regional ShakeAlert system. Although there is still an open debate on the feasibility of characterizing earthquakes from the early stage of P-waves onset ((Meier et al., 2016) (Trugman et al., 2019) (Colombelli et al., 2020)), the predicted MMI, that is SAVE final output, allows to build a threshold system. Its performance shows a good agreement (see Figure 3.3.10) for MMI threshold values that ShakeAlert makes use of to issue an alert, in the range going from perceived light shaking to light damage (Kohler et al., 2020). The variation we observe both in precision and in recall is driven by the trade-off between False/Missed Alerts and MMI threshold. That is particularly evident for the off-line test on continuous waveforms. In fact, we can observe two borderline cases in Figure 3.3.10: BK network is shown to be quite stable in precision

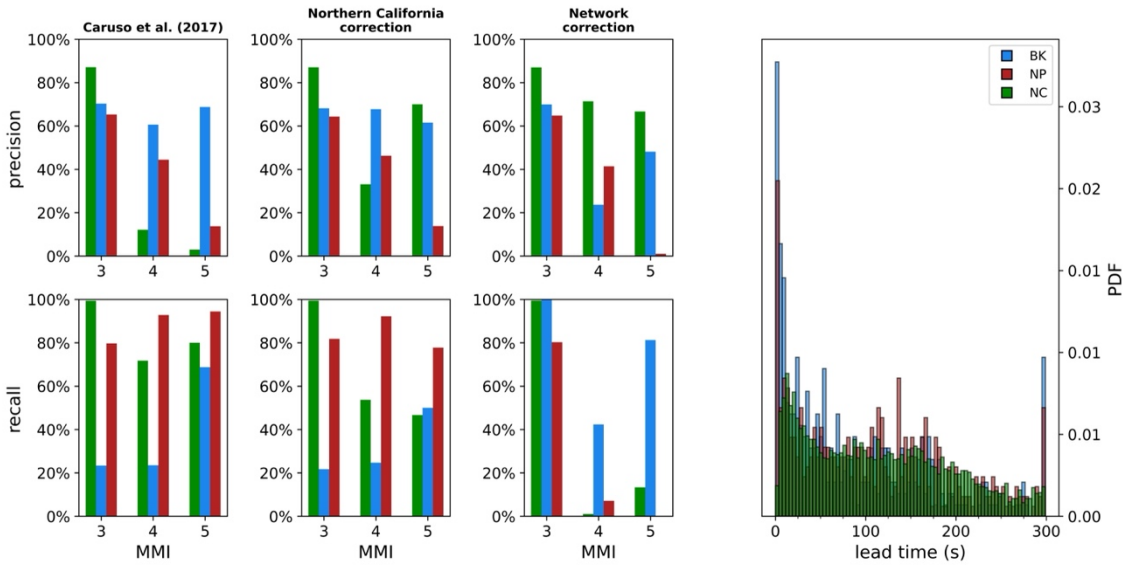


*Figure 3.3.10: Precision, recall and lead time distribution at three Northern California seismic networks. Upper rows show precision at BK, NP, NC seismic networks; lower rows show recall at the same networks. Column indexing follows the type of calibration applied to empirical PGV vs Pd law. Extreme right panel shows the distribution of lead time for each network. For all three networks peak of distribution is between 0 and 25 seconds since P-wave detection at the station.*

at all MMI thresholds with no correction applied, while a tailored empirical law shows an improvement in recall at a higher MMI threshold. In contrast, the NP network has a poor resolution in precision with Caruso et al. (2017) original law but a network-based calibration seems insufficient to improve the system response. The NP network was built to monitor earthquake shaking in densely populated areas, which is why many sensors are placed in man-made structures. The P-wave content might still be masked by the background noise indicating the need for high quality (quiet) installation sites for SAVE applications. Including uncertainties from GMPE and weighing PGA and PGV contributions in MMI evaluation is used for EEW systems (Saunders et al., 2020). Another path that can be explored is the introduction of single-station corrections.

The dependence of SAVE performance on the setting of a MMI threshold poses a challenging question on how high the alerting threshold should be (Minson et al., 2019). For an operating on-site system in Northern California, we observe that a higher alerting threshold (MMI=5) would provide adequate percentage in precision and recall with reasonable warning times (Figure 3.3.5 and last column of Figure 3.3.10). In terms of a user-oriented system, this result makes SAVE a suitable on-site solution. Usually, high alerting thresholds mean low number of false alert and increased number of missed alerts; low alerting thresholds mean low number of missed alerts but, as a consequence, users tend to be over-alerted (Cochran and Husker, 2019). SAVE might provide a valid

compromise, issuing fast reliable alerts, that could be integrated with information coming from the regional EEWS ShakeAlert in Northern California.

*Table 3-1:* Performance statistic for the continuous waveforms test using 3 seconds PTW and different calibration PGV vs $P_d$ empirical laws to get expected MMI.

| PGV VS $P_D$ LAW | NETWORK | $\mu_{\Delta MMI}$ | $\sigma_{\Delta MMI}$ | $MMI_{THRESHOLD}$ | TOTAL FA | TOTAL MA |
|---|---|---|---|---|---|---|
| **CARUSO ET AL. 2017** | **BK** | -0.7081 | 0.8398 | 3 | 318 | 10 |
| | | | | 4 | 65 | 5 |
| | | | | 5 | 5 | 2 |
| | **NP** | 0.4752 | 1.5537 | 3 | 165 | 79 |
| | | | | 4 | 195 | 12 |
| | | | | 5 | 213 | 2 |
| | **NC** | 0.5134 | 0.449 | 3 | 1059 | 43 |
| | | | | 4 | 2452 | 133 |
| | | | | 5 | 390 | 3 |
| **NORTHERN CALIFORNIA** | **BK** | -0.6836 | 0.7917 | 3 | 42 | 325 |
| | | | | 4 | 10 | 64 |
| | | | | 5 | 5 | 8 |
| | **NP** | 0.3413 | 1.1830 | 3 | 177 | 71 |
| | | | | 4 | 180 | 13 |
| | | | | 5 | 174 | 8 |
| | **NC** | 0.31 | 0.40 | 3 | 1063 | 40 |
| | | | | 4 | 511 | 218 |
| | | | | 5 | 3 | 8 |
| **NETWORK CALIBRATION** | **BK** | 0.4749 | 0.6721 | 3 | 178 | 1 |
| | | | | 4 | 116 | 49 |
| | | | | 5 | 14 | 3 |
| | **NP** | -0.026 | 0.611 | 3 | 170 | 77 |
| | | | | 4 | 17 | 156 |
| | | | | 5 | 0 | 36 |
| | **NC** | -0.002 | 0.366 | 3 | 1068 | 37 |
| | | | | 4 | 2 | 466 |
| | | | | 5 | 1 | 13 |

The application of SAVE in California leads to interesting observations. We let the system run on earthquakes of different tectonic settings (Japan, Central Italy, Southern Italy, Turkey, California) and large magnitude range (around 3.5 and up to ~7.5). We showed (in paragraphs 3.2) that SAVE can be easily adapted and calibrated without any big computational effort. For future EEW implementations, SAVE could represent a powerful tool (e.g. it could be integrated in smartphone apps to issue fast alerts at users' sites or it could be a seismic module for multidisciplinary risk mitigations platforms).

## 3.4 Implementation of the onsite EEWS SAVE at Campi Flegrei Caldera, Italy during the unrest crisis

### 3.4.1 Volcanological setting, bradyseism and earthquake activity at Campi Flegrei Caldera

The Campi Flegrei volcano (geographical location in Figure 3.4.1) is characterized by a nested caldera structure which is the consequence of two explosive eruptions, known as the Campanian ignimbrite (CI) and the Neapolitan yellow tuff (NYT) (Vitale and Isaia, 2014). The volcanism has been fed by a complex magmatic system. This system includes


*Figure 3.4.1: Location of the Campi Flegrei volcano. The caldera hosts almost one million of people living in the metropolitan area of Napoli. (this map has been taken from the web site page of INGV-Osservatorio Vesuviano sezione di Napoli link accessible at https://www.ov.ingv.it/index.php/monitoraggio-sismico-e-vulcanico/campi-flegrei/campi-flegrei-storia-eruttiva?view=article&id=66:ubicazione-campi-flegrei&catid=13:vulcani-della-campania)*

a deep (8 km depth) and widespread reservoir (Zollo et al., 2008). Above the magmatic system, a hydrothermal system has developed and its presence is testified by soil degassing and fumarole. The caldera has been affected by short-term deformation episodes, known as bradyseismic events, which have been documented since 1950s (Del Gaudio et al., 2010). The two most rapid phases of ground uplift occurred in 1970-72 and in 1980-84 (Scarpa et al., 2022). A long subsidence phase followed between 1985-2005. Since 2005 a new monotonic uplift episode has started, with a particular acceleration in

seismicity from 2014 onwards (Bevilacqua et al., 2022). The cause of bradyseism is still under debate. One hypothesis is the intrusion of magma at shallower depths, causing changes in pressure and volume which lead to deformations (Kilburn et al., 2023); another hypothesis that could explain the phenomenon is the poroelastic response of the shallow hydrothermal system, behaving as a constrain for the fluid migration processes happening at depth (De Landro et al., 2017).

Most of the seismicity associated with bradyseism occurs inland typically at shallow depths and small value of duration magnitude (Md<1). However, in the early 2023 there has been an increase of the average magnitude per month, with the occurrence of the Md=4.2 event at the end of September (Md=4.2), the highest duration magnitude since the beginning (in 2005) of the new bradyseismic crisis.

### 3.4.2 Multi-Risk Impact-based Early Warning at Campi Flegrei

The Campi Flegrei area is home to almost 1 million people. The sudden upwelling of the Pozzuoli area has caused damage and fracturing of houses and walls. In this context it is crucial to monitor the unrest phase of the volcano to support Civil Protection Authorities (CPAs) and first responders. The metropolitan area of Pozzuoli (in Figure 3.4.1) is one of the pilot sites of a 4-year long European innovation action under the Horizon Europe Framework Programme called "*GeO and weather multi-risk impact Based Early warning and response systems supporting rapid deploYment of first respONders in EU and beyond" (GOBEYOND)*.

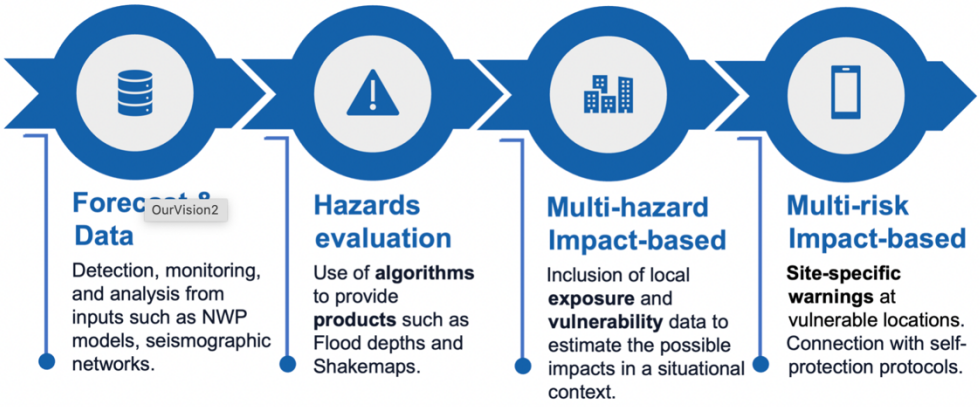


*Figure 3.4.2: MR-IEWS scheme which GOBEYOND aims at realizing (from webpage https://gobeyond-project.eu/the-project/)*

GOBEYOND aims at revolutionizing Disaster Risk Management (DRM). The goal is to develop a Multi-Risk Impact-based Early Warning System (MR-IEWS) for geo and weather hazards. The MR-IEWS will integrate the latest advancements in observation

systems, real-time data, local layers, predictive algorithms and platforms for impact forecasting, to provide timely and accurate warnings that can turn into actionable decisions (scheme in Figure 3.4.2). The local demonstrations will focus on using the high-resolution information available at local level to develop specific protocols of response actions to be triggered by the impact forecasting products of the MR-IEWS.

The unrest crisis affecting the Campi Flegrei Caldera represents a legitimate scenario to test and validate on-site earthquake early warning algorithms, such as SAVE that has the potential to be the product of the MR-IEWS related to the earthquake forecasting. In next paragraph we present the preliminary results of a retrospective SAVE test on the Md 4.2 event of September 2023.

### 3.4.3 Off-line test on the Md 4.2 earthquake of 27 September 2023

Retrospectively, we evaluated the performance of SAVE on one of the largest magnitude events recorded at Campi Flegrei in Sept, 27, 2023, through the off-line playback of recorded waveforms. Source parameters are reported in and the event location, evaluated by the Italian National Institute of Geophysics and Vulcanology (INGV), is represented in Figure 3.4.3. For the off-line test, we let SAVE algorithm run on the waveforms which recorded the event at the stations closest to the event epicenter.

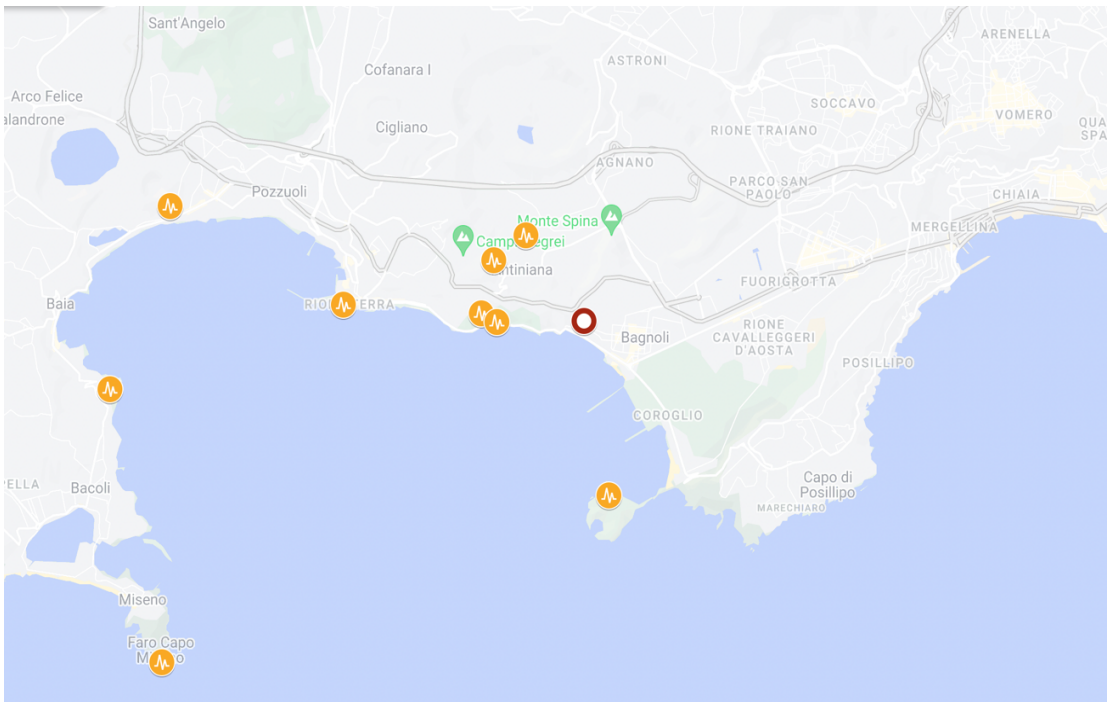


*Figure 3.4.3: Event location from INGV bulletin page (link https://terremoti.ov.ingv.it/gossip/flegrei/). The red point indicates the earthquake. Yellow points are available seismic stations used for the test.*

*Table 3-2: INGV source parameters of the Campi Flegrei earthquake used for the off-line test.*

| ORIGIN TIME (UTC) | LAT | LON | DEPTH (KM) | MAG |
|---|---|---|---|---|
| 2023/09/27 01:35:34 | 40.8192 | 14.1590 | 2.8 | 4.2±0.3 Md |

The results we show here are obtained from the analysis of the vertical component of the acceleration at the available stations of the INGV network. As described in paragraph 3.1, the system requires a tuning phase where the user set threshold levels for automatic picking and data quality control. For the off-line test of this event, we used the threshold values of the original paper (Caruso et al., 2017).

In Figure 3.4.4 we represent the results of SAVE test in terms of predicted PGV and MMI. The predicted PGV is evaluated from Pd, using the empirical scaling laws obtained for Italy by Caruso et al. 2017 (Caruso et al., 2017). The expected shaking intensity at the site is evaluated from Faenza and Michelini relationship (Faenza and Michelini, 2010). The observed PGV is evaluated from the horizontal components of velocity. In one second PTW the expected MMI at the sites matches the observed MMI within the errors (panel A of Figure 3.4.4), although we already observe a systematic overestimation. The highest MMI values are retrieved for the closest stations to event epicenter (less than 2.5 km). In one second since the first P-wave arrival, SAVE correctly predicts a maximum PGV value of 2 cm/s, corresponding to MMI around 5 (very light shaking). This result agrees with the shakemap evaluated by INGV retrospectively when the earthquake ended (for reference see https://terremoti.ingv.it/it/event/36299321). The seismic waveforms of the furthest stations (less than 8 km) that still pass through SAVE data quality control, show a predicted intensity which is two level smaller than the one obtained from the closest stations. Giving the fact that the maximum epicentral distance between the closest and the furthest station used in the off-line test is less than 10 km, the great decrease of predicted (and also observed) MMI is mostly related to attenuation effects due to volcanic rocks of the Campi Flegrei caldera (Iervolino et al., 2024). When we move to 2 and 3 seconds PTWs, it is more evident that the system is overestimating the expected PGV (MMI). The overestimation is particularly clear in Panel B and C for stations at 5-8 km of distance from event epicenter. This is due to the inclusion in the corresponding PTW of secondary phase arrivals (i.e., S-waves), resulting in the overestimation of the P-peak of displacement, which, in turn, leads to the prediction of overestimated shaking values.

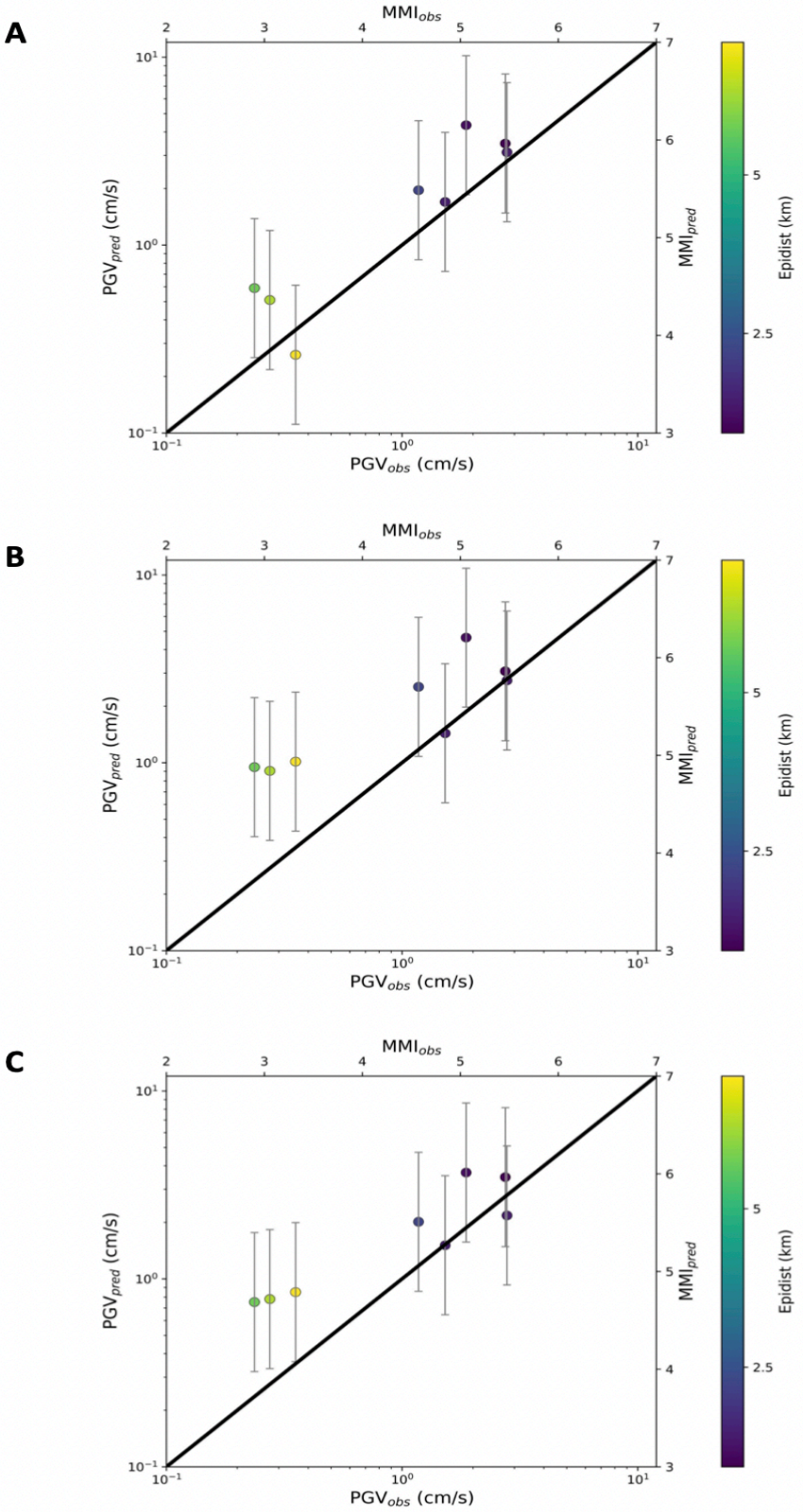


*Figure 3.4.4 Panel A: predicted PGV (MMI) versus observed PGV (MMI) using 1 second of P-Time Window. Panel B: predicted PGV (MMI) versus observed PGV (MMI) using 2 seconds of P-Time Window. Panel C: predicted PGV (MMI) versus observed PGV (MMI) using 3 seconds of P-Time Window. Points are colored following the observed source-to-station epicentral distance. Error bars represent the standard error of the corresponding PGV versus Pd relation from Caruso 2017 in each P-Time window. The black solid line in each panel is the one-to-one PGV line.*

Different strategies could overcome the issue of PGV (MMI) overestimation in the area

of interest as example: (a) refined methods for the real-time picking of the S-wave arrival or for the real-time separation of the P-phase from the S-phase such as polarization filters (Ross and Ben-Zion, 2014) might be implemented; (b) the PTWs used in the algorithm could be reduced to less than 1 second from P-wave arrival. This preliminary test showed that in future, we need to easily and rapidly move towards the (b) solution for SAVE implementation at Campi Flegrei. In order to apply the modifications, the empirical scaling laws of logPGV versus logPd need to be calibrated on the Campi Flegrei area and within shorter PTWs.

In Figure 3.4.5 we show the results of the magnitude estimation provided by SAVE at single stations. The catalog magnitude evaluated by INGV in Table 3-2 is the duration magnitude. The duration magnitude is often preferred over other magnitude scales in volcanic settings like the Campi Flegrei caldera. The duration magnitude is evaluated by taking into account the total duration of an earthquake. The energy release is measured from the duration of the observed signal after applying a station correction to reduce site effects (Castello et al., 2007). For the event we used for the test, the moment magnitude was also evaluated using the time domain approach proposed by Zollo (2022) ((Zollo et al., 2022)(Nazeri and Zollo, 2023)). The seismic moment of the earthquake is measured from the corner time and the plateau level of the LPDT curves. Indeed, it has been proved that these two parameters are directly related with the duration and the peak of the modelled source time function. The moment magnitude obtained for this event is Mw 4.2. Single-station SAVE estimate of moment magnitude is evaluated through the parameter $\tau_c$ on high quality data, as described in paragraph 3.1.2. Although single-station magnitude estimates of Figure 3.4.5 show a large variability, the average value is $M_{\tau_c}$=4.1 with $\sigma_M = 0.5$ in PTW=3 seconds. Many factors could be affecting the value we obtain on the standard deviation: (1) the filter applied on single-station displacement with highpass cut-off frequency of 0.075 Hz (Allen and Kanamori, 2003) might not be appropriate for this kind of events; (2) the selected P-time windows might be too long, leading to the inclusion of S-wave content in the analyzed signal; (3) the frequency content of the signals might be modified by attenuation effects that SAVE is not taking into account. However, the final output of SAVE is given in the form of a broad magnitude classification (see paragraph 3.1.3) so for the test on the Campi Flegrei Md 4.2 earthquake, SAVE correctly issues an alert for an expected medium ($3 < M \leq 5$) event at all the available stations.

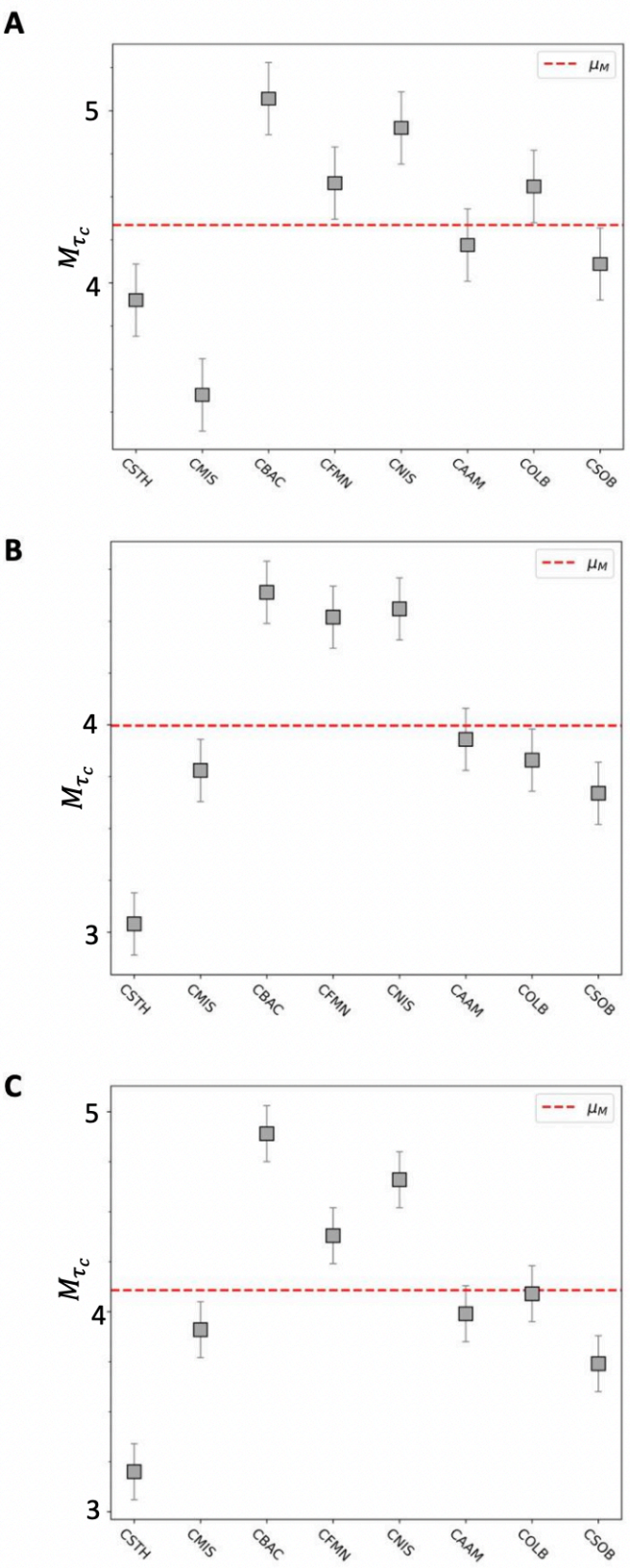


*Figure 3.4.5: Single-station estimated magnitude at the available stations in the different PTWs. The red dashed line is the average magnitude value. Error bars represent the standard error for the corresponding Mw versus $\tau_c$ laws from Caurso 2017. Panel A: magnitude values in one second PTW; panel B: magnitude values in 2 seconds PTW; panel C: magnitude values in 3 seconds PTW.*

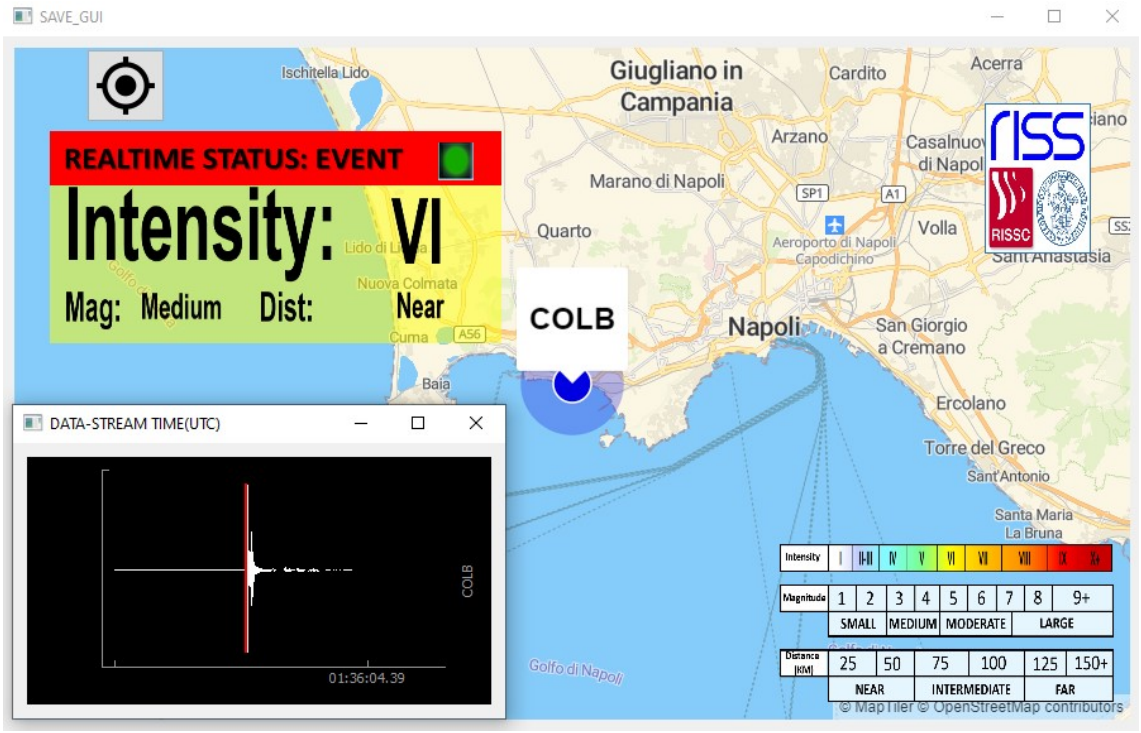


*Figure 3.4.6: SAVE graphical interface for the station COLB located at 900 meters from the event epicenter. At this station, the alert is issued for expected event of MMI=6, medium magnitude, nearby the site. The pulsing blue point on the map is the station location. In the bottom right the reference for intensity, magnitude and distance scales are represented. In bottom left the data stream of the signal is shown with the P-wave automatic pick marked with the vertical red line.*

An example of the graphical interface of SAVE for this test is shown in Figure 3.4.6 for the station COLB located at 900 meters from event epicenter.

SAVE test for the Md 4.2 earthquake at Campi Flegrei shows us, on one hand, that the system needs to be carefully calibrated to address overestimation errors (by analyzing much shorter windows than those currently used) and, on the other hand, that it could be easily adapted into a multi-hazard platform for the seismic monitoring of the metropolitan area of Pozzuoli.

# CHAPTER

# 4 Next Generation of P-wave based on-site system: P-Alert

## 4.1 P-Alert theoretical concepts

In this paragraph we describe a P-wave based on-site earthquake early warning system (P-Alert, hereinafter) developed by Colombelli et al. (2015). P-Alert methodology is straightforward and based on two key elements. The first one is the continuous measurement of the three peak amplitude parameters (which are the peak amplitude acceleration $P_a$, the peak amplitude velocity $P_v$ and the peak amplitude displacement $P_d$) on the vertical component of a single ground motion recording. The second key element is the use of the three combined peak amplitudes at the site to obtain expected PGV at the same site. The use of the three peak amplitudes $P_a$, $P_v$, $P_d$ makes the methodology more robust. The block diagram of P-Alert can be summarized into two parts: the first is an off-line calibration of the system and the second is the signal analysis with eventual alert issuing.

### 4.1.1 Calibration of PGV vs Px empirical laws and PGV threshold setting

In P-Alert algorithm, the calibration of PGV vs $P_x$ empirical laws is made upstream. The three peak amplitude parameters $P_a$, $P_v$, $P_d$ are evaluated off-line in a time window corresponding to the difference between the arrival time of S-waves ($T_S$) and the arrival time of P-wave ($T_P$). For each peak amplitude, the empirical scaling law is equal to (22) and the measurements should follow the relationship within the errors. The off-line calibration of the system makes it suitable for fast application in different regions of the world where the empirical scaling laws between PGV and Px are already available, such as Italy, Taiwan, Japan, western U.S and Turkey ((Zollo et al., 2010) (Colombelli et al., 2015) (Rea et al., 2024)). Depending on the user's needs, a threshold PGV* can be set. The PGV* threshold would result in an interval around $Px^*$, e.g. $P_{x\,L} \leq P_x^* \leq P_{x\,H}$ where $P_{x\,L}$ and $P_{x\,H}$ are the lowest and highest value around $P_x^*$ when taking into account the standard deviation of PGV vs $P_x$ law, respectively. An example of the setting of PGV* and the consequent interval of $P_x$ can be appreciated in top panel of Figure 4.1.1. The threshold PGV* is linked to the expected shaking intensity, as described in paragraph 2.2.1.1 and represents the level above which the system is calibrated to issue the alert.

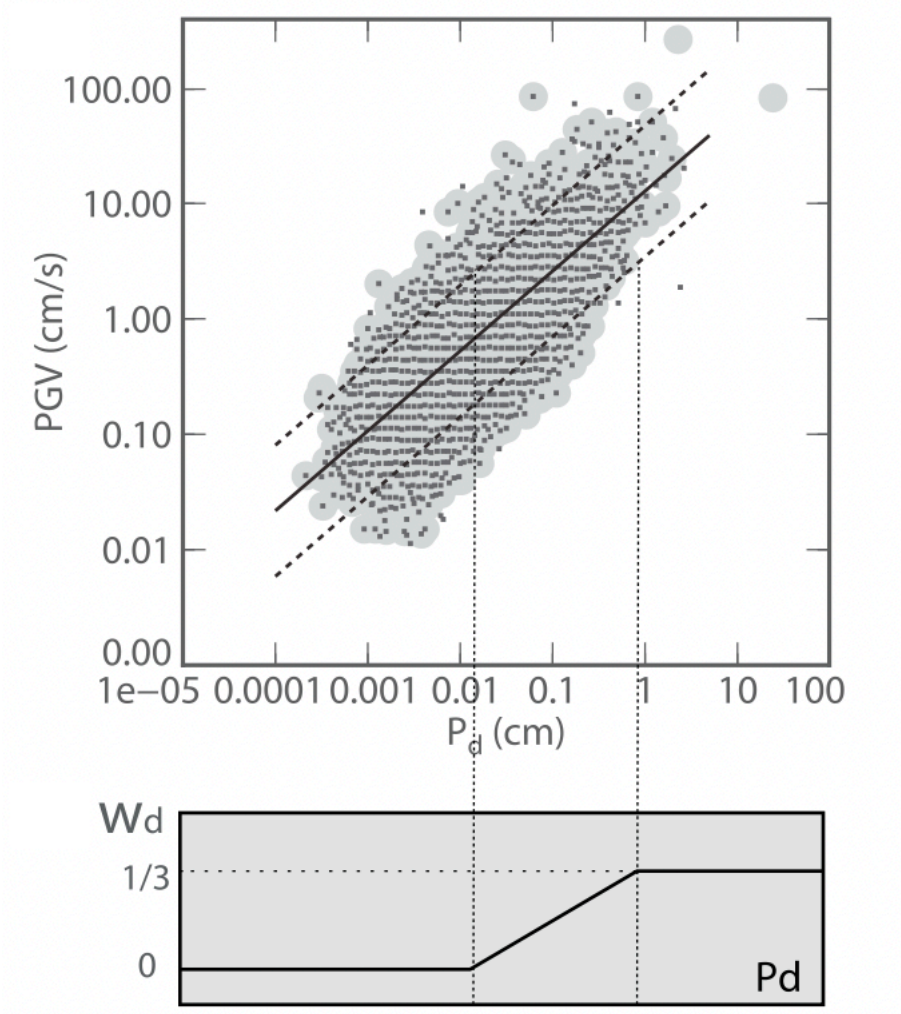


*Figure 4.1.1: Top panel: Data distribution and empirical relationships between $P_d$ and PGV. The solid black line is the best fit line, the dashed lines are the standard error of regression. The vertical dashed lines correspond to the interval of Pd values around the Pd*, obtained by fixing a threshold PGV* on y-axis. Bottom panel: example of $W_d$ definition. The observed $P_d$ parameter is compared to its threshold value and converted into a dimensionless variable, named $W_d$, which is equal to 0 in the region below the lower threshold to 1/3 in the region above the higher threshold and linearly increases between 0 and 1/3 in the intermediate region. (from Colombelli et al., (2015)).*

### 4.1.2 Signal analysis: combination of peak acceleration, peak velocity, peak displacement

After the calibration, the system can be applied on the vertical component of ground motion recordings. At each time along the seismogram, P-Alert measures $P_a$, $P_v$, $P_d$ and associates them with a fuzzy variable Wx, defined as:

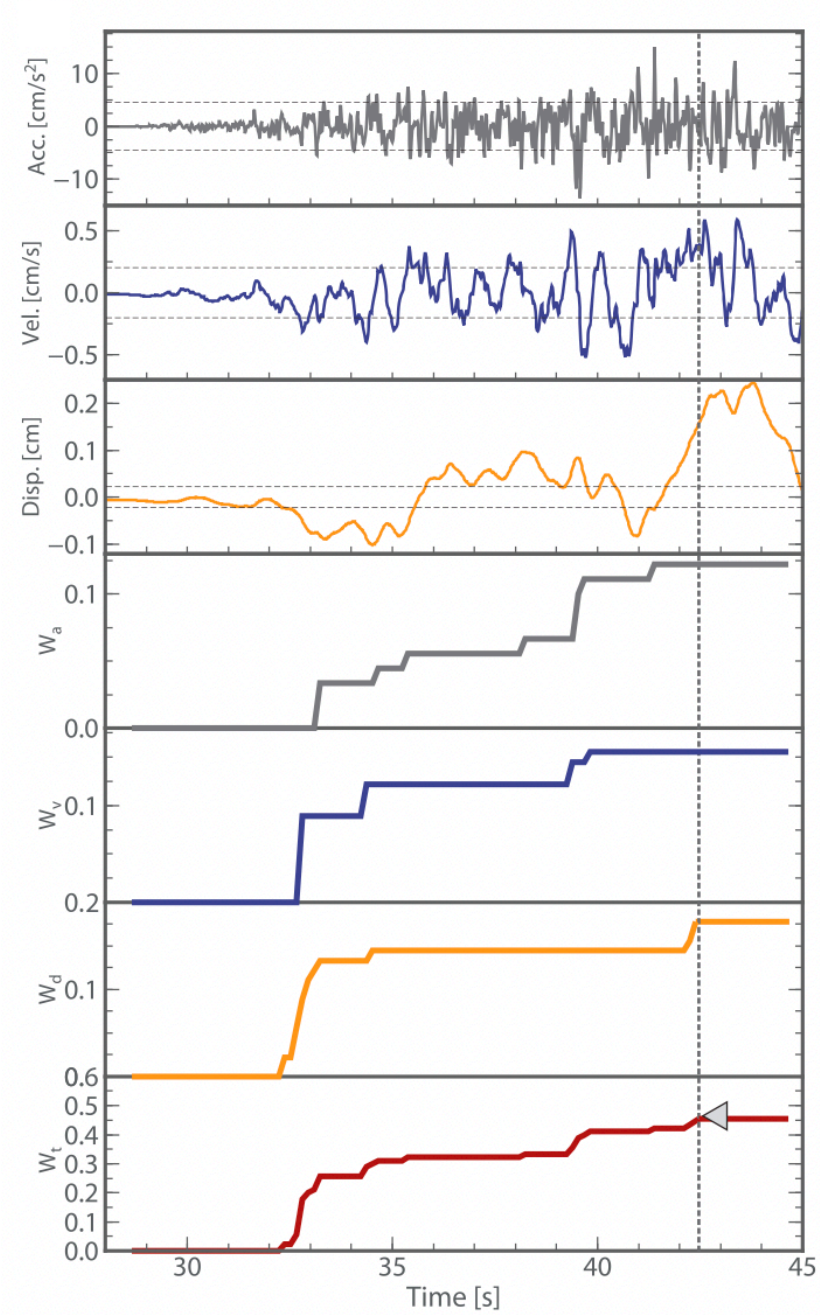


*Figure 4.1.2 Example of P-Alert workflow on a seismogram. From top to bottom: acceleration (dashed lines represent Pa* interval), velocity (dashed lines represent Pv* interval), displacement (dashed lines represent Pd* interval), fuzzy variable Wa referred to acceleration, fuzzy variable Wv referred to velocity, fuzzy variable Wd referred to displacement, fuzzy variable Wt from the sum of Wa, Wv, Wd. The gray rotated triangle shows the threshold value Wt* used for warning declaration. (from Colombelli 2015)*

$$\begin{aligned} W_x(t) &= 0 && P_x < P_{x\,L} \\ W_x(t) &= 1/3\,[(P_x - P_{x\,L})/(P_{x\,H} - P_{x\,L})] && P_{x\,L} \le P_x \le P_{x\,H} \\ W_x(t) &= 1/3 && P_x > P_{x\,H} \end{aligned} \qquad (33)$$

Where $P_{x\,L}$ and $P_{x\,H}$ are obtained from the PGV vs Px empirical law by fixing the threshold PGV*, as described in the previous paragraph. $W_X(t)$ is computed at each time

and is locked at the corresponding value until a larger value is encountered. As a result, $W_X(t)$ is a monotonically increasing stepladder-like function. Eventually the fuzzy variables are summed at each time step to get the fuzzy variable Wt, which is monotonically increasing from 0 to 1. The workflow of the scheme is presented in Figure 4.1.2.

### 4.1.3 System output: warning declaration

As system output, four different alert levels can be defined based on a threshold set on Wt, denoted Wt* hereinafter (matrix scheme of Figure 4.1.3): successful alert (SA), successful no-alert (SNA), missed alert (MA) and false alert (FA). The overall performance of the system and its reliability is controlled by the threshold on PGV and the threshold Wt*. Indeed, by varying the threshold in PGV and Wt the user can decide how selective the system might be: a change in both the thresholds has the consequence of varying the number of alerts (particularly missed and false alarms), which makes P-Alert extremely suitable for any kind of user tolerance and needs.

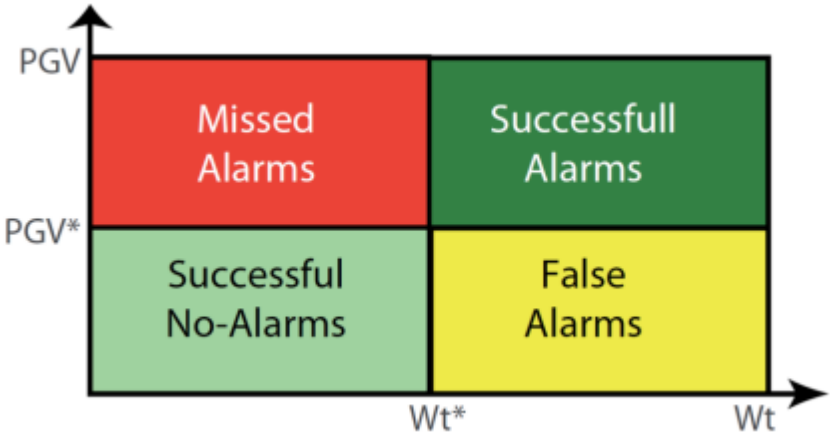


*Figure 4.1.3 Alert definition scheme. Alert categories: successful no alarm (light green zone), successful alarm (dark green zone), missed alarm (red zone) and false alarm (yellow zone).*

## 4.2 P-Alert at California

In this paragraph we present the results of the application of P-Alert in California. We perform an off-line test of P-Alert on 300 Californian events spanning a catalog time window of 20 years (from 2003 to 2023) (see Figure 4.2.1). The magnitude range goes from small to moderate and the depth range goes from very shallow (few kilometers) to deeper values (about 40 kilometers). We used records of strong motion networks with stations locations involving both Southern and Northern California regions (as shown in Figure 4.2.1). In paragraph 4.1 we described P-Alert workflow which requires (1) a calibration phase and (2) the application of the retrieved empirical laws to run the system in the region of interest. The following sub-paragraphs are focused on the results of each of the P-Alert workflow phases.

### 4.2.1 System calibration

In order to calibrate the system in California, we split the dataset presented in Figure 4.2.1 into two: one third of the available records are used for the later testing phase and two third of the available records are used for the training in the calibration phase. The dataset is divided with the constraint of maintaining the same data distribution for both the test and the train, as it is shown in Figure 4.2.2.

Firstly, we manually picked P- and S- arrivals on the records and we retrieved the P-peak of acceleration $P_a$, P-peak of velocity $P_v$ and P-peak of displacement $P_d$ from the vertical component of the waveforms in a time window equal to $T_P$-$T_S$, with $T_P$ and $T_S$ being the P- and S-arrival respectively.

Secondly, we evaluated the observed PGV from the horizontal components of velocity waveforms. We plot PGV versus $P_a$, $P_v$, $P_d$ to get the empirical scaling laws of P-Alert in California (see Figure 4.2.3). Since the majority of points have low values of observed PGV, $P_a$, $P_v$ and $P_d$, we adopted the approach used in Colombelli et al., (2015): we resampled PGV vs $P_x$ in 2D with a 0.5 cm/s step in PGV and 1 cm/s$^x$ (x=0,1,2 according to x being displacement, velocity or acceleration) step in $P_x$. We obtained the coefficients of PGV vs $P_x$ laws on the resampled sets (see Figure 4.2.3). As described in paragraph 4.1.1, the setting of a threshold for P-Alert is done during the calibration phase and it is thought to be user oriented. Once the scaling relations on which the system algorithm works are calibrated, the user can set a threshold in PGV which results in the interval values for $P_x$ that will trigger the system for eventual alert declaration. Here we set a

threshold value of PGV = 1.41 cm/s which corresponds to MMI=4 (light shaking) according to Worden 2012 intensity scale (Worden et al., 2012).

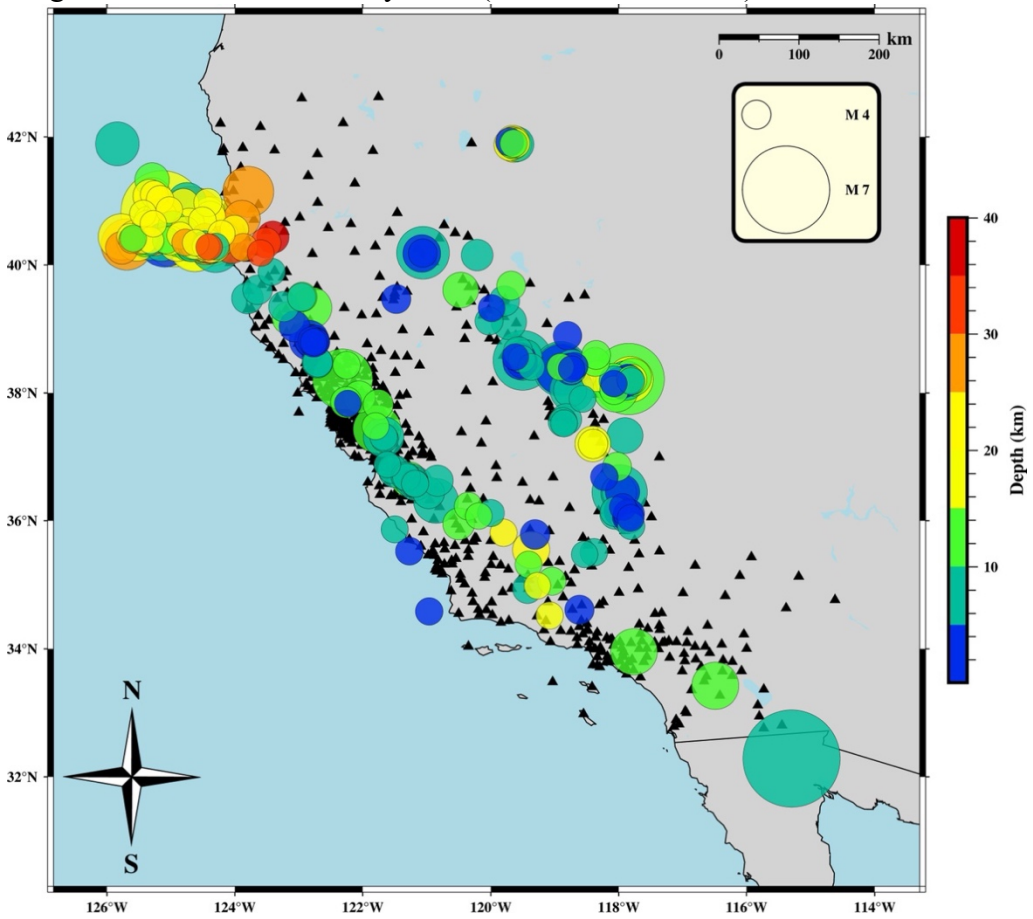


*Figure 4.2.1: Map of events whose waveforms are used to test P-Alert in California. Circles represent event locations. Marker size indicates event magnitude; the color indicates event depth. Black triangles represent seismic stations used for the analysis.*

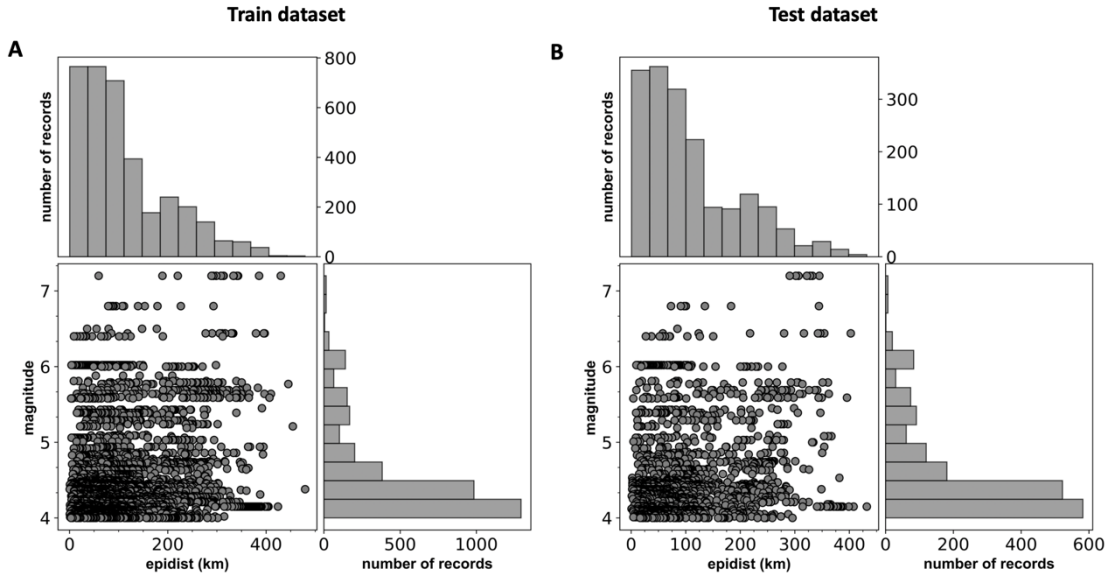


*Figure 4.2.2: Train and test dataset splitting. Panel A shows train dataset distribution of records with respect to magnitude and distance from event epicenter. Panel B shows test dataset distribution of records with respect to magnitude and distance from event epicenter.*

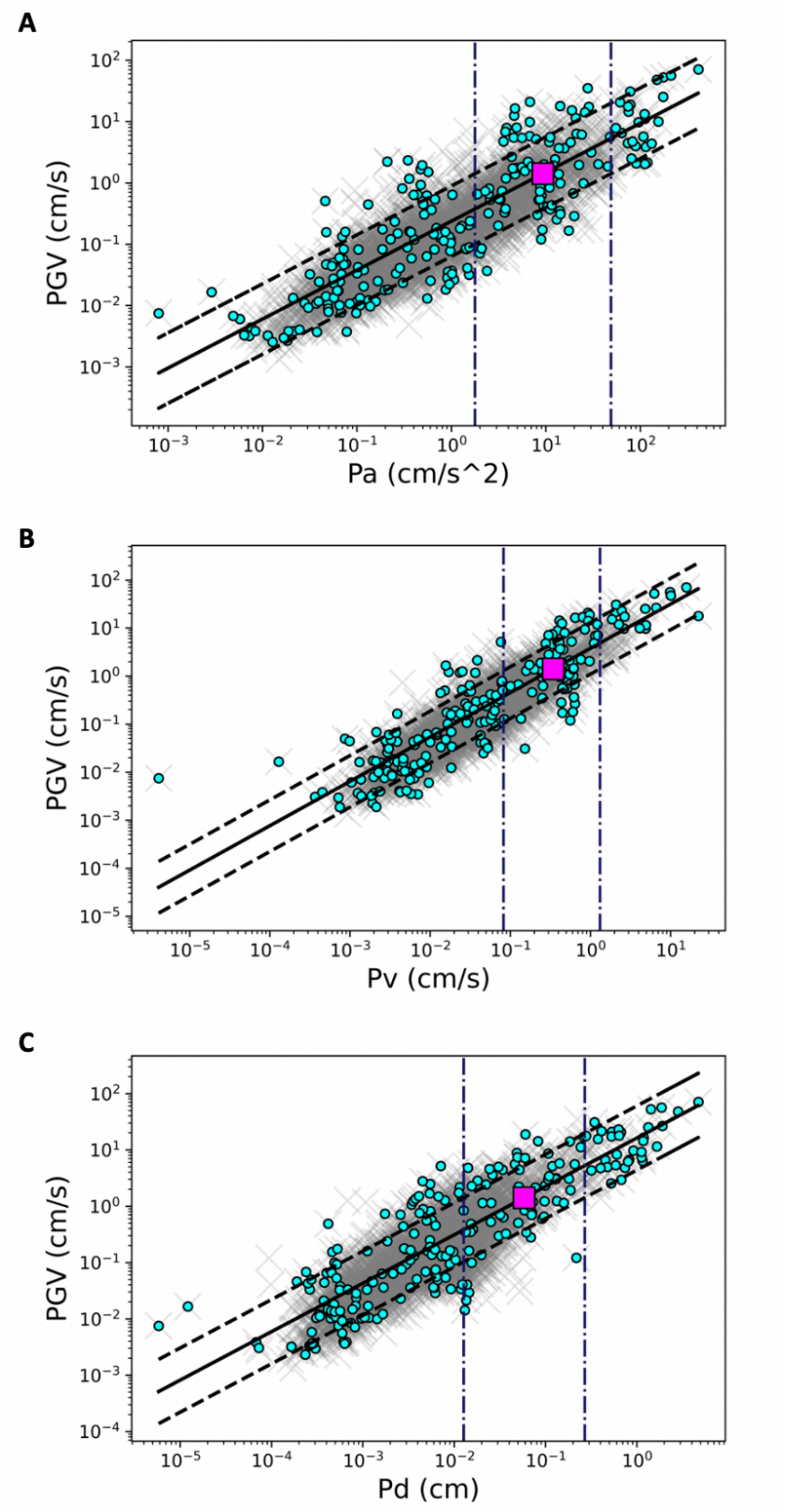


*Figure 4.2.3: Panel A represents the scaling of observed PGV versus $P_a$ on train records. Panel B represents the scaling of observed PGV versus $P_v$. Panel C shows the scaling of observed PGV versus $P_d$. In each panel the black solid line is the PGV vs $P_x$ relation; black dashed lines are the $\pm SE$ lines; the grey crosses are single values measured on each record; the cyan points are the 2D resampled dataset on which the fit is performed; the magenta square is the $PGV_{threshold}$ here set at 1.41 cm/s and the dark blue dashed-dotted lines correspond to the $P_x$ interval around the $PGV_{threshold}$.*

In table Table 4-1 we reported the values of $P_x$ intervals that allow to build the fuzzy variables $W_x$. As described in paragraph 4.1.2, the fuzzy variables are step-wise functions that monitor the growth of acceleration, velocity and displacement. The combination of the three variables is the fuzzy variable $W_t$ that takes into account any variation in the three physical parameters of the ground: when the variation in the peak is observed on the three of them, that is $W_t$ is higher than a threshold $w_t$*, the system is triggered for alert issuing.

*Table 4-1 Retrieved values for $P_a$, $P_v$, $P_d$ to build the corresponding fuzzy variables. Low and High values take into account the standard errors coming from PGV versus $P_x$ relationships. $P_x(PGV_{threshold})$ is the central value of PGV vs $P_x$ laws at $PGV_{threshold}$=1.41 cm/s in this study.*

| | $P_{x\,HIGH}$ | $P_{x\,LOW}$ | $P_x(PGV_{threshold})$ |
|---|---|---|---|
| **ACCELERATION (CM/S$^2$)** | 55 | 1.7 | 9.6 |
| **VELOCITY (CM/S)** | 1.5 | 0.1 | 0.4 |
| **DISPLACEMENT (CM)** | 0.25 | 0.01 | 0.06 |

To set a threshold for the fuzzy variable $W_t$, first we built the fuzzy variables $W_a$, $W_v$, $W_d$ for each record of the train dataset. The fuzzy variable $W_x$ has a zero value under a certain threshold in $P_x$, has a linear growth (with known slope) depending on the $P_x$ interval relative to $PGV_{threshold}$ and has a maximum value of $1/3$ when the upper $P_x$ value is reached. Here we slightly modified the approach described in paragraph 4.1.2 from Colombelli et al., (2015.) The maximum value for the fuzzy varialble $W_x$ is declared as soon as the corresponding $P_x$ value is higher than $P_x(PGVt_{reshold})$ which is the central measure retrieved from the calibrated PGV vs $P_x$ laws (magenta squares of Figure 4.2.3). The reason of this choice relies on the fact that we want the system to be as fast as possible in triggering an event. We also noticed that the high $P_x$ measure on PGV vs $P_x$ plus its standard deviation and the central value on PGV vs $P_x$ relationship are of the same order of magnitude (Table 4-1). Indeed, from Figure 4.2.3 it is clear that the measures are well distributed around the PGV vs $P_x$ line with very few scattered points.

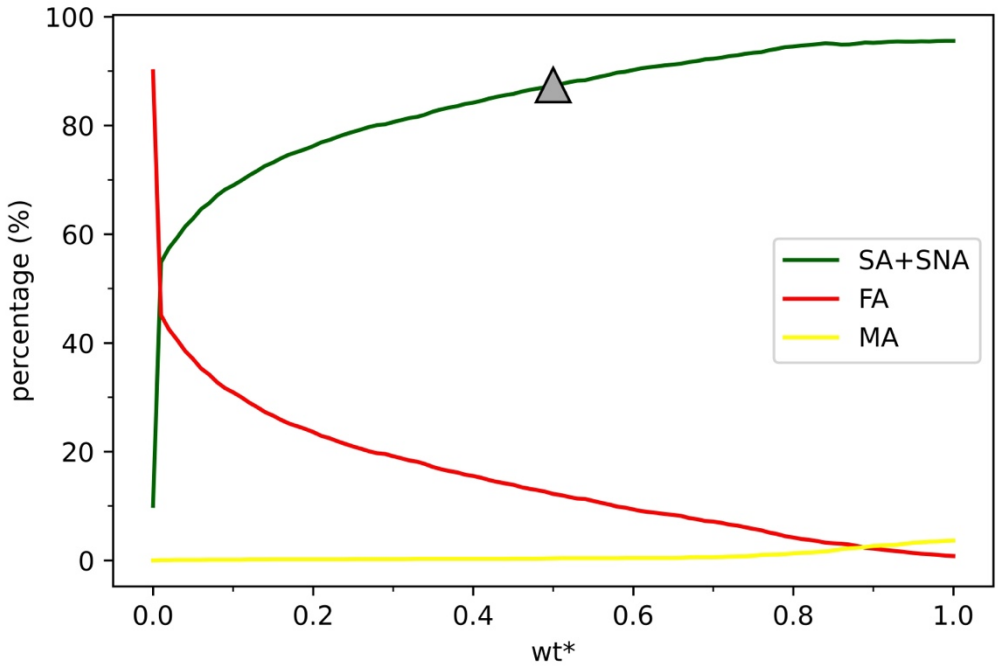


*Figure 4.2.4: Calibration curves obtained from the train dataset. The darkgreen line represents the percentage of Successful Alerts and Successful No-Alerts with respect to the threshold wt*; the red line represents the percentage of False Alerts with respect to wt*; the yellow line represents the percentage of Missed Alerts with respect to wt*. Darkg rey triangle is the value of wt* which corresponds to 85% of SA+SNA; 20% of FA and about 5% of MA.*

Once we have let the algorithm run on each available records of the train dataset, we get the measures of $P_a$, $P_v$, $P_d$ and their respective fuzzy variable $W_a$, $W_v$, $W_d$ along the seismograms. The sum of $W_a$, $W_v$, $W_d$ is the fuzzy variable $W_t$, that is monitored for potential alert issuing. According to how $W_t$ is built, we let $w_t$* vary in a range between 0 (lowest feasible value) and 1 (highest feasible value). We count the number of Successful Alert, Successful No-Alert, Missed Alert and False Alert following the matrix scheme of Figure 4.1.3 here reported as it follows:

$$\text{Successful Alert (SA): } W_t > w_t^* \ \& \ PGV_{obs} > PGV_{threshold}$$

$$\text{Successful No Alert (SNA): } W_t \leq w_t^* \ \& \ PGV_{obs} \leq PGV_{threshold}$$

$$\text{False Alert (FA): } W_t \geq w_t^* \ \& \ PGV_{obs} < PGV_{threshold}$$

$$\text{Missed Alert (MA): } W_t < w_t^* \ \& \ PGV_{obs} \geq PGV_{threshold}$$

The result of the scheme above is shown in Figure 4.2.4 in the form of calibration curves. The calibration curves give quantitative information about the total number of SA, SNA, FA and MA. Figure 4.2.4 shows the dependence of the calibration curves on the threshold

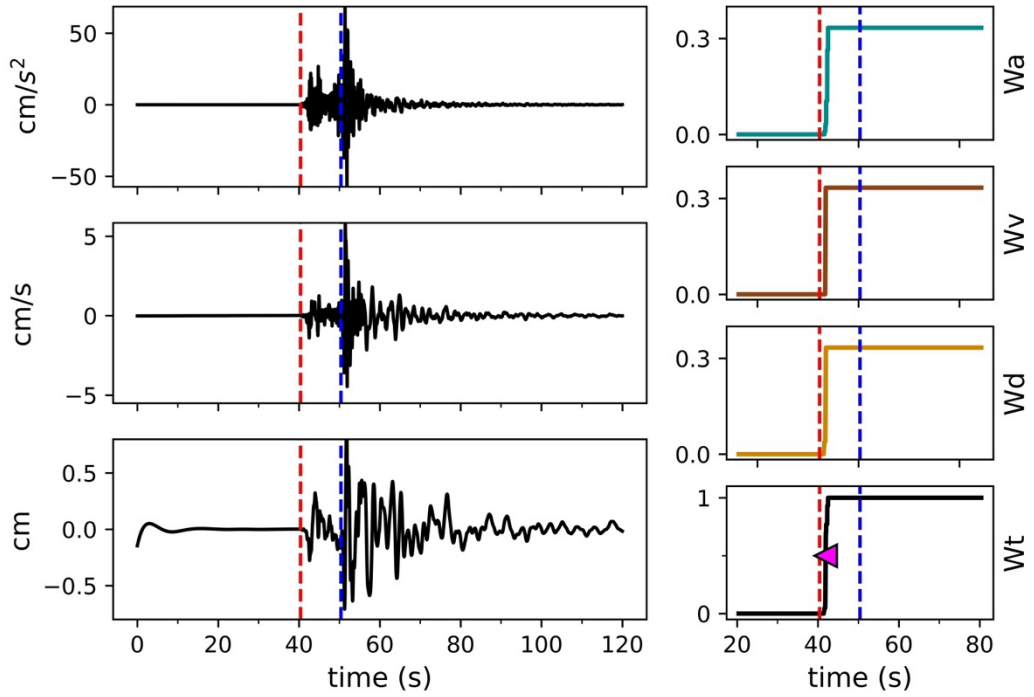


*Figure 4.2.5: Example of P-Alert application on the station KHMB record of the Mw 6.4 Ferndale earthquake happened on 2022/12/20 at 10:34:24 UTC. The epicentral distance is 70 km. On the left side of the figure from top to bottom it is represented the vertical component of acceleration; the vertical component of velocity; the vertical component of displacement. The time is relative to the beginning of the trace. The dashed red line marks the P-wave arrival. The dashed blue line marks the S-wave arrival. On the right side of the figure from top to bottom it is represented the fuzzy variable related to the peak acceleration Wa; the fuzzy variable related to the peak velocity Wv; the fuzzy variable related to the peak displacement Wd; the fuzzy variable Wt, sum of Wa, Wv, Wd. The magenta triangle marks the threshold wt* at which the system issues an alert, warning for expected PGV>1.41 cm/s (MMI>4).*

wt*. Moreover, from Figure 4.2.4 it is possible to explain the reason why P-Alert is a very user-friendly and user-oriented on-site system: the users could select the threshold $w_t$* that best matches their needs/tolerance (e.g minimum number of FA, minimum number of MA or maximum number of SA+SNA), effectively deciding with the calibration curves how strict he wants to be. For the application of the system on the test dataset, we chose a threshold value wt*=0.5 corresponding to 85% of the sum of SA and SNA. The choice was driven by a trade-off between lower wt* thresholds which would results in high percentage of MA and FA and higher wt* thresholds which would be too strict as the algorithm waits for $P_a$, $P_v$, $P_d$ to reach maximum levels to be triggered on $W_t$.

### 4.2.2 System testing

Once we calibrated the system, we applied it on the test dataset of Figure 4.2.2. An example on one record is presented in Figure 4.2.5. We reported the P- and S-picks (dashed blue and red line respectively) to show that P-Alert was triggered when the P-wave arrived at the station, warning for an event that was rightfully over the chosen PGV threshold of 1.41 cm/s (MMI=4). The S-wave content for stations close to event epicenter often corresponds to the PGV arrival at the same site. Moreover, from Figure 4.2.5 it is possible to see how the system is jointly monitoring acceleration, velocity and displacement through the corresponding fuzzy variables and it is declaring a warning as soon as the three of them are coherent with the calibrated threshold values.

The lead time here is defined as:

$$Lead\ Time = T(PGV_{threshold}) - T(w_t^*) \tag{34}$$

where $T(PGV_{threshold})$ is the time on the velocity waveform at which the observed PGV is equal to the threshold PGV, $T(w_t^*)$ is the time at which the fuzzy variable Wt first reaches the threshold level wt*. From the definition of Lead Time in equation (34) and the scheme for alert classification in paragraph 4.2.1, only Successful and False Alert can be taken into account in the lead time analysis, because for both of them there has been a warning declaration coming from the fact that the fuzzy variable Wt has overcome the threshold. The plot of lead time for the test dataset is presented in Figure 4.2.6. The zero value means for that record the system triggered exactly at the arrival of PGV=1.41 cm/s at the site. On average we found that for stations at 100 km the available lead time is about 10 seconds. This result is comparable to the one obtained for SAVE in paragraph 3.3.2. However, it is worth to mention that SAVE requires at least one second after the automatic picking of P-wave phase to issue an alert and the lead time SAVE can provide is based on the arrival of the PGV at the site. On the contrary, P-Alert does not require any P-phase identification (although it intrinsically uses the information coming from P-wave), the alert is issued as soon as the threshold level is reached and the lead time refers to the arrival time of the threshold PGV (here PGV=1.41 cm/s), whereas the highest PGV might reach the recording station even later, effectively increasing the available time to take actions. This means that the Figure 4.2.6 shows the minimum available lead time for P-Alert, which seems to be in agreement to what SAVE could provide at the same

epicentral distances and for the same range of magnitude (see Figure 3.3.5 for comparisons).

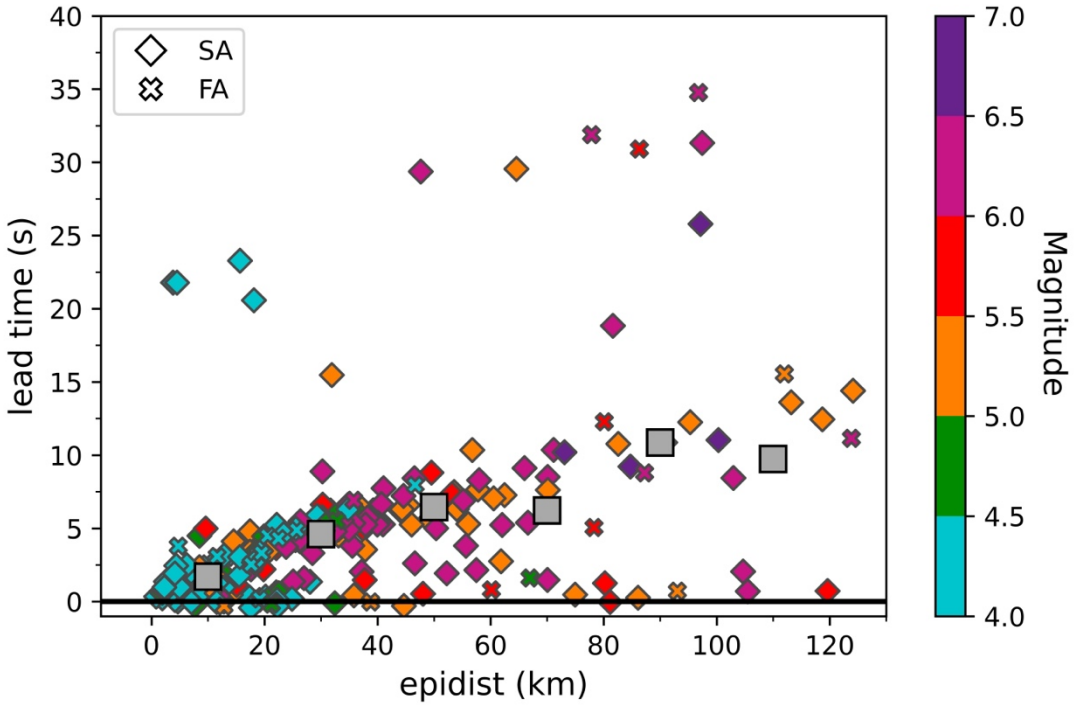


*Figure 4.2.6: Lead time plot for the test dataset. The lead time is defined as the time at which the $PGV_{threshold}$ is observed at the station and the time at which the fuzzy variable Wt first overcome the threshold wt* set to issue alerts. Marker colors follow event magnitude; marker types represent either False or Successful Alert. Darkgrey squares are averaged lead time values (bin width = 20 km).*

The system perfomance is shown in the pie chart of Figure 4.2.7. We evaluated the total number of Successful Alert, Successful No-Alert, Missed Alert and False Alert according to the scheme presented in the previous paragraph 4.2.1. We noticed that the percentage of SNA is above 86%. This result is expected, given the high number of records for event having magnitude smaller than 5. This subset of records populates most of the test dataset distribution also at distance greater than 50-100 km where it is feasible not to expect a PGV overcoming the chosen $PGV_{threshold}$=1.41 cm/s (MMI=4) (see Figure 4.2.2). Moreover, in the calibration phase of the system (see paragraph 4.2.1), we set a threshold in Wt which assured a percentage of overall success (SNA+SA) of 85% on the calibration curve, so the test is completely in agreement to what we observed previously. It is interesting to highlight the fact that the total number of SA is ten times bigger that the total number of MA+FA. Indeed, when we evaluated the precision and the recall for P-Alert in the same way as we did for the application of SAVE, we obtained that for this application of P-Alert the precision is equal to 89% and the recall is equal to 98%.

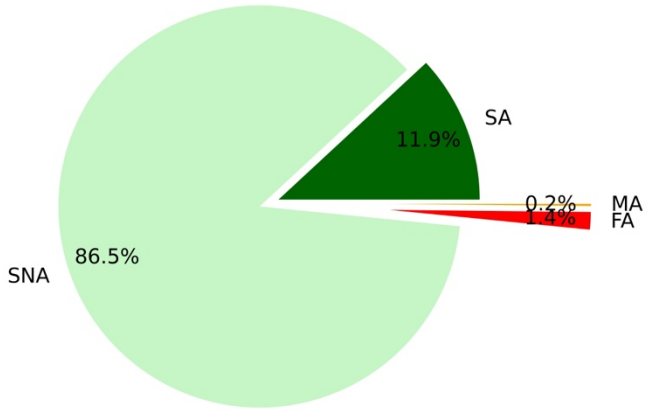


*Figure 4.2.7: Pie chart of P-Alert performance. Successful Alerts (SA) (in darkgreen) refer to a threshold PGV value of 1.41 cm/s (corresponding to MMI=4 according to Worden et al. 2012 scaling law). The percentage of False Alerts (in red) is one order of magnitude smaller than the percentage of SA. The percentage of Missed Alerts (in yellow) is two orders of magnitude smaller than the percentage of SA.*

The performance of P-Alert shows that there is a change in the on-site systems performance when limited or unlimited P-time windows are taken into account. The application of two different on-site systems in the same tectonic setting and on the same events is useful to highlight the aforementioned difference. From Figure 3.3.7 in paragraph 3.3.2, we can observe that the values of recall and precision for SAVE system, which works on the same MMI threshold for alert issuing (MMI=4), never reach the values obtained by P-Alert which was set to work at the same MMI threshold for this test. SAVE uses a limited P-time window (PTW max = 3 seconds since P-arrival), while for P-Alert no limitation on time is imposed. This is the reason why we observed a substantial reduction of MA.

# PART 3 – NEW PERSPECTIVES FOR EARTHQUAKE EARLY WARNING

The EEW algorithms and their applications provide a great insight into the earthquake physics. The complete characterization of the earthquake source obtained from the analysis of few seconds of available seismic signals remains a very promising challenge. The greatest issue in the framework of further development of EEWS is to establish whether the earthquake rupture has an intrinsic differentiation in the way the process starts and propagates and whether this differentiation depends on the final earthquake size. In Part 1 and Part 2 we focused the discussion on the physical grounds behind the concept of EEW and the application of the on-site systems. However, we also highlighted how contradictory the observations about this delicate matter are until now and how the fast characterization of the final earthquake magnitude is still affected by many limitations. Therefore, in Part 3 of the discussion we put the attention on the ongoing debate about the earthquake nucleation behavior. We present the results of a global earthquake catalog showing that the earthquake rupture beginning is deterministic and final-size dependent, at least in a probabilistic sense. These results might have a significant place both in the debate on earthquake rupture physics and, particularly, in the EEW future applications since they could pave the way for a rapid magnitude estimation which is fundamental to take fast mitigation actions.

# CHAPTER

# 5 The deterministic behavior of earthquake rupture beginning and the early magnitude characterization

In this chapter we present the results of the analysis of an unprecedent global seismic catalog to support the hypothesis of the deterministic behavior of the earthquake rupture beginning. The nucleation of earthquakes is still an open debate in the seismological community. The way earthquake ruptures grow and stop determines the final earthquake size which can be quantify by its magnitude. Small and large earthquakes develop in very different time scales: the former usually take few seconds to evolve on typical length scales of few kilometers; the latter can take hundreds of seconds to evolve on typical length scales of hundreds of kilometers. If the rupture process starts in the same way for small and large earthquakes, no deterministic prediction of the final size is feasible, until the process has finished. On the contrary, if the source mechanism starts differently from its early beginning, real-time proxies can be measured on seismic waves to discriminate the final event size. In this chapter we present the results of the analysis of the early P-wave displacement performed on big number of waveforms of worldwide earthquakes spanning a wide range of magnitude and depth having locations involving different geological setting. We prove that the initial growth rate of P-wave displacement could be a proxy for the early magnitude estimation. Moreover, we discuss the implication that the results have with the physical parameters related to the earthquake source and its nucleation (e.g the stress drop and the rupture velocity). Lastly, we discuss about the impact that the feasibility of the early magnitude characterization (less than 1 seconds of P-wave signal) might have on future earthquake early warning systems implementation.

## 5.1 The analysis on a big worldwide earthquake catalog

We analyzed 200 earthquakes with magnitude ranging from 4 to 9. For each event, we used either the acceleration waveforms or the velocity waveforms, depending on data availability. In previous studies ((Colombelli et al., 2014), (Colombelli and Zollo, 2015), (Nazeri et al., 2019), (Colombelli et al., 2020)) the preliminary dataset consisted of a smaller subset of events from a specific tectonic area of the world (e.g. Japan and Central Italy). In order to investigate globally on the physics behind the beginning of the earthquake rupture, we built a massive worldwide catalog consisting of 7000 thousand records of earthquakes from different tectonic areas and geological settings, including normal fault zones, strike-slip environments and subduction zones (Figure 5.1.1).

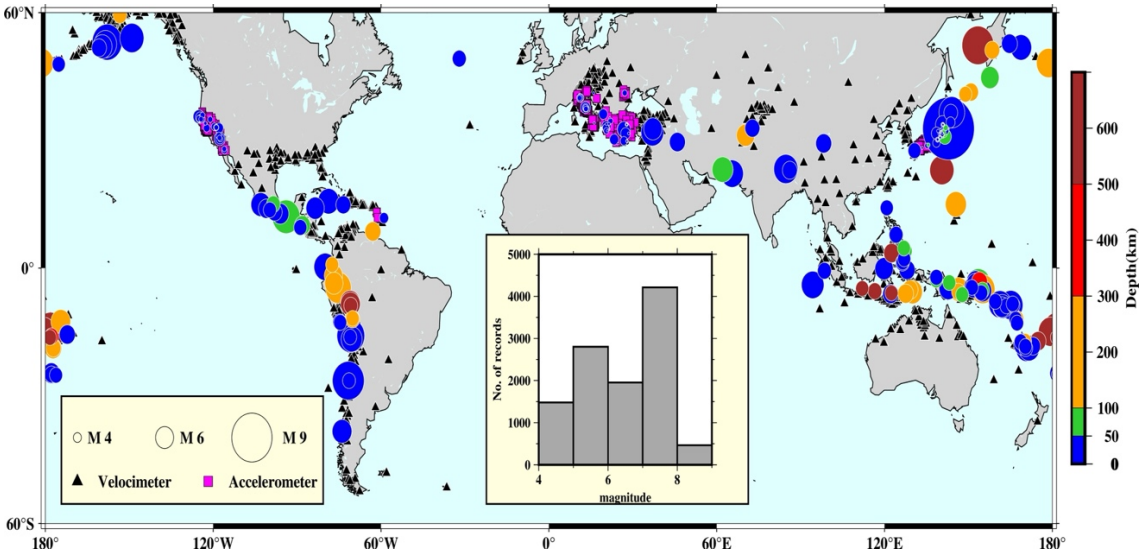


*Figure 5.1.1: Map of the events. The figure shows the epicentral position of the events used in this study (colored circles). The size of the circles is proportional to the earthquake magnitude and the color shows the event depth. Black triangles are the velocimeter sensors while magenta squares represent accelerometer sensors. The histogram in the middle shows the distribution of records in each magnitude bin.*

### 5.1.1 Evaluation of the LPDT curves and their initial slope

We select the records within a 25 km wide circular crown that includes the closest stations to event epicenter. Depending on the available recording sensor (velocimeter or accelerometer) (see Figure 5.1.1) we perform a single or double integration of signal, respectively, to get displacement and we finally apply a high-pass Butterworth filter with cut-off frequency of 0.075Hz to remove possible baseline effects. We compute the logarithm of the peak of the absolute displacement starting from the P-arrival time at the station.

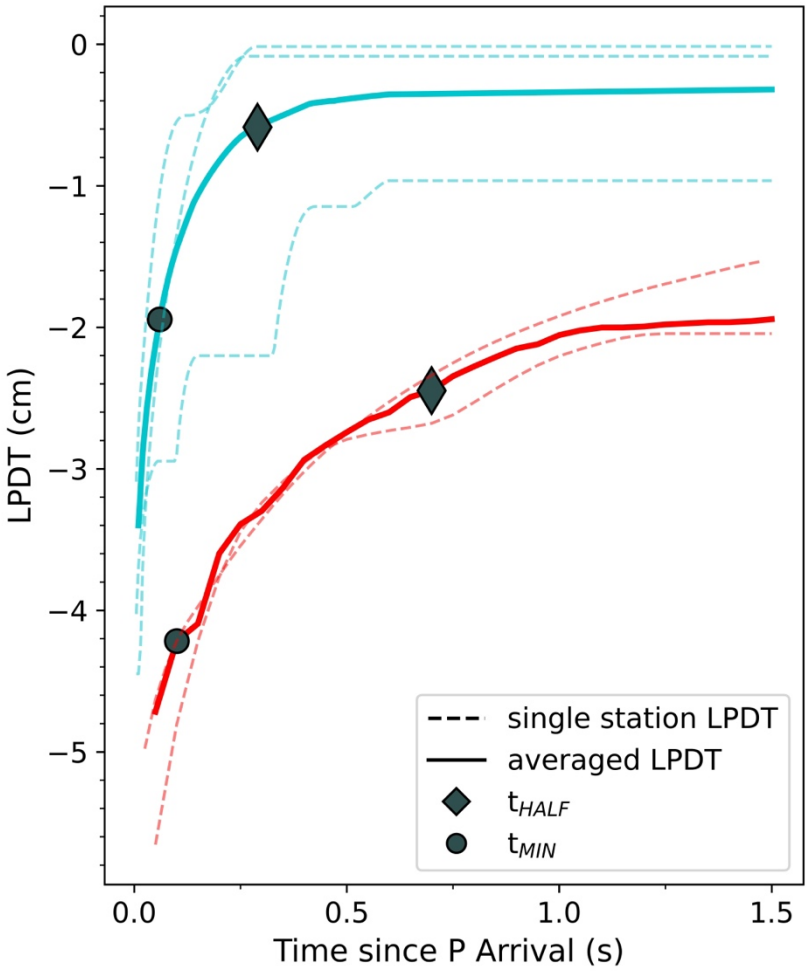


*Figure 5.1.2: Computation of LPDT curves and slope measurement. Color represents two different magnitude values (cyan is Mw=4, red is Mw=7). Dotted lines show the LPDT curves at each station; thick lines show the averaged LPDT curve. The circle (corresponding to $t_{MIN}$=0.05s) is the starting point for the slope evaluation. The diamond ($t_{HALF}$) is the ending point for slope evaluation.*

We average the obtained LPDT curves by stations (dashed lines in Figure 5.1.2). The average is performed at each time step and the starting point of the single station curve corresponds to the P-wave arrival at the station. Finally, we get the final LPDT curve (thick line in Figure 5.1.2) whose points have a standard deviation coming from the average we performed on single station curves. We calculate the initial slope on the averaged LPDT curve in few steps.

The first step is the fit of the observed LPDT curve with an exponential function in the following form:

$$\mathrm{LPDT_{teo}} = \mathrm{LPDT_{end}}\left(1 - \mathrm{e}^{-\mathrm{t}/\mathrm{t_1}}\right) - \mathrm{LPDT_0} \qquad (35)$$

Where $LPDT_0$ and $LPDT_{end}$ are the first and the last point of the curve respectively, $t_l$ is a fit parameter that simply allows the function to bend towards the plateau level. The fitting procedure is used to avoid numerical noise caused by the discontinuity of observed curves. The fitting curve is just used to select the time window for the slope measurement on the observed LPDT curve.

The second step is the curvature evaluation of the $LPDT_{teo}$ as:

$$\text{curvature} = \frac{|y''|}{(1 + (y')^2)^{3/2}} \tag{36}$$

where y' and y'' are the numerical first and second derivative of the interpolated LPDT curve. The curvature is a mathematical tool to quantify how much the curve deviates from a linear behavior. The curvature of the LPDT curve is expected to increase towards a maximum, where the curve bends to the plateau level, and to decrease monotonically towards zero since the plateau level is a straight line. We then recognize the time $t_{HALF}$ on the curvature, corresponding to half of the time where the maximum of the curvature is reached.

Finally, we evaluate the slope along the observed LPDT curve in the time interval between $t_{MIN}$=0.05 s and $t_{HALF}$. The choice of the starting point for the slope evaluation is done to account for errors in affect the manual picking of waveforms. The slope is obtained from the line that crosses the LPDT between $t_{MIN}$ and $t_{HALF}$, using a weighted least-square fit which takes into account the standard deviation on each point of the observed LPDT. The slope can be expressed as it follows:

$$\text{Slope} = \frac{\text{LPDT}(t_{HALF}) - \text{LPDT}(t_{MIN})}{t_{HALF} - t_{MIN}} \tag{37}$$

Throughout data processing and analysis, we aimed at minimizing artificial contaminations that could introduce bias into the results. We keep our method for the early P-wave slope evaluation as simple as possible, avoiding complex signal processing.

One potential source of bias could stem from the high-pass filtering applied to the displacement data. However, we followed the approach outlined by Colombelli et al. (2020), who addressed this issue, demonstrating that the slope calculated from

displacement records derived from unfiltered acceleration and velocity data maintains the scaling trend with magnitude.

Another potential bias could arise from geometric or anelastic attenuation of the radiated wavefield over distance. While Colombelli et al. (2020) showed that slope measurements from LPDT curves are only weakly affected by distance attenuation, for this analysis we selected records from a narrow circular zone (25 km wide) to minimize distance attenuation effects.

Finally, the potential directivity effect is mitigated by averaging LPDT curves distributed azimuthally within the selected circular zone to evaluate the initial slope.

## 5.2 The global scaling of the initial growth of LPDT curves with magnitude

We show that the P-wave signals associated with large earthquakes typically begin with a slow initial amplitude growth in the first few seconds, while the P-wave signals radiated by small events are mainly characterized by a rapid amplitude increase, in a shorter time. When evaluated over a large spectrum of magnitudes and for different tectonic areas worldwide, the early part of the log-displacement vs. time curves measured along the P-wave portion of stations in close-proximity distances (maximum distance difference of 25 km between the closest and the furthest stations from event epicenter) show a clear decreasing linear trend with the earthquake magnitude (Figure 5.2.1 A). The time window in which this estimate is done is also depending on the final earthquake magnitude, with larger time windows being necessary to measure the initial slope for larger magnitude events (Figure 5.2.1 B). Given the variability and uncertainties of measurements, the observed standard error of the linear regressions, suggests an uncertainty of about one magnitude unit associated with the slope measurement obtained by averaging the values at the stations within a very narrow (25 km) circular ring starting from the nearest station to epicenter.

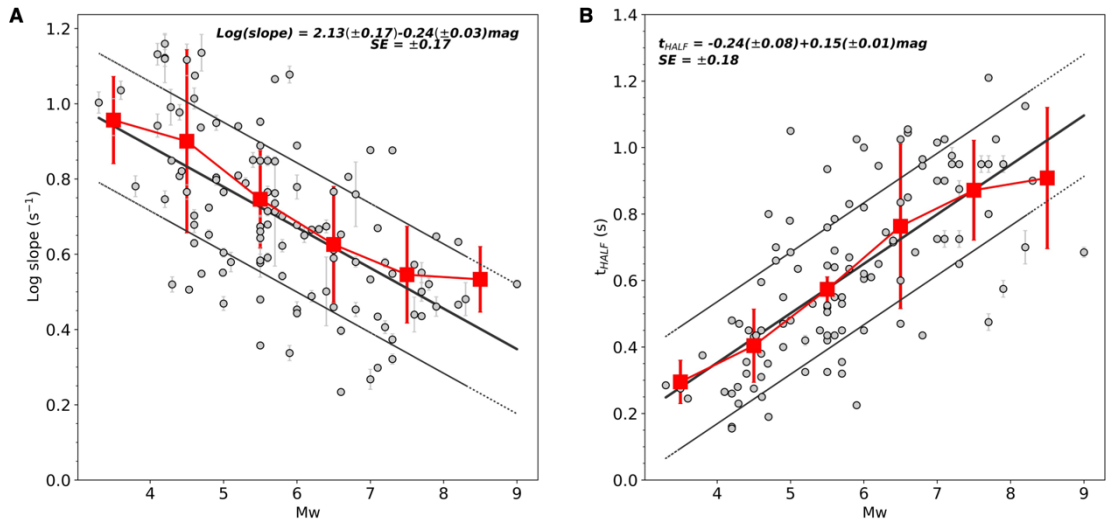


*Figure 5.2.1: Initial Slope pf LPDT curves and related time. (A) initial slope of LPDT curves as a function of magnitude. (B) the time at which LPDT curves reach half of the maximum of their curvature ($t_{HALF}$) as a function of magnitude. In both panels grey dots are single slope and time measurements, while red squares are the average values for each magnitude bin (bin width = 1). The solid black line represents the best fit line, along with ±one-SE thin lines. The fit parameters and the SE values are shown at top left of the panel.*

To assess the statistical relevance of the empirical relationships we show in Figure 5.2.1, we perform a correlation t-test whose results are shown in Table 5-1. Particularly, we find a robust anti-correlation between the logarithm of the slope measures and the moment magnitude while a positive correlation is observed between the characteristic time-window and the moment magnitude. The result is also confirmed by the small p-values.

*Table 5-1: Correlation t-test of slope versus magnitude and of $t_{HALF}$ versus magnitude. r is the Pearson correlation coefficient, t-value is obtained from a two-tailed t-test, p-value represents the significance level of null hypothesis that is "no linear correlation between variables of interest"*

| | **Log (Slope) vs magnitude** | **$t_{HALF}$ vs magnitude** |
|---|---|---|
| **r** | $-0.6$ | 0.7 |
| **t-value** | $-7.6$ | 10.4 |
| **p-value** | $9.6 \cdot 10^{-12}$ | 0.0 |

Figure 5.2.1 shows that for a M = 4 earthquake the average value of the initial growth rate of displacement is about 20 $s^{-1}$, while for a M = 9 the average value is about 2 $s^{-1}$ (panel A). As for the time for slope measurement, we need approximately 0.2 s for M = 4 earthquakes and about 1 s for M = 9 events (panel B).

### 5.2.1 The physical implications for the earthquake nucleation

Having ruled out any possible effect of bias that leads to the results shown in Figure 5.2.1, we argue that the scaling trend of the initial P-wave growth rate (the LPDT initial slope) with magnitude can be explained in terms of the preparatory process of the earthquake rupture. Different authors ((Nielsen et al., 2010),(Latour et al., 2013)) explored the complexity of the preparatory process that evolves in the rupture propagation by performing laboratory experiments. Nielsen et al. (2010) showed that the rupture sequences are composed of an initial phase with nucleation and crack size increasing at a slow stable velocity of about 5% of shear wave velocity. When the crack reaches a critical length related to frictional parameters (e.g. critical slip weakening distance Dc), the rupture accelerates towards subsonic velocity and finally to supershear (Nielsen et al., 2010). The time during which rupture accelerates towards the dynamic propagation is well-known and is strictly related to the final slip (Latour et al., 2013). Within this framework, the observed scaling of both slope and its characteristic time with magnitude could represent the footprint of the unstable acceleration phase that leads to dynamic propagation during the nucleation phase, supporting the hypothesis that earthquakes show a differentiation at the beginning of the rupture process.

The inverse scaling trend of slope with magnitude might be numerically and physically explained by taking into account the effect of variable stress drop and/or rupture velocity in the beginning of the earthquake rupture. A theoretical discussion of this hypothesis is presented in paragraph 1.3.2. We find that both the rupture velocity and the dynamic stress drop control the steepness of the LPDT initial slope. In Figure 5.2.2 we used the Sato & Hirasawa (1973) quasi-dynamic model of a circular rupture at constant stress-drop and uniform rupture velocity to simulate the P-wave displacement recorded at the strong motion network that recorded the Mw 6.5 Central Italy earthquake in 2016. Three different magnitude (M 5,6 and 7) events have been simulated at the 50 stations located within 100 km of epicentral distance. To show the effect of a variable rupture velocity with magnitude, we set Vr=0.9vs for Mw 5, Vr=0.7 Vs for Mw 6 and Vr=0.5 for Mw 7. The larger rupture velocity produces faster initial rise of the displacement waveform for smaller magnitude events that is not observed when rupture velocity is taken constant with magnitude. More complex numerical simulations are necessary to further investigate how these parameters control the scaling of the initial growth rate of displacement that we observe in Figure 5.2.1.

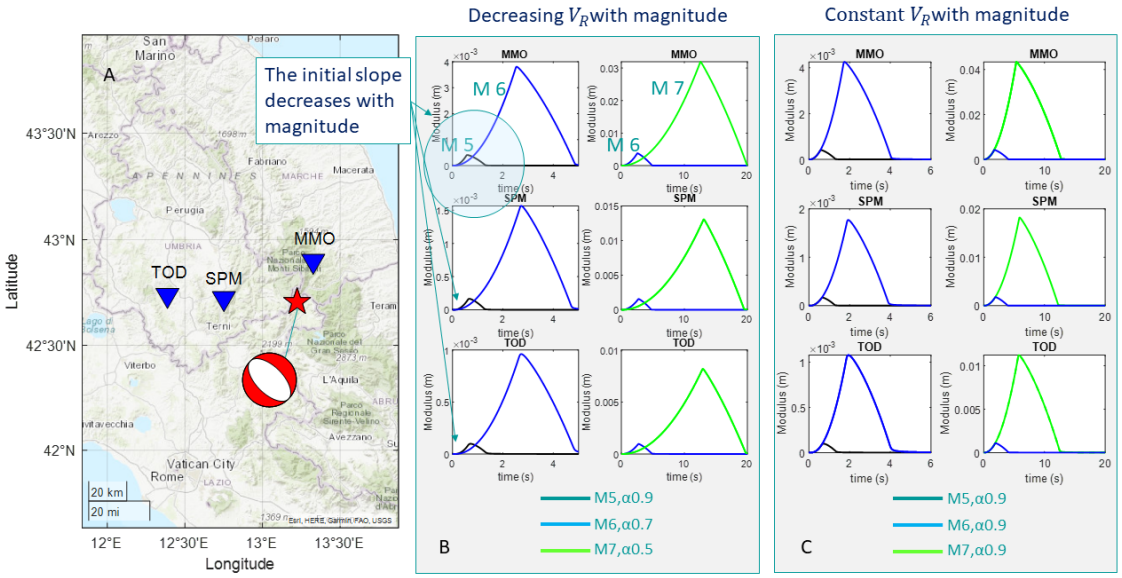


*Figure 5.2.2: Numerical simulations. The figure displays the S&H displacement pulse waveforms simulated at three stations of the network (panel A). The effect on waveforms of variable or constant rupture velocity with magnitude is clearly represented in panels B and C.*

Recently, Nielsen et al. (2024) has provided a detailed discussion about earthquake rupture physics through the finite difference numerical modelling. He has identified a scaling in the acceleration of rupture propagating from an initial crack. He has found that the rupture front tip location scales with the critical length of the crack in space and scales with the ratio between the crack length and the limiting rupture velocity in the subsonic regime in time. Consequently, he has argued that ruptures starting from a larger nucleation area will accelerate more slowly and that large nucleation can only take place on large faults. Within this framework, our results could be the link between the non-radiative part of the rupture process (the nucleation) and the far-field radiation. We argue that the scaling trends shown in Figure 5.2.1 could be purely related to the breakaway phase of the nucleation (as described by Nielsen et al. (2024)), that precedes the fully dynamic propagation. As we showed through preliminary synthetic tests (Figure 5.2.2), the physical parameters that control the amplitude and the rate of the far-field radiation (such as the velocity rupture) might be affected by an existing imprinting between the aseismic loading of the rupture (the nucleation phase) and its radiative phase. Our results confirm that, at least in a probabilistic sense, it is more likely that a small nucleation area will develop into a small earthquake rather than a big earthquake. The latter is more likely to be expected on a larger nucleation area which can break and host a major event. Moreover, the initial growth rate of the far-field displacement might be the footprint left by the non-radiative preparatory process, emerging on the seismic signals.

## 5.3 Future perspectives for earthquake early warning systems

In previous paragraphs we discussed about the principles and the applications of the Earthquake Early Warning Systems. Until now in the scientific literature, there is a fundamental assumption that is somehow implied for EEW: it is assumed that EEWS cannot predict the final earthquake size and can only observe the evolving moment release. This perspective arises from various factors we have illustrated throughout this work: (1) the parameters showing a scaling with the final earthquake size are very sensitive to the processing of data and to the time window of the signal being analyzed (paragraphs 1.2.1 and 1.2.2); as a consequence (2) the empirical scaling laws implemented in EEWS are characterized by a great variability that affects the magnitude estimation and the system performance (since extended time windows are required to get a stable magnitude measurement); most importantly (3) we have shown that the observations are too conflicting to definitively conclude that one model (the preslip or the cascade model described in paragraph 1.4) provides the correct description of the earthquake nucleation compared to the other. In this context, the results shown in paragraph 5.2 might represent a step forward not only in the understanding of the earthquake rupture beginning but also in building EEW approaches. Indeed, the global scaling trend observed between the initial growth rate of displacement and the final magnitude in Figure 5.2.1 could be implemented in future EEWS to get fast magnitude characterization in less than 1 second since the first P-wave detection. The results we showed are obtained in off-line mode, meaning that the initial growth rate of displacement was measured on a very short time window of the whole available P-wave signal on which the development of the displacement could be appreciated (we could build the complete LPDT curves and retrieve their plateau level but we focused on its earliest part instead). Besides the investigation on the earthquake rupture physics, the challenge that the retrieved empirical laws pose for EEW is their application to the real-time monitoring. Moreover, we concluded that the initial growth rate of displacement inversely scales with the final magnitude from an average we performed on a certain number of stations per event (although limited in space). In future applications for EEWS, and particularly for on-site EEWS, there is the need to move towards a single station approach and for this reason we need to explore whether it is feasible to get the fast magnitude characterization using the growth rate of displacement versus magnitude law with a single LPDT curve slope value rather than an average LPDT curve slope measurement. For a step in this direction, the use of AI methods can be greatly effective (Lara et al., 2023); another step

is represented by the next generation of P-wave based earthquake early warning systems (like P-Alert that we discussed in chapter 4) which have the great potential to provide an environment where the new methodology we proposed could be easily implemented. Indeed, these kinds of systems are free from being time window dependent since the P-wave parameters are continuously measured. In paragraph 3.3 of Chapter 3 and in paragraph 4.2 of Chapter 4 we tested two different on-site algorithms on the same region (California) and we showed how the perfomance greatly improves when the system does not depend on a fixed PTW.

The new interpretations of the earthquake rupture we discussed here can pave the way to a whole new chapter of the earthquake physics and consequently of the implementation of the earthquake early warning, improving systems that are working to mitigate the catastrophic effects earthquakes might have on people's lives.

# Conclusions

The work presented in this thesis is divided into three interconnected parts, all centered on the topic of Earthquake Early Warning (EEW). By exploring the physical principles and methodologies of EEW systems, this study has tested these approaches on various seismic catalogs and examined the implications of earthquake rupture physics for EEW.

In **Part One**, an overview of the physical foundations of EEW is provided, focusing on early P-wave parameters and their relationship with the nucleation phase of earthquake rupture. **Part Two** discusses the methodologies and applications of two on-site EEW systems, SAVE and P-Alert, highlighting their respective performance. Finally, **Part Three** addresses earthquake rupture physics, emphasizing its significance for the future development of EEW systems.

The core contribution of this work lies in the extensive application of on-site EEW algorithms to a wide range of datasets from different tectonic environments, including the volcanic setting of the Campi Flegrei Caldera. This comprehensive analysis has facilitated a discussion on the performance of these systems, bringing to light their strengths and weaknesses. For instance, SAVE has demonstrated flexibility and ease of integration with existing network systems. However, its reliance on a fixed P-wave time window has highlighted limitations in its performance, underscoring the need for the next generation of P-wave-based on-site systems.

Building on this, P-Alert was tested, for the first time since its conception in 2015, on a large Californian dataset. The results confirmed the significant potential of this system, which continuously measures early P-wave parameters and offers improved resolution in parameter estimation. P-alert overcomes the limitations of SAVE since it naturally considers an expanded P-wave time window, so to manage the possible occurrence of small and large earthquakes, and it bases the alert on the exceedance of a threshold in the predicted impact (PGV). The focus on on-site P-wave-based EEW systems has also provided a unique opportunity to investigate earthquake rupture behavior by analyzing the earliest portion of the radiated P-wave signals. Among the most noteworthy findings is the global scaling relationship between the initial growth rate of early P-wave displacement and the final earthquake magnitude. This result is confirmed and verified by a massive battery of tests for check-validation. This scaling, observed within an exceptionally short P-time window (less than one second), has two major implications:

- The growth rate of displacement may offer insights into the nucleation phase, possibly reflecting the footprint of the non-radiative processes that precede dynamic rupture propagation.

- The empirical scaling relationship could be applied to rapidly characterize earthquake size in future EEW systems.

Further research is needed to explore the connection between the growth rate of displacement and physical parameters governing earthquake rupture, such as rupture velocity and stress drop.

This PhD thesis integrates different research topics, all linked to the central theme of Earthquake Early Warning. The work presented here offers a foundation for advancing existing methodologies and deepening our understanding of earthquake rupture physics.

# APPENDIX A – A Python package for on-site earthquake early warning

## A.1 Python package for SAVE off-line and real-time testing

For the development of the Python version of SAVE, the decision was made to follow the original scheme for on-site Early Warning proposed by Caruso et al. (2017), which was previously implemented in C++. This new Python version of the algorithm is designed to be user-friendly and includes additional features, such as:

- Dual usage modes, for both offline testing on data and real-time applications;
- The ability to adjust thresholds used by SAVE from an external text file: users can modify data quality control thresholds by editing specific lines in the provided text file, which the code automatically reads and updates.

For offline data analyses, users can choose whether to test the algorithm with manual picks or with automatic filter picks.

### A.1.1 Code architecture

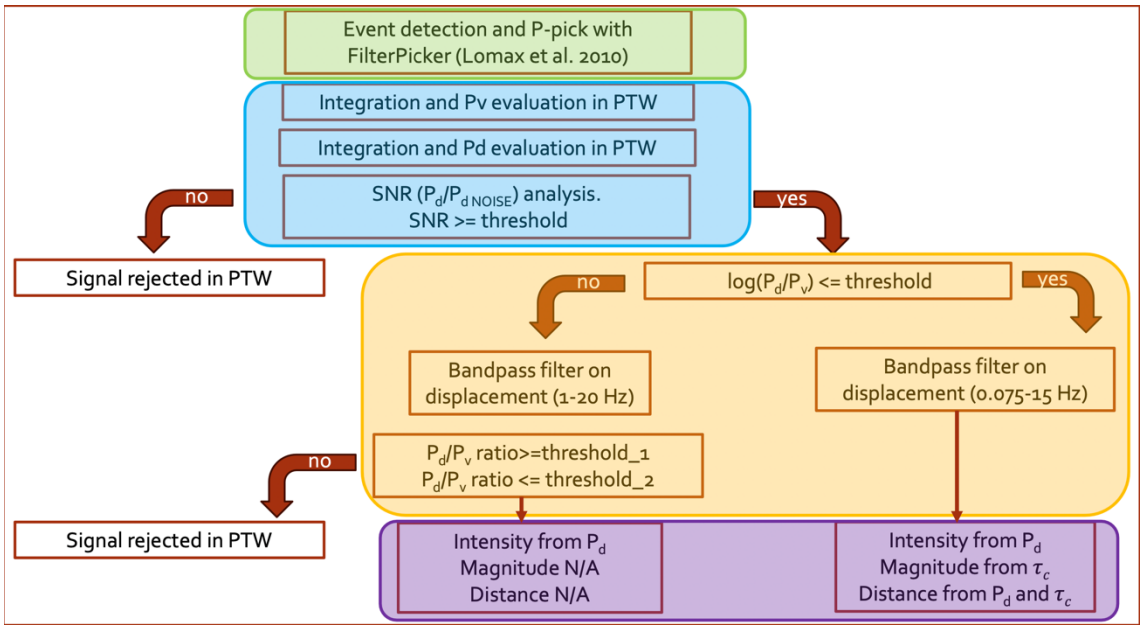


*Figure A.1.1: Block diagram of SAVE python code. The four modules are highlighted with different colored boxes: in green box the picker module; in blue the integration and first quality control module; in orange the second quality control and filter selection module; in violet the output parameters estimation module.*

Figure A.1.1 shows the block diagram of the SAVE software developed in Python. The main modules are as follows:

- **Picking module (in green):** Detects and extracts the P-wave arrival time from the station's vertical component.

- **Data integration and first quality control module (in blue):** Integrates the acceleration data to obtain velocity and displacement, calculates the signal-to-noise ratio, and compares it to a user-defined threshold.

- **Second quality control and filter selection module (in orange):** Analyzes the quality of the peak velocity-to-peak displacement ratio within a user-defined tolerance range and applies a displacement filter.

- **Intensity, magnitude, and distance estimation module (in violet):** This final module depends on the previous module, especially on the automatic filter selection. Depending on the selected filter, the system provides an intensity estimate, a magnitude and distance range (for high-quality data), or only an intensity estimate (for low-quality data).

## A.1.2 Code modules

Below is a detailed description of each software module, specifying: Module objective; Algorithm description; Produced outputs.

1. **Automatic Picker**

**Module Objective:** Recognize the arrival time of the seismic P-phase when an event occurs by analyzing the station's vertical (Z) component.

**Algorithm Description:** Starting from the waveform, a Characteristic Function (CF) is calculated. This function peaks when the signal's amplitude, measured within a short time window, is high compared to the characteristic amplitude measured within a longer window (background noise). The waveform is filtered across multiple frequency bands, each producing a CF. A seismic P-phase arrival is declared at time $t_{pick}$ when the CF in any frequency band exceeds a minimum threshold, and the CF's average value subsequently remains above a second threshold for a sufficient period.

**Output:** Arrival times of one or more possible seismic phases if detected in the input waveform. No output otherwise.

### 2. Data Integration and Signal-to-Noise Ratio (SNR)

**Module Objective:** Assess the quality of the displacement signal in the examined window by analyzing the signal-to-noise ratio.

**Algorithm Description:** From the input signal, a first numerical integration of the waveform is performed to obtain velocity. In the analyzed window starting from the recognized seismic phase's arrival time, zero-crossing is applied, and the absolute peak velocity ($P_v$) is calculated. A second numerical integration then provides displacement. Zero-crossing is again applied, and the absolute peak displacement ($P_d$) is calculated. A 2-second signal window is then isolated, starting at $t_{pick}-3$ seconds, to measure background noise ($P_d^{NOISE}$). The SNR in decibels is calculated as $P_d$/ $P_d^{NOISE}$ and is verified to be above a user-adjustable threshold.

**Output:** Displacement waveform in the examined window, $P_v$ and $P_d$ if the SNR is adequate. No output otherwise.

### 3. $P_d/P_v$ Ratio and Automatic Displacement Filter Selection

**Module Objective:** Filter displacement data based on the logarithmic Pd/Pv ratio within the examined window, providing necessary parameters for intensity, magnitude, and distance calculations.

**Algorithm Description:** Using the $P_d$ and $P_v$ values from the previous module, the logarithmic ratio is calculated. If this is below a user-defined threshold, a 0.075–15 Hz bandpass filter is applied to displacement, the peak displacement Pd and the characteristic period τc are calculated. If the condition is unmet, a 1–20 Hz bandpass filter is applied for a second check on the ratio. If it falls within a tolerance range ($threshold_1$ and $threshold_2$), Pd is accepted; otherwise, the signal is rejected.

**Output:** Pd and τc if the 0.075–15 Hz bandpass filter is applied. Pd if the 1–20 Hz bandpass filter is used.

4. **Intensity, Magnitude, and Distance Estimation**

**Module Objective:** Estimate macroscopic intensity, expected magnitude range, and event distance.

**Algorithm Description:** The algorithm uses Pd and, if available, τc. Based on the window duration (1, 2, or 3 seconds) from P-phase detection, the logarithmic Pd is used in corresponding formulas to estimate the maximum expected site velocity (PGV). This is converted into expected macroscopic intensity via Faenza & Michelini (2010) scaling laws. If τc is also available, its logarithm is used to estimate magnitude, and the combination of τc and Pd logarithms provides a distance estimate.

**Output:** Macroscopic intensity value, expected magnitude and distance range. If data quality is low, only macroscopic intensity is provided.

## A.1.3 Input parameters

User-adjustable input parameters are modifiable in two text files. The first configures the automatic picker, and the second configures the thresholds the SAVE algorithm depends on for data quality control.

**filterpicker_config.txt Text File** In this file, user-adjustable parameters follow the FilterPicker nomenclature (Lomax et al., 2012): Filter window (in seconds), Long Term Window (in seconds), Threshold 1, Threshold 2, tUP Event (in seconds).

```
FILTER PICKER SETTING FOR SAVE (follows the scheme by Lomax et al. 2012)
WARNING: please only modify parameter of interest in the corrispondig line. Do not add or remove any lines.

Filter window (in seconds)
1

Long Term Window (in seconds)
12.0

Threshold 1
10

Threshold 2
10

tUP Event (in seconds)
1
```

*Figure A.1.2: Example of file text for picker setting of SAVE python package*

**param_config.txt Text File** This file allows users to adjust values for key parameters used in both offline and real-time versions of SAVE, including: SNR threshold; Log(Pd/Pv) threshold for high-quality data control; Upper threshold for low-quality data control; Lower threshold for low-quality data control; Maximum window duration after P-phase detection (1–3 seconds required).

```
PARAMTERS SETTING FOR SAVE
WARNING: please only modify parameter of interest in the corrispondig line. Do not add or remove any line.

SNR THRESHOLD
8

Log(Pd/Pv) HIGH QUALITY THRESHOLD
-0.2

Log(Pd/Pv) LOW QUALITY UPPER BOUND THRESHOLD
-0.9

Log(Pd/Pv) LOW QUALITY LOWER BOUND THRESHOLD
-1.8

P-TIME WINDOW (MIN 1 - MAX 3 SECONDS)
3

OFFLINE PERFORMANCE PICKS (Automatic/Manual)
Manual
```

*Figure A.1.3: Example of file text for thresholds setting of SAVE python package in off-line mode*

In offline mode, the last line allows users to choose between using automatic or manual picks (figure A.1.3)

```
PARAMTERS SETTING FOR SAVE
WARNING: please only modify parameter of interest in the corrispondig line. Do not add or remove any lines.

SNR THRESHOLD
14

Log(Pd/Pv) HIGH QUALITY THRESHOLD
-0.2

Log(Pd/Pv) LOW QUALITY UPPER BOUND THRESHOLD
-0.9

Log(Pd/Pv) LOW QUALITY LOWER BOUND THRESHOLD
-1.8

P-TIME WINDOW (MIN 1 - MAX 3 SECONDS)
3

SENSOR OF THE STATION (user3 value for ISNET stations)
0.509

LOGGER OF THE STATION (user2 value for ISNET stations)
5.36e-07
```

*Figure A.1.4: Example of file text for thresholds setting of SAVE python package in real-time mode*

In real-time mode, the last two lines include Sensor and Logger information for unit conversion.

## A.1.4 Output parameters

Output parameters can be read from automatically generated text files.

**Offline Version:** Output parameters are in files named SAVE_offline_0N_second.txt, with N from 1 to 3. Each file includes: STA (station code), PICKING_TIME (absolute pick time), INTENSITY (macroscopic intensity), MAG_RANGE (predicted magnitude range), MAG_VALUE (estimated magnitude), DISTANCE_RANGE (predicted distance range), DISTANCE_VALUE (estimated distance in km), SNR (SNR in the examined window), LOG_PD_PV (logarithmic Pd/Pv value), MODE (data quality: H = high, L = low, R = rejected), Pd (P-phase peak displacement in cm), Tc (P-phase characteristic period in seconds), PTW (examined window length in seconds) (in Figure A.1.5)

```
STA PICKING_TIME INTENSITY MAG_RANGE MAG_VALUE DISTANCE_RANGE DISTANCE_VALUE SNR LOG_PV_PD MODE Pd(cm) tc(s) PTW(s)
VDS3 2023-05-14T07:28:48.803354Z 3.0196461160504664 MEDIUM 3.11 NEAR 26.036 22.006638245598275 -1.4055457594573422 H 0.00124686289512 0.251 1.0
```

*Figure A.1.5: Example of file text for output parameters of SAVE python package in off-line mode*

**Real-time Version:** Parameters are in SAVE_INFO_ALERT.txt. The first three lines detail network, station, and component information, with the absolute P-phase pick time. Following lines include parameter estimates for each window, intensity, magnitude range, distance range, and data quality estimates. (Figure A.1.6)

```
============ SAVE ALERT PARAMETERS =============
NETWORK IX STATION VDS3 CHANNEL HNZ
UTC PICKING TIME 2023-05-14T07:28:48.803354Z

== SAVE PARAMETERS ESTIMATES IN 1.0 SECONDS SINCE P-ARRIVAL ==
INTENSITY: 3.02 MAGNITUDE: MEDIUM DISTANCE: NEAR
Mode: H SNR: 22.00 Log_Pd_Pv: -1.40 Pd(cm): 0.0012 tc(s): 0.251 M: 3.11 R(km): 26.036


== SAVE PARAMETERS ESTIMATES IN 2.0 SECONDS SINCE P-ARRIVAL ==
INTENSITY: 3.24 MAGNITUDE: SMALL DISTANCE: NEAR
Mode: H SNR: 24.21 Log_Pd_Pv: -1.54 Pd(cm): 0.0016 tc(s): 0.221 M: 2.93 R(km): 21.917


== SAVE PARAMETERS ESTIMATES IN 3.0 SECONDS SINCE P-ARRIVAL ==
INTENSITY: 3.29 MAGNITUDE: MEDIUM  DISTANCE: NEAR
Mode: H SNR: 27.12 Log_Pd_Pv: -1.43 Pd(cm): 0.0022 tc(s): 0.255 M: 3.03 R(km): 23.508
```

*Figure A.1.6: Example of file text for output parameters of SAVE python package in real-time mode*

## A.2 Example tests on two Irpinia earthquakes

In the following paragraphs, we provide two examples of offline performance of SAVE. We tested the algorithm on the two main events of the seismic sequences recorded and monitored by the ISNET network, which began on May 14, 2023, and May 29, 2023, with epicenters located in Capo di Giano (PZ) and Laviano (SA), respectively.

### A.2.1 Off-line test on event at Capo Di Giano (PZ), Italy

The main event of May 14th, 2023 seismic sequence was located by the ISNET network in Capo di Giano (PZ). Table A-1 provides information on location and magnitude (more information available at http://isnet-bulletin.fisica.unina.it/cgi-bin/isnet-events/isnet.cgi).

*Table A-1: Source parameters for the main event of the Capo di Giano (PZ) sequence on May 14, 2023*

| LAT | LON | DEPTH (KM) | MW |
|---|---|---|---|
| **40.763** | **15.487** | **6.6** | **2.8** |

For this event, we provide an offline test of the SAVE procedure at the station closest to the epicenter, VDS3. The epicentral distance estimated by ISNET is 8.3 km. The test was performed using the automatic picker FilterPicker. Table A-2 provides the selected parameters for the picker, and the figure (reference) shows the result of the application. The P-wave arrival is accurately estimated and consistent with manual picking. The figure is automatically generated by the automatic picker.

*Table A-2 - Parameters chosen for FilterPicker settings*

| | |
|---|---|
| Filter window (s) | 1 |
| Long Term Window (s) | 12 |
| Threshold 1 | 10 |
| Thresshold 2 | 10 |
| tUP Event | 1 |

The thresholds used by the SAVE algorithm are described in Table A-3. The output information obtained using a maximum window of 3 seconds from the automatically recognized P arrival is provided in Table A-4.

*Table A-3 - Parameters chosen for SAVE settings*

| | |
|---|---|
| SNR THRESHOLD | 8 |
| Log(Pd/Pv) High quality threshold | -0.2 |
| Log(Pd/Pv) Low quality upper bound threshold | -0.9 |
| Log(Pd/Pv) Low quality lower bound threshold | -1.8 |

| | |
|---|---|
| P-Time window (s) | 3 |
| Offline performance picks | Automatic |

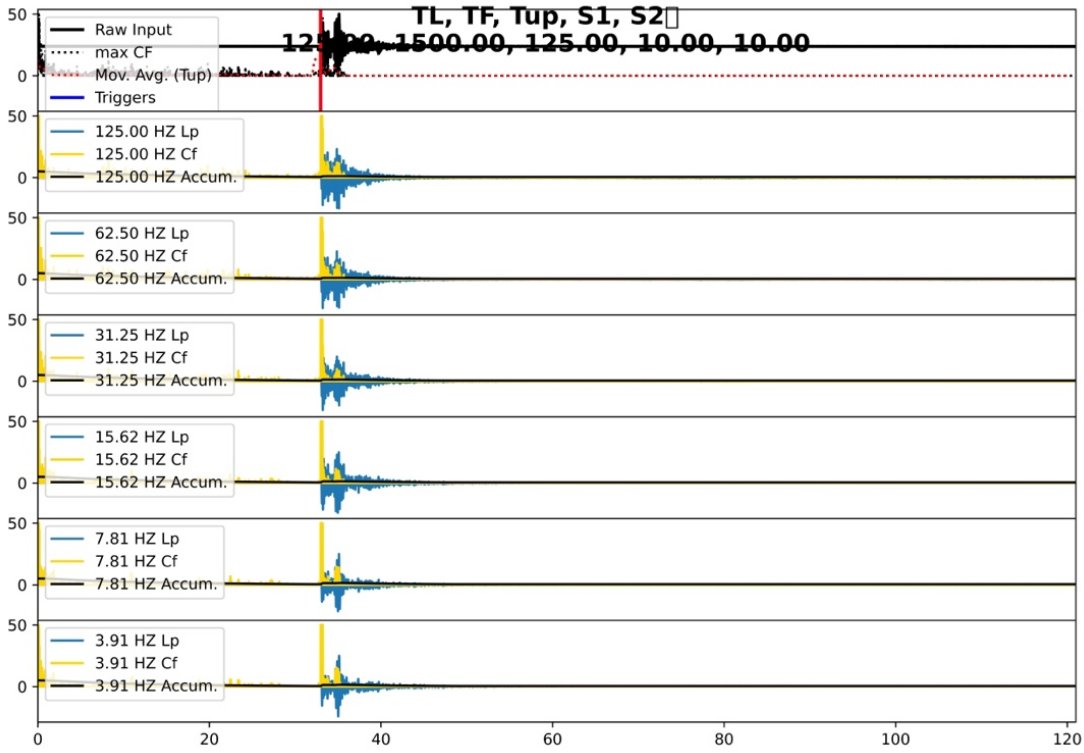


*Figure A.2.1: Automatic pick on the vertical component of VDS3 station for the event of Capo di Giano (PZ)*

*Table A-4 - Output parameters obtained from the offline test of SAVE on the Capo di Giano (PZ) event*

| STA | Picking time | Intensity | Mag Range | Mag Value | Dist Range | Dist Value(km) | SNR | Log(Pd/Pv) | Mode | Pd(cm) | Tc(s) | PTW(s) |
|---|---|---|---|---|---|---|---|---|---|---|---|---|
| **VDS** | 2023-05-14T07:28:48.774002 | 3.02 | MEDIUM | 3.11 | NEAR | 25.955 | 21.61 | -1.40 | H | 0.0012 | 0.25 | 1 |
| **VDS** | 2023-05-14T07:28:48.774002 | 3.24 | MEDIUM | 3.03 | NEAR | 23.004 | 23.81 | -1.54 | H | 0.0016 | 0.236 | 2 |
| **VDS** | 2023-05-14T07:28:48.774002 | 3.29 | MEDIUM | 3.03 | NEAR | 23.505 | 26.72 | -1.43 | H | 0.0022 | 0.255 | 3 |

## A.2.2 Off-line test on event at Laviano (SA), Italy

The main event of the sequence that began on May 29, 2023, was located by the ISNET network in Laviano (SA). Table A-5 provides information on location and magnitude. For this event, we conducted an offline test of SAVE at the station closest to the epicenter, VDS3, with an epicentral distance of 12.5 km. The offline test used the automatic picker, whose settings are described in Table 2. The thresholds on which SAVE operates are

described in Table 4. Table A-6 shows the information obtained within a maximum window of 3 seconds from the detection of the P arrival.

*Table A-1: Source parameters for the main event of the Laviano (SA) sequence on May 29, 2023*

| LAT | LON | DEPTH (KM) | MW |
|---|---|---|---|
| **40.782** | **15.327** | **8.8** | **2.9** |

*Table A-6 - Output parameters obtained from the offline test of SAVE on the Laviano (SA) event*

| STA | Picking time | Intensity | Mag Range | Mag Value | Dist Range | Dist Value(km) | SNR | Log(Pd/Pv) | Mode | Pd(cm) | Tc(s) | PTW(s) |
|---|---|---|---|---|---|---|---|---|---|---|---|---|
| **VDS3** | 2023-05-29T16:55:28.047001 | 2.22 | MEDIUM | 3.23 | NEAR | 36.792 | 14.99 | -1.31 | H | 0.0049 | 0.271 | 1 |
| **VDS3** | 2023-05-29T16:55:28.047001 | 2.22 | MEDIUM | 3.07 | NEAR | 34.062 | 14.99 | -1.31 | H | 0.0049 | 0.244 | 2 |
| **VDS3** | 2023-05-29T16:55:28.047001 | 1.98 | MEDIUM | 3.1 | NEAR | 40.137 | 14.99 | -1.31 | H | 0.00049 | 0.267 | 3 |

# References


Aki, Keiiti., and P. G. . Richards, 2009, Quantitative seismology, University Science Books.

Allen, R. M., and H. Kanamori, 2003, The Potential for Earthquake Early Warning in Southern California, Science (1979), 300, no. 5620, 786–789, doi: 10.1126/science.1080912.

Aranda, J. M. E., A. Jimenez, G. Ibarrola, F. Alcantar, A. Aguilar, M. Inostroza, and S. Maldonado, 1995, Mexico City Seismic Alert System, Seismological Research Letters, 66, no. 6, 42–53, doi: 10.1785/gssrl.66.6.42.

Beroza, G. C., and W. L. Ellsworth, 1996, Properties of the seismic nucleation phase, Tectonophysics, 261, nos. 1–3, 209–227, doi: 10.1016/0040-1951(96)00067-4.

Bevilacqua, A. et al., 2022, Data analysis of the unsteadily accelerating GPS and seismic records at Campi Flegrei caldera from 2000 to 2020, Sci Rep, 12, no. 1, 19175, doi: 10.1038/s41598-022-23628-5.

Bilal, M., and A. Askan, 2014, Relationships between Felt Intensity and Recorded Ground-Motion Parameters for Turkey, Bulletin of the Seismological Society of America, 104, no. 1, 484–496, doi: 10.1785/0120130093.

Boatwright, J., 1980, A spectral theory for circular seismic sources; simple estimates of source dimension, dynamic stress drop, and radiated seismic energy., Bulletin of the Seismological Society of America.

Boore, D. M., and G. M. Atkinson, 2008, Ground-Motion Prediction Equations for the Average Horizontal Component of PGA, PGV, and 5%-Damped PSA at Spectral Periods between 0.01 *s* and 10.0 *s*, Earthquake Spectra, 24, no. 1, 99–138, doi: 10.1193/1.2830434.

Böse, M., D. E. Smith, C. Felizardo, M.-A. Meier, T. H. Heaton, and J. F. Clinton, 2018, FinDer v.2: Improved real-time ground-motion predictions for M2–M9 with seismic finite-source characterization, Geophys J Int, 212, no. 1, 725–742, doi: 10.1093/gji/ggx430.

Campillo, M., and I. R. Ionescu, 1997, Initiation of antiplane shear instability under slip dependent friction, J Geophys Res Solid Earth, 102, no. B9, 20363–20371, doi: 10.1029/97JB01508.

Caruso, A., S. Colombelli, L. Elia, M. Picozzi, and A. Zollo, 2017, An on-site alert level early warning system for Italy, J Geophys Res Solid Earth, 122, no. 3, 2106–2118, doi: 10.1002/2016JB013403.

Castello, B., M. Olivieri, and G. Selvaggi, 2007, Local and Duration Magnitude Determination for the Italian Earthquake Catalog, 1981-2002, Bulletin of the Seismological Society of America, 97, no. 1B, 128–139, doi: 10.1785/0120050258.

Chung, A. I., I. Henson, and R. M. Allen, 2019, Optimizing earthquake early warning performance: ElarmS-3, Seismological Research Letters, 90, no. 2 A, 727–743, doi: 10.1785/0220180192.

Clayton, J., B. Derico, and A. Foster, 2023, Google alert failed to warn people of Turkey earthquake, BBC.

Clinton, J., A. Zollo, A. Marmureanu, C. Zulfikar, and S. Parolai, 2016, State-of-the art and future of earthquake early warning in the European region, Bulletin of Earthquake Engineering, 14, no. 9, 2441–2458, doi: 10.1007/s10518-016-9922-7.

Cochran, E. S., J. Bunn, S. E. Minson, A. S. Baltay, D. L. Kilb, Y. Kodera, and M. Hoshiba, 2019, Event detection performance of the PLUM earthquake early warning algorithm in southern California, Bulletin of the Seismological Society of America, 109, no. 4, 1524–1541, doi: 10.1785/0120180326.

Cochran, E. S., and A. L. Husker, 2019, How low should we go when warning for earthquakes?, Science (1979), 366, no. 6468, 957–958, doi: 10.1126/science.aaz6601.
Colombelli, S., A. Caruso, A. Zollo, G. Festa, and H. Kanamori, 2015, A *P* wave-based, on-site method for earthquake early warning, Geophys Res Lett, 42, no. 5, 1390–1398, doi: 10.1002/2014GL063002.
Colombelli, S., G. Festa, and A. Zollo, 2020, Early rupture signals predict the final earthquake size, Geophys J Int, 223, no. 1, 692–706, doi: 10.1093/gji/ggaa343.
Colombelli, S., and A. Zollo, 2015, Fast determination of earthquake magnitude and fault extent from real-time *P* -wave recordings, Geophys J Int, 202, no. 2, 1158–1163, doi: 10.1093/gji/ggv217.
Colombelli, S., A. Zollo, G. Festa, and H. Kanamori, 2012, Early magnitude and potential damage zone estimates for the great Mw 9 Tohoku-Oki earthquake, Geophys Res Lett, 39, no. 22, doi: 10.1029/2012GL053923.
Colombelli, S., A. Zollo, G. Festa, and M. Picozzi, 2014, Evidence for a difference in rupture initiation between small and large earthquakes, Nat Commun, 5, doi: 10.1038/ncomms4958.
Cooper, J. D., 1868, Earthquake indicator, San Francisco.
Cua, G., and T. Heaton, 2007, The Virtual Seismologist (VS) Method: a Bayesian Approach to Earthquake Early Warning, in *Earthquake Early Warning Systems*, Springer Berlin Heidelberg, Berlin, Heidelberg, 97–132.
Dahlen, F. A., 1974, On the ratio of *P* -wave to *S* -wave corner frequencies for shallow earthquake sources, Bulletin of the Seismological Society of America, 64, no. 4, 1159–1180, doi: 10.1785/BSSA0640041159.
Dieterich, J. H., 1979, Modeling of rock friction: 1. Experimental results and constitutive equations, J Geophys Res Solid Earth, 84, no. B5, 2161–2168, doi: 10.1029/JB084iB05p02161.
Douglas, J., 2018, Ground motion prediction equations 1964–2018, University of Strathclyde.
Ellsworth, W. L., and G. C. Beroza, 1995, Seismic Evidence for an Earthquake Nucleation Phase, Science (1979), 268, no. 5212, 851–855, doi: 10.1126/science.268.5212.851.
Erdik, M., Y. Fahjan, O. Ozel, H. Alcik, A. Mert, and M. Gul, 2003, Istanbul Earthquake Rapid Response and the Early Warning System., Bulletin of Earthquake Engineering, 1, no. 1, 157–163, doi: 10.1023/A:1024813612271.
Faenza, L., and A. Michelini, 2010, Regression analysis of MCS intensity and ground motion parameters in Italy and its application in ShakeMap, Geophys J Int, 180, no. 3, 1138–1152, doi: 10.1111/j.1365-246X.2009.04467.x.
Del Gaudio, C., I. Aquino, G. P. Ricciardi, C. Ricco, and R. Scandone, 2010, Unrest episodes at Campi Flegrei: A reconstruction of vertical ground movements during 1905–2009, Journal of Volcanology and Geothermal Research, 195, no. 1, 48–56, doi: 10.1016/j.jvolgeores.2010.05.014.
Hoshiba, M., 2013, Real-time prediction of ground motion by Kirchhoff-Fresnel boundary integral equation method: Extended front detection method for Earthquake Early Warning, J Geophys Res Solid Earth, 118, no. 3, 1038–1050, doi: 10.1002/jgrb.50119.
Hsu, T. Y., P. Y. Lin, H. H. Wang, H. W. Chiang, Y. W. Chang, C. H. Kuo, C. M. Lin, and K. L. Wen, 2018, Comparing the Performance of the NEEWS Earthquake Early Warning System Against the CWB System During the 6 February 2018 $M_w$ 6.2 Hualien Earthquake, Geophys Res Lett, 45, no. 12, 6001–6007, doi: 10.1029/2018GL078079.

Iervolino, I. et al., 2024, Seismic risk mitigation at Campi Flegrei in volcanic unrest, Nat Commun, 15, no. 1, 10474, doi: 10.1038/s41467-024-55023-1.
Kanamori, H., 2005, Real-time seismology and earthquake damage mitigation, Annu Rev Earth Planet Sci, 33, 195–214, doi: 10.1146/annurev.earth.33.092203.122626.
Kanamori, H., 1977, The energy release in great earthquakes, J Geophys Res, 82, no. 20, 2981–2987, doi: 10.1029/JB082i020p02981.
Kodera, Y., Y. Yamada, K. Hirano, K. Tamaribuchi, S. Adachi, N. Hayashimoto, M. Morimoto, M. Nakamura, and M. Hoshiba, 2018a, The Propagation of Local Undamped Motion (PLUM) Method: A Simple and Robust Seismic Wavefield Estimation Approach for Earthquake Early Warning, Bulletin of the Seismological Society of America, 108, no. 2, 983–1003, doi: 10.1785/0120170085.
Kodera, Y., Y. Yamada, K. Hirano, K. Tamaribuchi, S. Adachi, N. Hayashimoto, M. Morimoto, M. Nakamura, and M. Hoshiba, 2018b, The propagation of local undamped motion (PLUM) method: A simple and robust seismic wavefield estimation approach for earthquake early warning, Bulletin of the Seismological Society of America, 108, no. 2, 983–1003, doi: 10.1785/0120170085.
Kohler, M. D., D. E. Smith, J. Andrews, A. I. Chung, R. Hartog, I. Henson, D. D. Given, R. de Groot, and S. Guiwits, 2020, Earthquake early warning Shakealert 2.0: Public rollout, Seismological Research Letters, 91, no. 3, 1763–1775, doi: 10.1785/0220190245.
Kong, Q., R. M. Allen, L. Schreier, and Y.-W. Kwon, 2016, MyShake: A smartphone seismic network for earthquake early warning and beyond, Sci Adv, 2, no. 2, doi: 10.1126/sciadv.1501055.
Kostrov, B. V., 1964, Selfsimilar problems of propagation of shear cracks, Journal of Applied Mathematics and Mechanics, 28, no. 5, 1077–1087, doi: 10.1016/0021-8928(64)90010-3.
Lancieri, M., and A. Zollo, 2008, A Bayesian approach to the real-time estimation of magnitude from the early *P* and *S* wave displacement peaks, J Geophys Res Solid Earth, 113, no. B12, doi: 10.1029/2007JB005386.
De Landro, G., V. Serlenga, G. Russo, O. Amoroso, G. Festa, P. P. Bruno, M. Gresse, J. Vandemeulebrouck, and A. Zollo, 2017, 3D ultra-high resolution seismic imaging of shallow Solfatara crater in Campi Flegrei (Italy): New insights on deep hydrothermal fluid circulation processes, Sci Rep, 7, no. 1, 3412, doi: 10.1038/s41598-017-03604-0.
Lara, P., Q. Bletery, J. Ampuero, A. Inza, and H. Tavera, 2023, Earthquake Early Warning Starting From 3 s of Records on a Single Station With Machine Learning, J Geophys Res Solid Earth, 128, no. 11, doi: 10.1029/2023JB026575.
Latour, S., A. Schubnel, S. Nielsen, R. Madariaga, and S. Vinciguerra, 2013, Characterization of nucleation during laboratory earthquakes, Geophys Res Lett, 40, no. 19, 5064–5069, doi: 10.1002/grl.50974.
Liu, M., and K. Liu, 2024, Overview of China high-speed railway earthquake early-warning system, High-speed Railway, 2, no. 4, 274–282, doi: 10.1016/j.hspr.2024.10.001.
Lomax, A., C. Satriano, and M. Vassallo, 2012, Automatic picker developments and optimization: Filterpicker-A robust, broadband picker for real-time seismic monitoring and earthquake early warning, Seismological Research Letters, 83, no. 3, 531–540, doi: 10.1785/gssrl.83.3.531.
Marcou, S., R. M. Allen, N. A. Abrahamson, and C.-H. Sung, 2024, Ground-Motion Modeling Using MyShake Smartphone Peak Acceleration Data, Bulletin of the Seismological Society of America, doi: 10.1785/0120240209.

Meier, M.-A., J. P. Ampuero, and T. H. Heaton, 2017, The hidden simplicity of subduction megathrust earthquakes, Science (1979), 357, no. 6357, 1277–1281, doi: 10.1126/science.aan5643.
Meier, M., T. Heaton, and J. Clinton, 2016, Evidence for universal earthquake rupture initiation behavior, Geophys Res Lett, 43, no. 15, 7991–7996, doi: 10.1002/2016GL070081.
Meier, M. A., Y. Kodera, M. Böse, A. Chung, M. Hoshiba, E. Cochran, S. Minson, E. Hauksson, and T. Heaton, 2020, How Often Can Earthquake Early Warning Systems Alert Sites With High-Intensity Ground Motion?, J Geophys Res Solid Earth, 125, no. 2, doi: 10.1029/2019JB017718.
Meier, M., Z. E. Ross, A. Ramachandran, A. Balakrishna, S. Nair, P. Kundzicz, Z. Li, J. Andrews, E. Hauksson, and Y. Yue, 2019, Reliable Real-Time Seismic Signal/Noise Discrimination With Machine Learning, J Geophys Res Solid Earth, 124, no. 1, 788–800, doi: 10.1029/2018JB016661.
Melgar, D. et al., 2023, Sub- and super-shear ruptures during the 2023 Mw 7.8 and Mw 7.6 earthquake doublet in SE Türkiye, Seismica, 2, no. 3, doi: 10.26443/seismica.v2i3.387.
Melgar, D., A. Ganas, T. Taymaz, S. Valkaniotis, B. W. Crowell, V. Kapetanidis, V. Tsironi, S. Yolsal-Çevikbilen, and T. Öcalan, 2020, Rupture kinematics of 2020 January 24 Mw 6.7 Doğanyol-Sivrice, Turkey earthquake on the East Anatolian Fault Zone imaged by space geodesy, Geophys J Int, 223, no. 2, 862–874, doi: 10.1093/gji/ggaa345.
Melgar, D., and G. P. Hayes, 2019, Characterizing large earthquakes before rupture is complete, Sci Adv, 5, no. 5, doi: 10.1126/sciadv.aav2032.
Minson, S. E., A. S. Baltay, E. S. Cochran, T. C. Hanks, M. T. Page, S. K. McBride, K. R. Milner, and M.-A. Meier, 2019, The Limits of Earthquake Early Warning Accuracy and Best Alerting Strategy, Sci Rep, 9, no. 1, 2478, doi: 10.1038/s41598-019-39384-y.
Nakamura, Y., 1988, On the urgent earthquake detection and alarm system (UrEDAS), in *Ninth World Conference on Earthquake Engineering*, 673–678.
Nalbant, S. S., J. McCloskey, S. Steacy, and A. A. Barka, 2002, Stress accumulation and increased seismic risk in eastern Turkey, Earth Planet Sci Lett, 195, nos. 3–4, 291–298, doi: 10.1016/S0012-821X(01)00592-1.
Nazeri, S., S. Colombelli, and A. Zollo, 2019, Fast and accurate determination of earthquake moment, rupture length and stress release for the 2016-2017 Central Italy seismic sequence, Geophys J Int, 217, no. 2, 1425–1432, doi: 10.1093/gji/ggz097.
Nazeri, S., and A. Zollo, 2023, EASOt-AP: An open-source MATLAB package to estimate the seismic moment, rupture radius, and stress-drop of earthquakes from time-dependent P-wave displacements, Comput Geosci, 171, 105293, doi: 10.1016/j.cageo.2022.105293.
Nielsen, S., J. Taddeucci, and S. Vinciguerra, 2010, Experimental observation of stick-slip instability fronts, Geophys J Int, 180, no. 2, 697–702, doi: 10.1111/j.1365-246X.2009.04444.x.
Olson, E. L., and R. M. Allen, 2005, The deterministic nature of earthquake rupture, Nature, 438, no. 7065, 212–215, doi: 10.1038/nature04214.
Patel, S. C., and R. M. Allen, 2022, The MyShake App: User Experience of Early Warning Delivery and Earthquake Shaking, Seismological Research Letters, 93, no. 6, 3324–3336, doi: 10.1785/0220220062.

Peng, C., P. Jiang, Q. Ma, J. Su, Y. Cai, and Y. Zheng, 2022, Chinese Nationwide Earthquake Early Warning System and Its Performance in the 2022 Lushan M6.1 Earthquake, Remote Sens (Basel), 14, no. 17, 4269, doi: 10.3390/rs14174269.

Peng, C., P. Jiang, Q. Ma, P. Wu, J. Su, Y. Zheng, and J. Yang, 2021, Performance Evaluation of an Earthquake Early Warning System in the 2019–2020 M6.0 Changning, Sichuan, China, Seismic Sequence, Front Earth Sci (Lausanne), 9, doi: 10.3389/feart.2021.699941.

Rea, R., S. Colombelli, L. Elia, and A. Zollo, 2024, Retrospective performance analysis of a ground shaking early warning system for the 2023 Turkey–Syria earthquake, Commun Earth Environ, 5, no. 1, 332, doi: 10.1038/s43247-024-01507-3.

Ross, Z. E., and Y. Ben-Zion, 2014, Automatic picking of direct P, S seismic phases and fault zone head waves, Geophys J Int, 199, no. 1, 368–381, doi: 10.1093/gji/ggu267.

Rubin, A. M., and J. P. Ampuero, 2005, Earthquake nucleation on (aging) rate and state faults, J Geophys Res Solid Earth, 110, no. 11, 1–24, doi: 10.1029/2005JB003686.

Rydelek, P., C. Wu, and S. Horiuchi, 2007, Comment on "Earthquake magnitude estimation from peak amplitudes of very early seismic signals on strong motion records" by Aldo Zollo, Maria Lancieri, and Stefan Nielsen.

SATO, T., and T. HIRASAWA, 1973, Body wave spectra from propagating shear cracks., Journal of Physics of the Earth, 21, no. 4, 415–431, doi: 10.4294/jpe1952.21.415.

Satriano, C., L. Elia, C. Martino, M. Lancieri, A. Zollo, and G. Iannaccone, 2011, PRESTo, the earthquake early warning system for Southern Italy: Concepts, capabilities and future perspectives, Soil Dynamics and Earthquake Engineering, 31, no. 2, 137–153, doi: 10.1016/j.soildyn.2010.06.008.

Satriano, C., A. Lomax, and A. Zollo, 2008, Real-time evolutionary earthquake location for seismic early warning, Bulletin of the Seismological Society of America, 98, no. 3, 1482–1494, doi: 10.1785/0120060159.

Satriano, C., Y. M. Wu, A. Zollo, and H. Kanamori, 2011, Earthquake early warning: Concepts, methods and physical grounds, Soil Dynamics and Earthquake Engineering, 31, no. 2, 106–118, doi: 10.1016/j.soildyn.2010.07.007.

Saunders, J. K., B. T. Aagaard, A. S. Baltay, and S. E. Minson, 2020, Optimizing Earthquake Early Warning Alert Distance Strategies Using the July 2019 Mw 6.4 and Mw 7.1 Ridgecrest, California, Earthquakes, Bulletin of the Seismological Society of America, 110, no. 4, 1872–1886, doi: 10.1785/0120200022.

Sheen, D., J. Park, H. Chi, E. Hwang, I. Lim, Y. J. Seong, and J. Pak, 2017, The First Stage of an Earthquake Early Warning System in South Korea, Seismological Research Letters, 88, no. 6, 1491–1498, doi: 10.1785/0220170062.

Tan, O., and T. Taymaz, 2006, Active tectonics of the Caucasus: Earthquake source mechanisms and rupture histories obtained from inversion of teleseismic body waveforms, in *Postcollisional Tectonics and Magmatism in the Mediterranean Region and Asia*, Geological Society of America.

Taymaz, T. et al., 2021, Source Mechanism and Rupture Process of the 24 January 2020 Mw 6.7 Doğanyol–Sivrice Earthquake obtained from Seismological Waveform Analysis and Space Geodetic Observations on the East Anatolian Fault Zone (Turkey), Tectonophysics, 804, 228745, doi: 10.1016/j.tecto.2021.228745.

Trugman, D. T., M. T. Page, S. E. Minson, and E. S. Cochran, 2019, Peak Ground Displacement Saturates Exactly When Expected: Implications for Earthquake Early Warning, J Geophys Res Solid Earth, 124, no. 5, 4642–4653, doi: 10.1029/2018JB017093.

Uenishi, K., and J. R. Rice, 2003, Universal nucleation length for slip-weakening rupture instability under nonuniform fault loading, J Geophys Res Solid Earth, 108, no. B1, doi: 10.1029/2001JB001681.
Vallée, M., and V. Douet, 2016, A new database of source time functions (STFs) extracted from the SCARDEC method, Physics of the Earth and Planetary Interiors, 257, 149–157, doi: 10.1016/j.pepi.2016.05.012.
Vitale, S., and R. Isaia, 2014, Fractures and faults in volcanic rocks (Campi Flegrei, southern Italy): insight into volcano-tectonic processes, International Journal of Earth Sciences, 103, no. 3, 801–819, doi: 10.1007/s00531-013-0979-0.
Worden, C. B., M. C. Gerstenberger, D. A. Rhoades, and D. J. Wald, 2012, Probabilistic relationships between ground-motion parameters and modified mercalli intensity in California, Bulletin of the Seismological Society of America, 102, no. 1, 204–221, doi: 10.1785/0120110156.
Wu, Y.-M., 2003, Relationship between Peak Ground Acceleration, Peak Ground Velocity, and Intensity in Taiwan, Bulletin of the Seismological Society of America, 93, no. 1, 386–396, doi: 10.1785/0120020097.
Wu, Y.-M., and H. Kanamori, 2008, Development of an Earthquake Early Warning System Using Real-Time Strong Motion Signals, Sensors, 8, no. 1, 1–9, doi: 10.3390/s8010001.
Wu, Y. M., and H. Kanamori, 2005a, Experiment on an onsite early warning method for the Taiwan early warning system, Bulletin of the Seismological Society of America, 95, no. 1, 347–353, doi: 10.1785/0120040097.
Wu, Y. M., and H. Kanamori, 2005b, Experiment on an onsite early warning method for the Taiwan early warning system, Bulletin of the Seismological Society of America, 95, no. 1, 347–353, doi: 10.1785/0120040097.
Wu, Y. M., and H. Kanamori, 2005c, Rapid assessment of damage potential of earthquakes in Taiwan from the Beginning of P waves, Bulletin of the Seismological Society of America, 95, no. 3, 1181–1185, doi: 10.1785/0120040193.
Wu, Y., H. Mittal, T. Huang, B. M. Yang, J. Jan, and S. K. Chen, 2019, Performance of a Low-Cost Earthquake Early Warning System (P-Alert) and Shake Map Production during the 2018 Mw 6.4 Hualien, Taiwan, Earthquake, Seismological Research Letters, 90, no. 1, 19–29, doi: 10.1785/0220180170.
Wu, Y. M., and L. Zhao, 2006, Magnitude estimation using the first three seconds P-wave amplitude in earthquake early warning, Geophys Res Lett, 33, no. 16, doi: 10.1029/2006GL026871.
Zhu, W., and G. C. Beroza, 2018, PhaseNet: A Deep-Neural-Network-Based Seismic Arrival Time Picking Method, Geophys J Int, doi: 10.1093/gji/ggy423.
Zollo, A., O. Amoroso, M. Lancieri, Y.-M. Wu, and H. Kanamori, 2010, A threshold-based earthquake early warning using dense accelerometer networks, Geophys J Int, 183, no. 2, 963–974, doi: 10.1111/j.1365-246X.2010.04765.x.
Zollo, A., S. Colombelli, A. Caruso, and L. Elia, 2023, An Evolutionary Shaking-Forecast-Based Earthquake Early Warning Method, Earth and Space Science, 10, no. 4, doi: 10.1029/2022EA002657.
Zollo, A., M. Lancieri, and S. Nielsen, 2006, Earthquake magnitude estimation from peak amplitudes of very early seismic signals on strong motion records, Geophys Res Lett, 33, no. 23, doi: 10.1029/2006GL027795.
Zollo, A., N. Maercklin, M. Vassallo, D. Dello Iacono, J. Virieux, and P. Gasparini, 2008, Seismic reflections reveal a massive melt layer feeding Campi Flegrei caldera, Geophys Res Lett, 35, no. 12, doi: 10.1029/2008GL034242.

Zollo, A., S. Nazeri, and S. Colombelli, 2022, Earthquake Seismic Moment, Rupture Radius, and Stress Drop from P-Wave Displacement Amplitude Versus Time Curves, IEEE Transactions on Geoscience and Remote Sensing, 60, doi: 10.1109/TGRS.2021.3119909.